5-2018

Mass Transport of Metallic Nanostructures during Sintering Process: A Molecular Dynamics Perspective

Jiaqi Wang
University of Tennessee

To the Graduate Council:

I am submitting herewith a thesis written by Jiaqi Wang entitled "Mass Transport of Metallic Nanostructures during Sintering Process: A Molecular Dynamics Perspective." I have examined the final electronic copy of this thesis for form and content and recommend that it be accepted in partial fulfillment of the requirements for the degree of Master of Science, with a major in Mechanical Engineering.

Seungha Shin, Major Professor

We have read this thesis and recommend its acceptance:

Anming Hu, David J. Keffer

Accepted for the Council:
Dixie L. Thompson

Vice Provost and Dean of the Graduate School

(Original signatures are on file with official student records.)

Mass Transport of Metallic Nanostructures during Sintering Process: A Molecular Dynamics Perspective

A Thesis Presented for the

Master of Science

Degree

The University of Tennessee, Knoxville

Jiaqi Wang

May 2018

I would like to dedicate this thesis to my parents, who are always loving and supporting me in my life.

Acknowledgments

I would like to sincerely thank my supervisor Prof. Seungha Shin, for his patience and intelligence devoted to me. Also I have to gratefully thank my parents, who raised me up with great efforts and costs. Last but not the least, I thank all of my dear friends, who provide me support, fun and happiness.

Abstract

Sintering of nanomaterials has been broadly utilized as a joining technique in various applications for achieving excellent mechanical, thermal, and electronic properties. However, the joining of the nanomaterial will facilitate the growth of the nanograin, which deteriorate the performance of the mechanical properties. Also, different defects developed during the sintering process deteriorate the thermal and electronic properties. Therefore, how to prevent the growth of the nanograin and the development of the defects during sintering have become an extremely important issue for improving the properties of sintered joints. This research employs molecular dynamics approach to reveal the atomic-scale sintering dynamics and study the properties of the sintered products of Cu-Ag core-shell nanoparticles (NPs) and nanowires (NWs), over a wide range of temperatures and on three different sintering models: (1) two core-shell NP model; (2) two core-shell NW model; (3) multiple core-shell NP model. Two new sintering mechanisms are found: (1) crystallization-amorphization-recrystallization during solid-phase sintering process and (2) wetting in the sintering of two unequally sized NPs induced by its own small size of existence of Cu core. A three-stage sintering is found for both NPs and NWs. The rupture strength of the sintered joint in the NW is found even higher than the CS NW itself. The effect of porosity and NP agglomeration effect on sintering of multiple core-shell NP model is unravled and the properties of the sintered structure at different temperatures are analyzed in terms of the porosity, grain size, and crystallinity. Through these researches, size and temperature effects on the sintering dynamics of the Cu-Ag core shell NPs/NWs are unraveled, enhanced understanding in defects formation and grain growth are achieved. Those results are expected to contribute to the development of various applications such as electronic packaging, wearable electronics, and energy devices.

Table of Contents

List of Tables

List of Figures

Chapter 1

Introduction

1.1 Sintering of Copper (Cu)-Silver (Ag) Core-Shell Nanostructures

Sintering, as a manufacture technique in powder metallurgy and ceramic processing at microscopic/macroscopic [4], has been extended to nanoscale, as a pathway to achieve flexible and low-cost electronic devices [5, 6, 7, 8]. Among various nanostructures, Ag nanoparticles/nanowires have been broadly utilized due to their excellent thermal and electrical conductivity. However, the high cost in synthesizing the Ag nanostructure and the material itself has prohibited wider application of them. In order to lower the cost while maintaining the high thermal and electrical conductivities, the Cu-Ag core-shell structure has been adopted as an alternative. This Cu-Ag core-shell structure can also effectively prevent the oxidation of the Cu core.

In all of those electronic applications, the Ag nanostructures are required to sinter to each other, in order to achieve a more densified structure with higher mechanical strength, thermal, and electrical conductivities. However, during sintering process, growth of grain and formation of defect normally occurs, which would deteriorate the properties of the final sintered structures. Thus, understanding the sintering dynamics under different conditions is a prerequisite for efficient control of sintering products. Sintering of microscopic/macroscopic nanoparticles have been extensively studied, and six dominant mechanisms are unravelled

[1], they are: (1) surface diffusion; (2) lattice diffusion from the surface; (3) vapor transport; (4) grain boundary diffusion; (5) lattice diffusion from the grain boundary; (6) plastic flow, as shown in the Figure 1.1. However, the nanostructures have very large surface area to bulk volume ratio, i.e., the surface atoms occupy a large fraction of the whole atoms. Thus, the surface energy of the nanostructures is much higher than the bulk counterpart, which can induce different sintering mechanisms due to higher surface mobility. In summary, the surface crystallographic orientation, size, temperature, etc. would yield different sintering dynamics of the nanostructures, while the research of sintering of nanostructures is still immature.

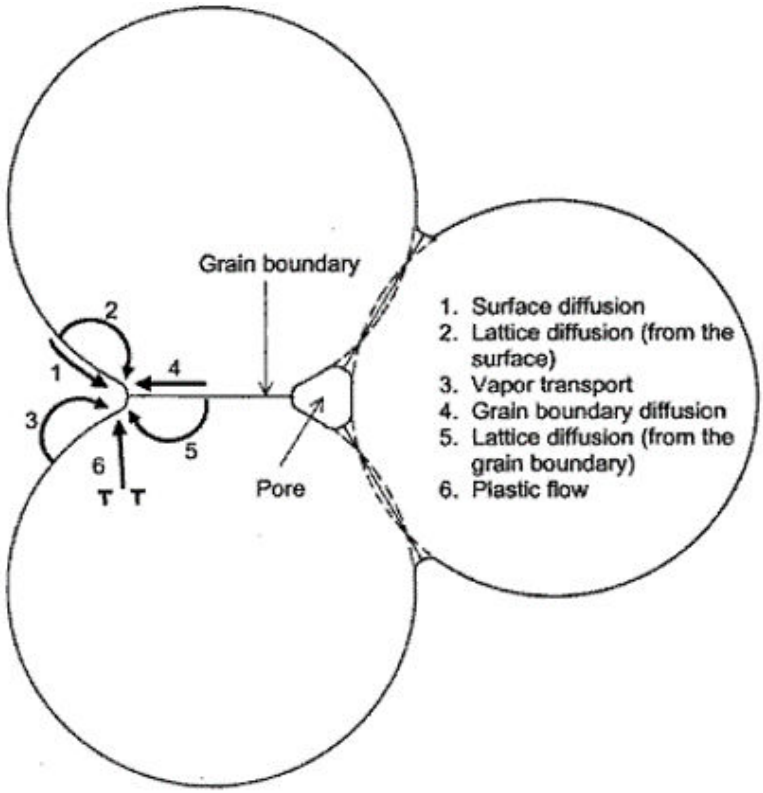

Figure 1.1: Six dominant sintering mechanisms of microscopic/macroscopic particles. This image is a modified version from the book [1].

There are two main problems in the current research of sintering of nanostructures: (1) Most researches focus on monometallic two-nanoparticle (NP) model, which is only validated for loosely-packed NP sintering on substrate or in gas phase, thus it neglects important factors, such as the porosity and NP agglomeration effect, which can alternate the sintering

dynamics. Very limited researches can be found on the sintering of multiple NPs, thus the sintering dynamics of a more realistic model is still quite immature; (2) None of the research has studied the sintering dynamics of core-shell nanostructures, instead only the pure NP has been studied. Because of the existence of the core, the surface mobility of the nanostructues can be significantly increased, which can also alternate the sintering dynamics and influence the properties of the sintered product.

As an initial work in sintering dynamics of core-shell nanostructure, this work is divided into three stages, aiming at obtaining an integrative understanding of the sintering mechanism at different sintering conditions, including the growth of the grain and formation of defects. In the first stage of this research, sintering of two-NP model with Cu-Ag NPs are studied. Temperature and size effect of the sintering dynamics are included. Novel sintering mechanisms are unravelled. In the second stage, sintering of two-NP/NW model with Cu-Ag core-shell NPs and NWs at room temperature is compared. A three-stage sintering is found for both NPs and NWs. It is also found that the rupture strength of the sintered joint in the NW can be higher than the CS NW itself. In the third stage, the sintering dynamics of multiple-NP model with Cu-Ag core shell NP, and the properties of the sintered structure at different temperatures are analyzed in terms of the porosity, grain size, and crystallinity.

Due to the ultrafine size of the nanostructure, it is challenging to design *in situ* experiment to harvest the atomic-scale sintering mechanisms, thus molecular dynamics is employed, which can provide us an atomic-scale perspective. A brief introduction to molecular dynamics is presented in the following section and all of the details of simulation setup and results will be elaborated in the following three chapters (chapter 2, 3, and 4).

1.2 Molecular Dynamics

Molecular dynamics (MD) simulation is one of the types of "computer simulations", which investigates various atomic-scale phenomena, such as mass transport (e.g., melting, sintering, oxidation, diffusion, etc) and thermal transport (e.g., phonon scattering) (Figure 1.2). MD is also capable of calculating various static properties, including lattice constant, bulk modulus, heat capacity, thermal expansion coefficient, etc.

MD employs the Newton's second law to derive the motion of atoms at each time step, as indicated by this equation:

$$f_i = -\frac{\partial u}{\partial r_i} \tag{1.1}$$

Here f_i is the force acting on atom i, and u is the potential energy, which is specified by the interaction parameters in input file or a separate interaction potential file as used for embedded atom method potential.

Equation 1.1 illustrates the most fundamental but simple physics underlying MD. From this equation, it is known that the accuracy of the interaction potential determines the value of the simulation results (namely, MD obeys the simple rule: garbage in, garbage out). Thus, selecting a suitable potential is always the first step, and the most important step before implementing any simulation. Also, there are many other details need extreme care, such as boundary condition, timestep, system size, ensemble, simulation time, scaling performance, etc. Since all of these are not main focus of this research and they have already been documented in detail in many books and papers [9, 10, 11, 12, 13, 14, 15], they will not be elaborated here.

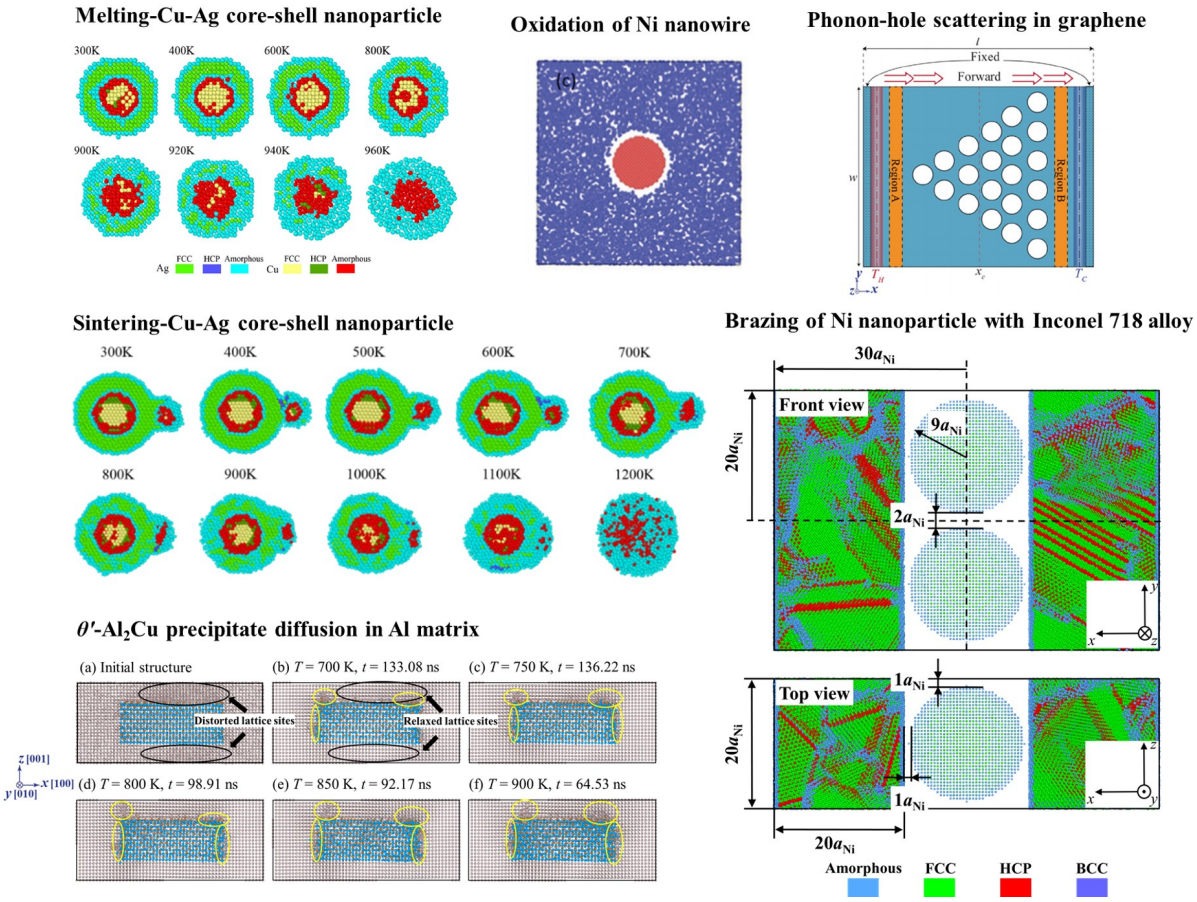

Figure 1.2: Application examples of molecular dynamics, including melting, oxidation, phonon scattering, sintering, brazing, and precipitate diffusion. The images of "Oxidation of Ni nanowire" and "Phonon-hole scattering in graphene" are from the paper "Role of surface oxidation on the size dependent mechanical properties of nickel nanowires: a ReaxFF molecular dynamics study" [2] and "Thermal rectification via asymmetric structural defects in graphene" [3], respectively. All others images are from Jiaqi Wang's own work.

Chapter 2

Geometrical Effects on Sintering Dynamics of Cu-Ag Core-Shell Nanoparticles

Note: Chapter 2 is a modified version of the publication: **Jiaqi Wang**, Seungha Shin*, and Anming Hu, "Geometrical effects on sintering dynamics of Cu-Ag core-shell nanoparticles", The Journal of Physical Chemistry C, 120, 17791-17800 (2016).

2.1 Introduction

Bimetallic nanoparticle (NP) [16, 17, 18, 19, 20] has unique thermal, electrical, and mechanical properties, which have contributed to the development of technology in wire-bonding, lead-free soldering materials and construction of nanoscale devices. Ag NPs with various sizes have been created and utilized as conductive pastes in these applications in order to achieve reliable joining with other structures through sintering [16, 21]. However, the high cost of Ag NPs has hindered the industrial application of such technology [22, 23]. Pure Cu has thermal and electrical conductivities comparable to pure Ag (only 4.5% and 6.5% less than that of Ag respectively) [24], whereas the price of pure Cu nanopowder is only one-quarter of Ag nanopowder. For lowering cost while maintaining the good thermal

and electrical conductivities, Cu-Ag core-shell (CS) NP is synthesized as a replacement of pure Ag NP [25, 26, 27, 28].

The sintering of NPs is a crucial metallurgic method for fabrication of nanomaterials with tailored properties, and is frequently utilized in nanojoining and inkjet printing technology [29, 30, 31, 32, 33, 34, 35]. NP has larger surface curvature and higher surface energy compared with bulk counterpart, both of which facilitate the sintering of NPs and render the sintering process different from their micro/millimeter-scale counterparts [36]. Numerous studies have been conducted to identify the effects of NP size, temperature, heating rate, and crystallographic orientation on the sintering process of NPs [37, 38, 39, 40]. Various sintering mechanisms including stress-induced plasticity [38], elastic deformation and surface diffusion mechanisms [39] have been suggested; among them, it has been broadly reported that the sintering of NPs is dominated by surface diffusion and grain boundary diffusion [41]. However, the sintering of Cu-Ag CS NPs has not been studied according to our best knowledge, and different dominant sintering mechanisms are expected due to the interfacial restructuring because of the lattice mismatch between Ag and Cu [42].

In this research, molecular dynamics (MD) is firstly employed to simulate the sintering of Cu-Ag CS NPs. Despite a limited experimental observation of the structural evolution during sintering, the MD simulation provides a powerful tool to monitor the atom trajectory [36, 43, 44]. Temperature and size effects on the sintering kinetics are investigated by evolution of shrinkage (ζ), local crystalline structure, and potential energy (PE, E_P) during sintering.

2.2 Methodology

2.2.1 MD Simulation Implementation

The embedded atom method (EAM) potential [45] for Cu and Ag alloy system is selected as the force field in our simulations. This binary EAM potential is constructed from a combination of existing EAM potentials for Cu and Ag, both of which can accurately reproduce the lattice parameters, cohesive energy, elastic constants, and phonon frequencies

of Cu and Ag [46], respectively. In addition, the Cu-Ag phase diagram and high-temperature properties calculated from the constructed EAM agree well with experiments, which demonstrates that the selected force field is suitable for the melting and sintering simulations over broad temperature ranges [46]. Based on this potential model, the total energy of the bimetallic system is:

$$E_{tot} = \frac{1}{2}\sum_{ij} v_{ij}(r_{ij}) + \sum_{i} F_i(\bar{\rho}_i) \tag{2.1}$$

where $v_{ij}(r_{ij})$ is the pair interaction energy between atoms i and j separated by distance r_{ij}, and F_{ij} is the embedding energy of atom i, which is a function of the host electron density $\bar{\rho}_i$. The $\bar{\rho}_i$ is given by

$$\bar{\rho}_i = \sum_{j \neq i} \rho_j(r_{ij}) \tag{2.2}$$

where $\rho_j(r_{ij})$ is the electron density function of atom i assigned to atom j.

The Cu core and Ag shell atoms both within face-centered cubic (FCC) lattice sites are located in a spherical shape in non-periodic vacuum cell. Each CS NP is relaxed at 300 K for 50 ps separately to eliminate any effects induced by instabilities of initial CS structure. After relaxation, the PE of the CS NP reaches equilibrium, indicating that the whole system is fully relaxed. The equilibrated NPs are then used as initial structures for melting and sintering simulations, and all the simulations in this research are performed using the LAMMPS code [47], and part of the simulations relies on Extreme Science and Engineering Discovery Environment (XSEDE) resources [48].

NVT canonical ensemble (constant number of atoms, volume, and temperature) is employed with the Nosé-Hoover thermostat for temperature control. A uniform temperature is obtained by eliminating the temperature gradient inside the NP with isothermal-heating (IH) method [43]; thus, heat transfer effects on the melting and sintering process can be ignored. 1 fs is chosen as a time step, which has been validated that it conserves energy well in NVE microcanonical ensemble (constant number of atoms, volume, and energy). The duration of sintering simulation is 500 ps. Several test simulations up to 10 ns showed that the sintered morphology did not show distinct change after 500 ps; thus, 500 ps is selected

as a total simulation time. Although a complete sintering process cannot be achieved within this time scale (not even in 10 ns), various phenomena in the early stages of the sintering process including neck formation, neck growth, and densification can be studied through these MD simulations.

2.2.2 Analysis Method

PE and Lindemann index (LI, δ_{LI}) have been widely applied to determine the melting points (MPs) of CS and pure NPs in previous studies [49, 50, 51, 52]. MP is identified as a temperature at which a steep increase of PE occurs due to the absorption of latent heat as NP melts. LI indicates thermally driven disorders and determines the MP at which a sharp increase occurs. LI values of 0.07 and 0.1 are regarded as melting criteria of pure Ag and Cu atoms [49], and an atom with LI larger than the criteria is defined as a Lindemann atom. The LI of a single atom i is given by [53]:

$$\delta_{\mathrm{LI},i} = \frac{1}{N-1} \sum_{j \neq i} \frac{\sqrt{\langle r_{ij}^2 \rangle - \langle r_{ij} \rangle^2}}{\langle r_{ij} \rangle} \tag{2.3}$$

where N is the total number of atoms in the system, r_{ij} is the distance between i-th and j-th atoms, and $\langle\rangle$ represents an ensemble average. The LI of the system is defined as the average of the LI over all N atoms given by

$$\delta_{\mathrm{LI}} = \frac{1}{N} \sum_{i} \delta_{\mathrm{LI},i} \tag{2.4}$$

Shrinkage (ζ) characterizes the sintering process and is defined as the ratio of change in distance of centers of mass to initial distance, given by [43]

$$\zeta = \frac{\Delta L}{L_0} = \frac{L_0 - L}{L_0} \tag{2.5}$$

where L_0 is the distance between the centers of mass of two adjacent NPs at the onset of sintering (equivalent to the addition of two sintered NPs' radii), and L is the instantaneous distance of centers of mass during sintering process. In the analysis of sintering mechanisms

and processes, the slope of shrinkage curve is employed to distinguish sintering stages. Neck size, as an important parameter in determining the sinterability of two NPs [16, 54], is also measured where the curvature is the largest among the circumference.

The mean squared displacement (MSD, $\langle d^2 \rangle$) of Ag shell atoms located within the outermost layer is calculated to reveal the sintering mechanism by Einstein's relation, which is given by

$$\langle d^2 \rangle = \langle \{ [r(t_0 + \tau) - r_{com}(t_0 + \tau)] - [r(t_0) - r_{com}(t_0)] \}^2 \rangle \tag{2.6}$$

Here t_0 is the time origin, and τ is the observation time. $\langle\rangle$ represents an ensemble average over all atoms and all time origins. $r(t_0)$ is atom position at time origin, while $r_{com}(t_0)$ is position of center of mass at time origin. After observation time τ, the position of each atom and center of mass become $r(t_0 + \tau)$ and $r_{com}(t_0 + \tau)$, respectively. The calculated MSD has eliminated any effect of the random center-of-mass motion caused by Nosé-Hoover thermostats.

The local structural evolution is identified through the common neighbor analysis [55, 56, 57], which has been extensively employed for the study on structural evolution of nanomaterials during melting, sintering, and mechanical deformation processes [58, 59, 60, 61, 62, 63]. Usually, two atoms are regarded as bonded, if their distance is less than a specified cutoff radius r_{cut}; e.g., for FCC structures, the cutoff radius is set to be halfway between the first and second neighbors,

$$r_{\text{cut}}^{\text{FCC}} = \frac{a_{\text{FCC}}(1/\sqrt{2} + 1)}{2} \approx 0.854 a_{\text{FCC}} \tag{2.7}$$

where a_{FCC} is the lattice constant of FCC crystal structure. The obtained cutoff radii for Ag and Cu, according to Equation 2.7, are 3.491 and 3.081 Å, respectively. Local orders of atoms are classified into three categories: (1) FCC (atoms in a local FCC order), (2) hexagonal closed packed (HCP, atoms in a local HCP orders), and (3) amorphous (atoms in all other local orders). A single HCP layer in the FCC crystal is regarded as a twin boundary (TB), while two HCP layers are considered to be a stacking fault [60, 63].

2.3 Results and Discussion

2.3.1 Thermal Stability: Melting of Different-Sized Cu-Ag CS NPs

Thermal stabilities of four different-sized Cu-Ag CS NPs with a fixed core radius/shell thickness ratio (1:1) are studied (Table 2.1 and Figure 2.1). These simulations identify MPs and melting process, which validates our simulation methodology. Additionally, since the melting of the NP is known to significantly affect the sintering process (e.g., the surface premelting of the NP facilitates the shrinkage growth during sintering process [16]), the thermal stability of the NP under various conditions should be identified to understand the sintering mechanisms.

Table 2.1: Configuration of Cu-Ag core-shell NPs with four different sizes. NP type is presented as Ag_xCu_y, and x or y is time of lattice constant (a_{Ag} = 4.085 Å) of Ag. Note that x:y is not ratio of number of Ag atoms to number of Cu atoms, but the ratio of CS NP radius to core radius, and it is maintained as 2:1. Namely, the ratio of shell thickness to core radius is 1:1.

NP type	Shell thickness/Å	Core radius/Å	#Cu atoms	#Ag atoms
(a) $Ag_3Cu_{1.5}$	$1.5a_{Ag}$	$1.5a_{Ag}$	79	401
(b) $Ag_5Cu_{2.5}$	$2.5a_{Ag}$	$2.5a_{Ag}$	369	1871
(c) $Ag_7Cu_{3.5}$	$3.5a_{Ag}$	$3.5a_{Ag}$	1055	5089
(d) $Ag_9Cu_{4.5}$	$4.5a_{Ag}$	$4.5a_{Ag}$	2171	10707

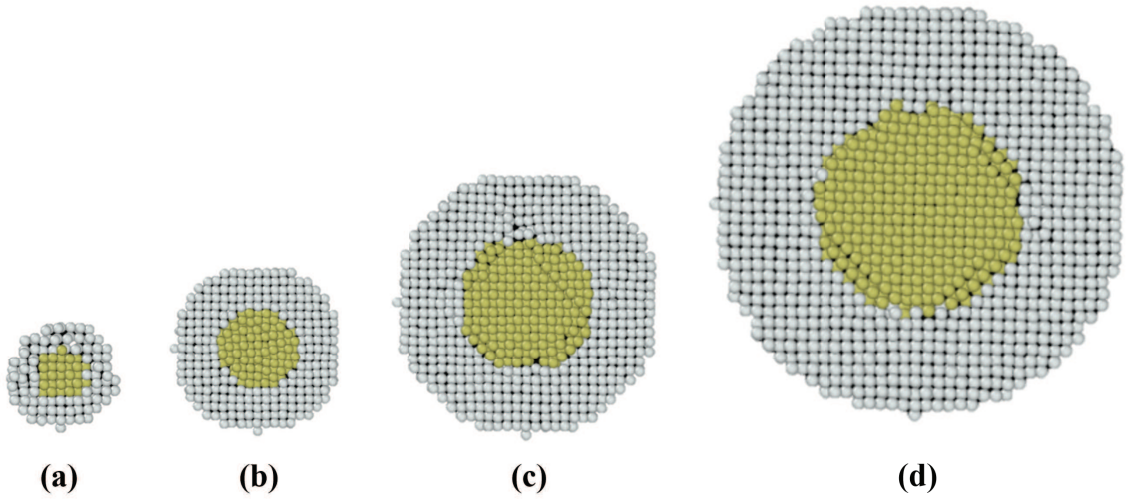

Figure 2.1: Cross-sectional images of four Cu(gold)-Ag(grey) core-shell NPs with different sizes: (a) $Ag_3Cu_{1.5}$, (b) $Ag_5Cu_{2.5}$, (c) $Ag_7Cu_{3.5}$, (d) $Ag_9Cu_{4.5}$.

MPs are determined as 720, 960, 1140, and 1220 K for $Ag_3Cu_{1.5}$, $Ag_5Cu_{2.5}$, $Ag_7Cu_{3.5}$, and $Ag_9Cu_{4.5}$, respectively, as indicated by PE and LI profile in Figures 2.2a and 2.2b. Local crystalline structural evolution (Figure 2.3) and LI of each atom (Figure 2.4) in $Ag_5Cu_{2.5}$ during IH process are shown as a representative melting process. The MPs, determined by well-established PE and LI criteria, coincide well with each other for various sizes of NP, which verifies our methodology.

Before melting, both PE and LI increase linearly with temperature. Surface atoms of Ag shell and interfacial atoms show higher mobility than other atoms. When the temperature of NP $Ag_5Cu_{2.5}$ reaches 900 K, surface premelting occurs as indicated by appearance of Lindemann atoms in the outer shell [Figure 2.4(c)], and this surface premelting propagates from outer shell to inner core as temperature increases [Figures 2.4(d), and (e)]. The observation of surface premelting and its propagation direction agree well with previous reports for the Cu-Ag CS NP [64], and also other NPs such as Pt-Pd CS NPs [65]. At 960 K, all of the inner core atoms are excited, and no crystal structure is maintained at this temperature [Figures 2.3 at 960 K and 2.4(f)] . The LI evolution of inner core atoms also coincides with reported simulation results [58].

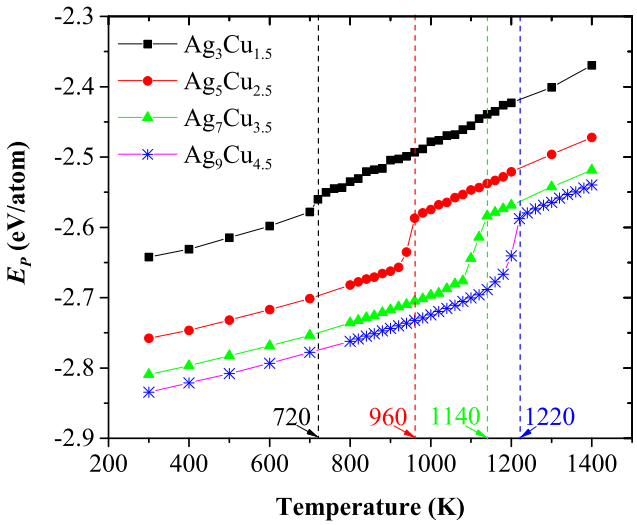

(a) Potential energy (E_p)

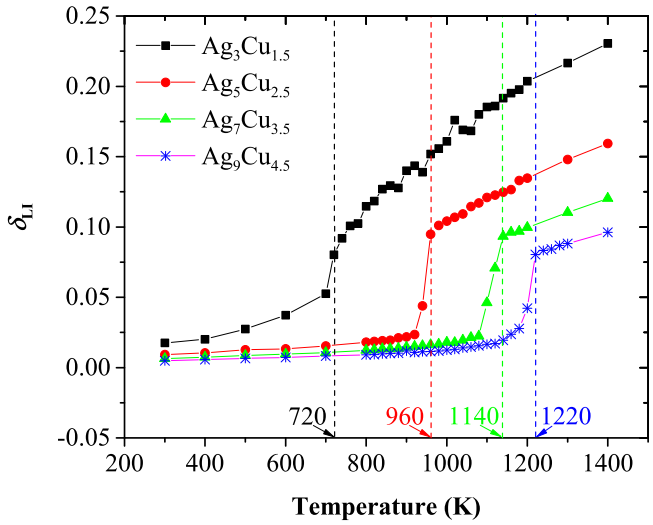

(b) Lindemann index (δ_{LI})

Figure 2.2: Temperature dependence of ensemble-averaged (a) potential energy (E_P), and (b) Lindemann index (δ_{LI}) profile of different-sized NPs during IH process.

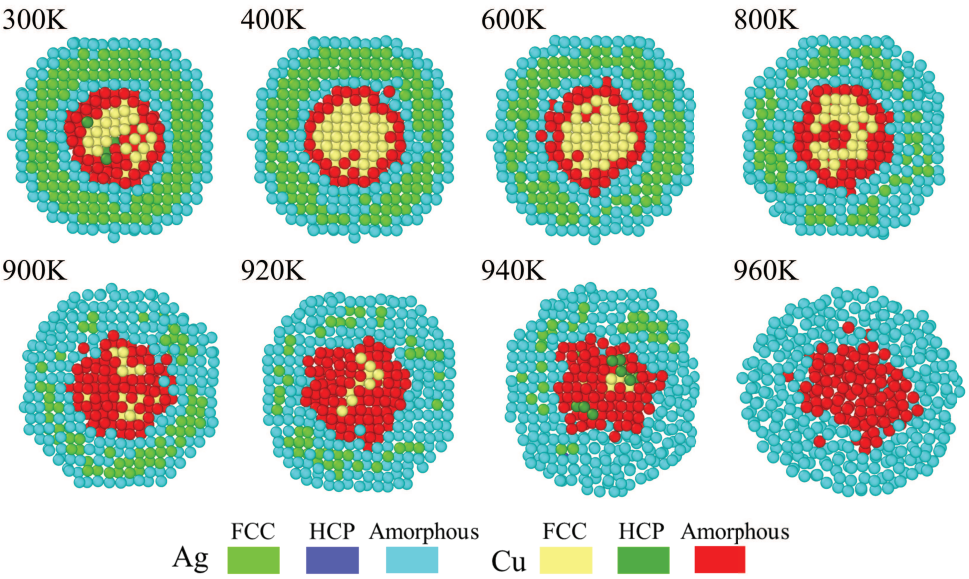

Figure 2.3: Local crystalline structure evolution of NP $Ag_5Cu_{2.5}$ at representative temperatures. It is analyzed by common neighbor analysis. (Light Green: Ag FCC; Blue: Ag HCP; Cyan: Ag amorphous; Yellow: Cu FCC; Dark Green: Cu HCP; Red: Cu Amorphous) As temperature increases, atoms located in FCC lattice site of both Ag shell and Cu core switch to amorphous orders. At 960 K, no FCC or HCP lattice is observed, indicating the completion of solid to liquid phase transition. This coincides well with the melting temperature determined by potential energy and Lindemann index profile.

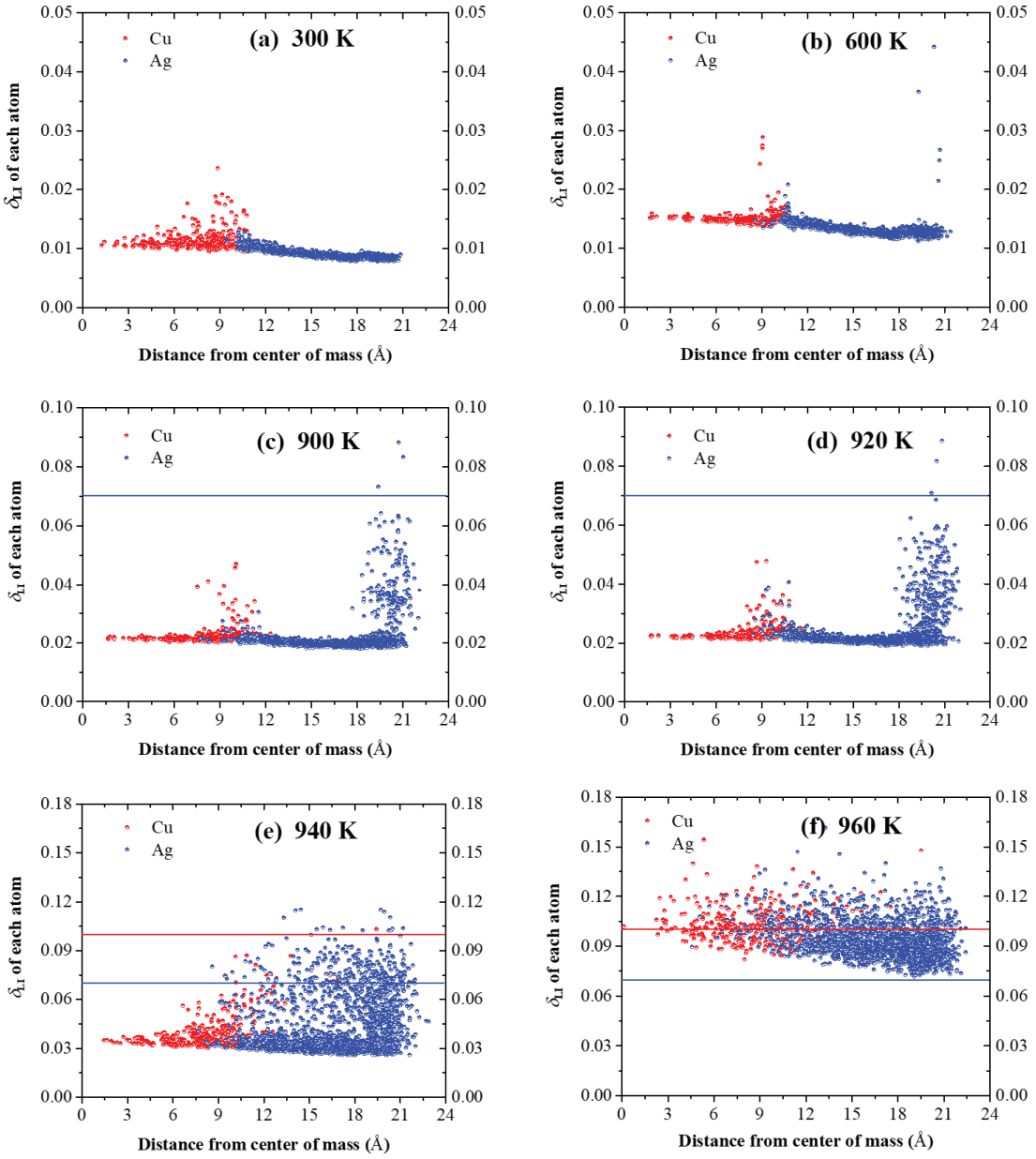

Figure 2.4: Lindemann index (LI, δ_{LI}) of each atom along the radius of NP $Ag_5Cu_{2.5}$ at representative temperatures. Red sphere represents LI of Cu core while blue one represents the LI of Ag shell. Disorders of both shell and interface regions increase with increasing temperature. The disorders of the shell atoms lead to the surface premelting, and propagate toward the center of the NP.

2.3.2 Sintering of Two Equally Sized NPs

To investigate the size effects on the sintering dynamics of two equally sized NPs, three pairs of NPs, which are $Ag_3Cu_{1.5}$-$Ag_3Cu_{1.5}$, $Ag_5Cu_{2.5}$-$Ag_5Cu_{2.5}$, $Ag_7Cu_{3.5}$-$Ag_7Cu_{3.5}$, are studied at various temperatures (300 K to 1200 K). The initial structure is relaxed at 300 K for sintering simulations at all different temperatures, and the geometrical details of the two NPs are the same as the ones in the melting simulations. The local crystalline structure in cross section of NP pair $Ag_5Cu_{2.5}$-$Ag_5Cu_{2.5}$ after relaxation at 300 K is shown in Figure 2.5a. Because of the small size (i.e., large curvature, which induces high surface energy), the geometry of NP after relaxation is faceted, deviating from a perfect spherical shape. Since the facets have different areas and crystallographic orientations, they release different amounts of energy when the free surface is annihilated during sintering. Therefore, different sintering mechanisms are expected due to different amounts of released energy. In order to eliminate the effect of relative crystallographic orientation, the left and right NPs are placed facing (100) surfaces to each other, with a distance of 3 Å between the nearest atoms in all cases. After relaxation, the local orders of Ag atoms located in proximity of the surface and the Ag/Cu interface are amorphous, while the atoms located between the surface and interface remain at FCC lattice sites and no HCP crystalline structure is detected in Ag shell. The interfacial Cu atoms are also recognized as amorphous due to restructuring by the lattice mismatch and interfacial interaction, and the Shockley partial dislocations form HCP atoms in two adjacent (111) planes within the core [60, 66].

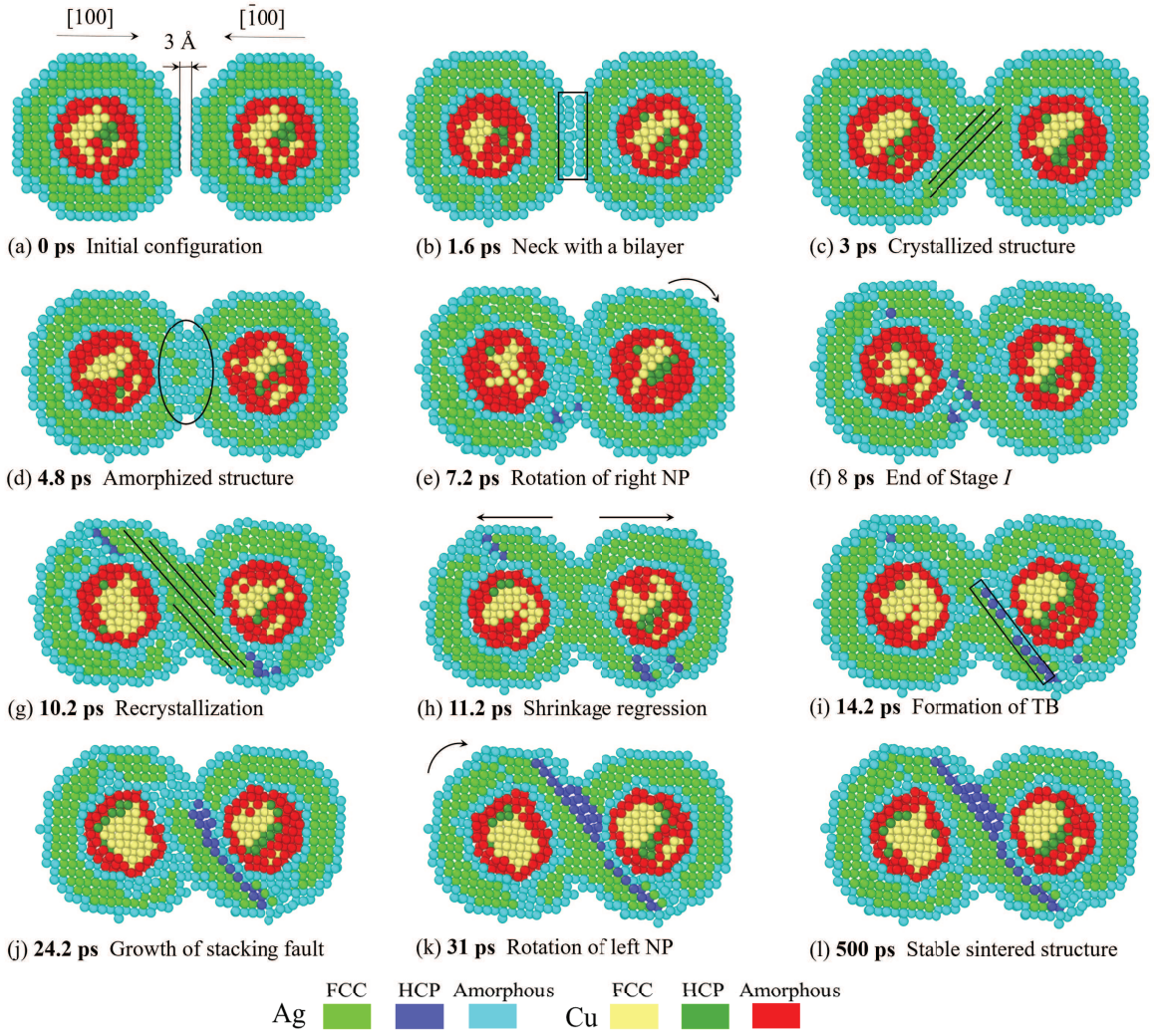

Figure 2.5: Local crystalline structure of two $Ag_5Cu_{2.5}$ NPs during solid-phase sintering at 300 K. (a) Initial atomic configuration after relaxation at 300 K and (b)-(l) structural evolution at various instants. Color scheme is explained as below: Cyan: Ag amorphous; Light Green: Ag FCC; Blue: Ag HCP; Red: Cu Amorphous; Yellow: Cu FCC; Dark Green: Cu HCP.

Kinetic energy (KE), which is dependent on temperature, should be sufficient to activate the diffusion mechanism for sintering, and the diffusion activation energy depends on the location (e.g., surface, interface, core, etc.) and structure (e.g., FCC, HCP, and amorphous). Thus, different sintering mechanisms are expected depending on temperature. Here, the sintering mechanisms of NPs are discussed in three temperature regimes; solid-phase (< MP - 100 K), surface-premelting-induced (MP - 100 K < T < MP), and liquid-phase sintering (> MP). Since the solid-phase sintering is critical in the assembly and joining of nanomaterials, sintering mechanism at room temperature is our main focus.

The snapshots of local crystalline structural evolution of two $Ag_5Cu_{2.5}$ NPs during sintering at 300 K are chosen as a representative to illustrate the solid-phase sintering process [Figure 2.5 (b)-(l)]. At initial stage of sintering, the NPs approach each other, forming a neck with weak bonding. This initial bilayer neck is amorphous, inducing a high-energy grain boundary [Figure 2.5(b)]. Interfacial atoms are then relaxed for energy minimization, forming crystalline structures [Figure 2.5(c)]. Therefore, the grain boundary energy decreases, as demonstrated by the reduction in PE of Ag shell between points (b) and (c) in Figure 2.6a. However, this initially crystallized structure is transient; i.e., as neck grows, the crystallized neck region becomes amorphous again, and only a small fraction of crystallized structure remains [Figur 2.5(d)]. Reduction in surface area and curvature as a result of sintering from point (c) to (d) further decreases PE by annihilation of free surfaces. Starting from point (d), PE climbs to a peak at point (e) due to the elastic energy induced by formation of HCP structure [Figure 2.5(e)]. Right after point (e), NPs are rotated for optimal crystallization positions. Consequently, atoms in the neck region are crystallized again with strong bonding [Figure 2.5(g)], contributing to PE reduction from point (e) to (g). Amorphization-recrystallization has been reported for sintering of nickel NPs with 2.2 nm diameter [67, 68], however, here we observe crystallization before amorphization, and thus a new crystallization-amorphization-recrystallization mechanism is detected. This difference can be attributed to two reasons. First, crystallization before amorphization occurs very quickly in the initial stage of sintering, which is accomplished within several picoseconds, making it difficult to observe especially in experiment. Therefore, it has not been reported before from both computational and experimental perspectives. Second, this mechanism is

size dependent. For nickel NP with a diameter of 2.2 nm, surface atoms with dangling bonds occupy a large fraction of the whole NP. As a result, the NP itself is in a quasi-liquid state, making it difficult to crystallize before amorphization during sintering. After sintering, two NPs coalesce into one larger NP and then it crystallizes to reach an energy-minimum state.

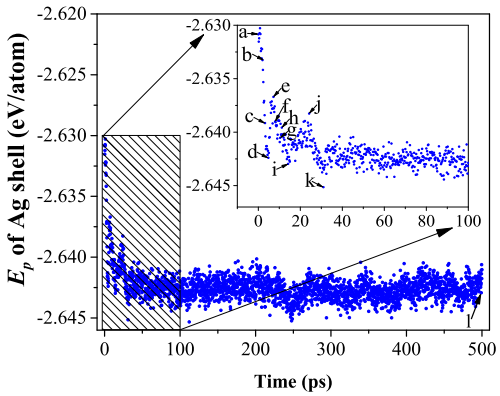

(a) Potential energy (E_p)

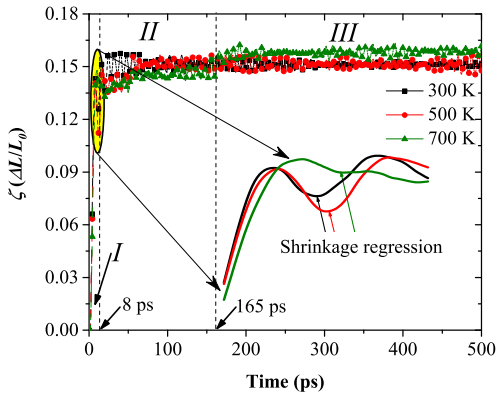

(b) Shrinkage (ζ)

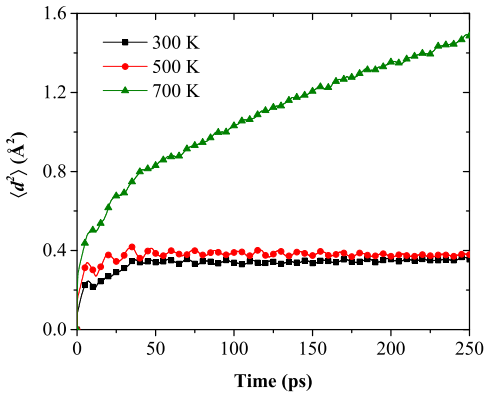

(c) Mean square displacement (MSD, $\langle d^2 \rangle$)

Figure 2.6: (a) Potential energy (E_p) evolution of Ag shell during the sintering of NP pair $Ag_5Cu_{2.5}$-$Ag_5Cu_{2.5}$ at 300 K. Points a to l indicate the instants illustrated in Figure 2.5, at which representative structural transformations occur. (b) Shrinkage (ζ) of two equal-sized $Ag_5Cu_{2.5}$ NPs during solid-phase sintering at 300 K (black square), 500 K (red circle), and 700 K (green triangle). The sintering process is divided into three stages: (I) neck formation (1.6 ps) and fast growth (1.6-8 ps), (II) slow neck growth (8-165 ps), and (III) equilibrium stage (165-500 ps). The shrinkages of the second and third stages depend on the sintering temperature. (c) Mean square displacement (MSD, $\langle d^2 \rangle$) evolution of the outermost layer atoms in NP $Ag_5Cu_{2.5}$ at 300 K (black square), 500 K (red circle), and 700 K (green triangle). MSD reaches equilibrium at low temperatures (< 500 K), while it increases linearly with observation time at higher temperatures (> 500 K).

After recrystallization, shrinkage regression [Figures 2.5(h) and 2.6b] is commonly observed for these three parallel pairs with equally-sized NPs, presumably due to the occurrence of elastic collision, which is more pronounced at the initial stage of sintering [(before 165 ps in Figure 2.6b] [43, 69, 70]. During the bouncing-back process, the PE is converted to KE, however, shrinkage regression increases the surface area, contributing to the PE increase from point (g) to (h). At point (i), a twin boundary appears along the [111] direction, and gradually develops intrinsic stacking fault [Figure 2.5(j)], which consists of two adjacent planes of HCP atoms and confirms that the Shockley partial dislocation occurs in (111) planes during the sintering. The partial dislocation core then passes through the left NP, causing the rotation of left NP [Figure 2.5(k)]. A stacking fault is left behind and finally ends on the free surface of left NP, forming stable stacking faults in the sintered structure [Figure 2.5(l)]. The formation of stacking fault also increases the PE of the sintering system [from point (i) to (j)], which is quickly damped out by thermostats and further rotation of right NP [from point (j) to (k)]. Twin boundary formation and stacking fault growth confirm that the plastic deformation via dislocation propagation is an important mechanism for the early-stage solid-phase sintering [39, 67, 71]. Understanding the formation mechanism of twin boundaries and stacking faults in FCC lattice could possibly improve the thermal and electrical conductivities of the sintered structure by manipulation of size, temperature and crystallographic orientation [72].

The sintering process can be characterized by three stages as the shrinkage curves [Figure 2.6b] illustrate. This three-stage process is also observed in solid-phase sintering of different sizes of NP pairs [Figure 2.7 (a) and (b)]. Stage I includes the neck formation and rapid growth, marked by a sharp increase of shrinkage, which is accomplished at around 8 ps at all temperatures. Since the initial coalescence of NPs does not require thermal activation [18], the neck formation and rapid growth stages are independent of temperature, as evidenced by the similar shrinkage slope, $d\zeta/dt$. Such an observation is similar to the sintering of NPs $Ag_3Cu_{1.5}$ and $Ag_7Cu_{3.5}$; however, the duration of stage I depends on the NP size. Smaller NPs have higher surface energy and curvature, leading to a faster neck formation and growth stage (e.g., for $Ag_3Cu_{1.5}$ and $Ag_7Cu_{3.5}$, the stage I takes about 6 ps and 11.4 ps, respectively). Stage II shows the temperature-dependent neck growth with a reduced sintering rate. As

the neck grows in stage I, the curvature and surface area are reduced, i.e., sintering driving force decreases, lowering the sintering rate.

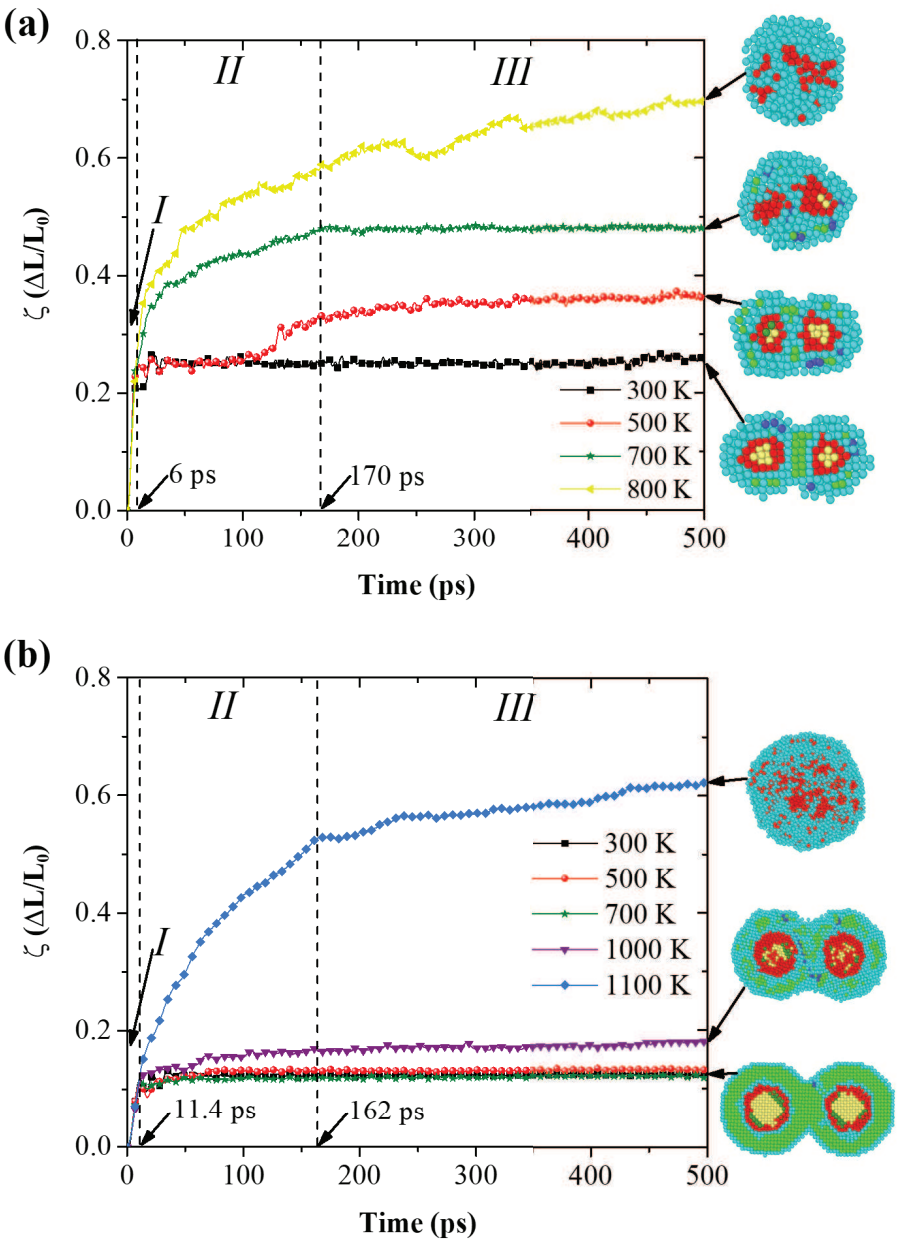

Figure 2.7: Shrinkage (ζ) of two equally sized NPs (a) $Ag_3Cu_{1.5}$ and (b) $Ag_7Cu_{3.5}$ during sintering at different temperatures. The sintered structures at 500 ps for respective temperatures are also shown. Since the sintered structures at 500 and 700 K in (b) are similar to that at 300 K, the sintered structures at 300 K is demonstrated only. The sintering process of both NPs is also characterized by three stages, indicated by dashed lines. The color scheme is the same as Figure 2.5.

During the solid-phase sintering of NP pair $Ag_5Cu_{2.5}$-$Ag_5Cu_{2.5}$ at 300 K and 500 K, the neck does not grow significantly due to the lack of diffusion mechanisms, such as surface diffusion or grain boundary diffusion. However, at 700 K, the neck grows slowly because of limited diffusion of surface atoms. MSDs in Figures 2.6c and 2.8 are used to identify the activation temperature (T_a) for the surface diffusion. MSDs reach equilibrium (constant values) below T_a (400 K, 500 K, and 700 K for NPs $Ag_3Cu_{1.5}$, $Ag_5Cu_{2.5}$ and $Ag_7Cu_{3.5}$, respectively), indicating that no surface diffusion occurs below the T_a, which confirms our finding that the plastic deformation dominates the solid-phase sintering at low temperatures. As the temperature increases above T_a, MSD increases linearly with observation time due to more vibrant atomic movement. The surface diffusion becomes a dominant sintering mechanism at a higher temperature, even below the surface-premelting temperature (T_{sm}), although the diffusivity is much smaller than liquid diffusion. The last stage (Stage III) is the equilibrium stage for solid-phase sintering. For sintering of NP $Ag_5Cu_{2.5}$ below 500 K, the shrinkage reaches equilibrium after Stage II, and then the atoms vibrate around their equilibrium positions without diffusion. Although diffusion occurs at a temperature (e.g., 700 K) above T_a while below T_{sm}, which is still within the temperature regime of solid-phase sintering, the shrinkage shows a very slow increase. As a result, the stage III at temperature below T_{sm} can also be categorized as an equilibrium stage.

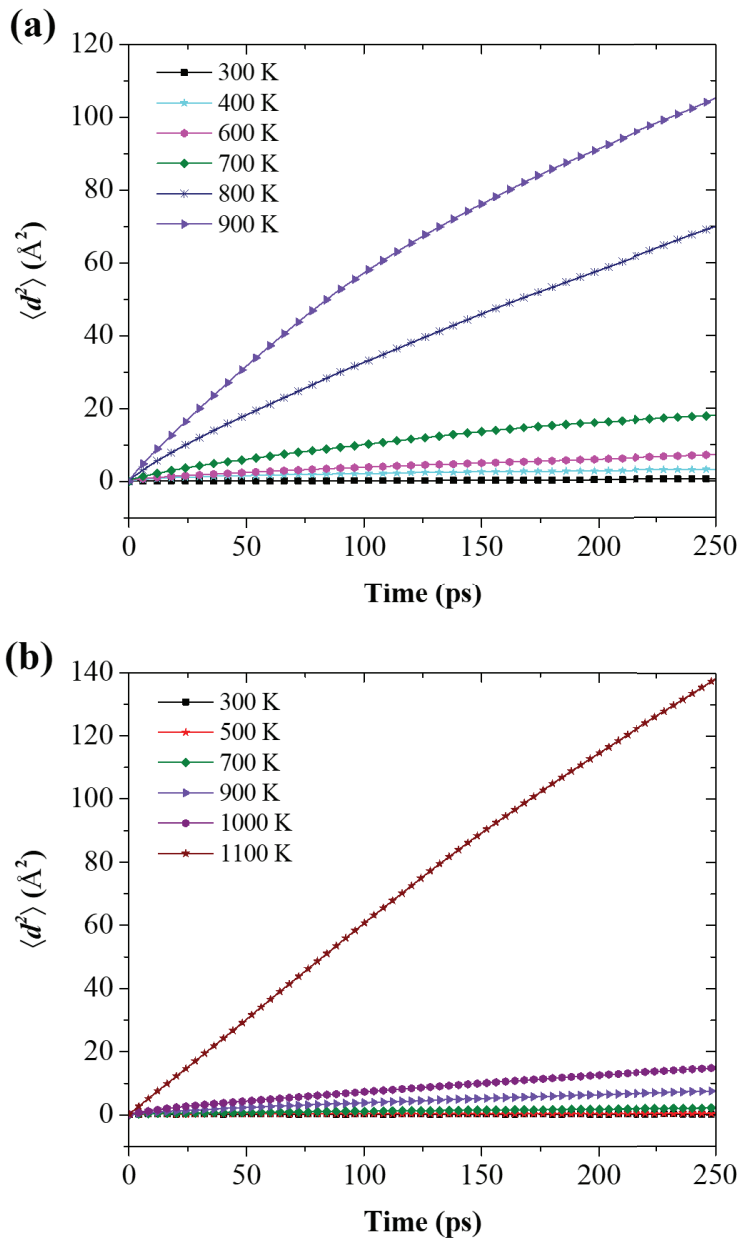

Figure 2.8: Mean square displacement ($\langle d^2 \rangle$) of NPs (a) $Ag_3Cu_{1.5}$ and (b) $Ag_7Cu_{3.5}$ during sintering process at each temperature. At 400 K (cyan star), the outermost-layer atoms in NP $Ag_3Cu_{1.5}$ have started to diffuse, and thus 400 K is determined as surface diffusion activation temperature (Ta) for NP $Ag_3Cu_{1.5}$, while for NP $Ag_7Cu_{3.5}$, T_a is determined as 700 K (olive diamond).

To reveal the sintering mechanisms in surface-premelting-induced and liquid-phase regimes, the sintering processes of NP pair $Ag_5Cu_{2.5}$-$Ag_5Cu_{2.5}$ at 900 K and 1000 K are studied [Figure 2.9]. The three-stage sintering scenario is more significant at 900 K and 1000 K [Figure 2.10a]. Stage I is independent of temperature even though the neck forms a little faster at a higher temperature due to larger KE. The crystallization-amorphization is not detected in this stage; instead, the amorphization of interfacial atoms occurs simultaneously with interdiffusion. As Figures 2.9(a) and (b) show, at the end of stage I (8 ps), atoms in the neck region are randomly located; i.e., no crystal structure is maintained. In stage II, the shrinkage is regressed below the MP, but the degree of shrinkage regression decreases as temperature increases. Above MP (1000 K), the solid phase of the NP has not remained, and thus atoms move in random directions (no specific path), causing the loss of elastic-collision-like behavior, i.e., no regression occurs. In smaller NPs, the Stage II takes a longer time since the surface premelting is pronounced even at low temperatures, which leads to a continuous neck growth. As a result, the neck size of small NP $Ag_3Cu_1.5$ sintered at 400 K has reached the diameter of initial single NP. At the end of stage II [Figure 2.9(a) at 112 ps] at 900 K, the NP maintains its CS structure, and the Cu cores are not coalescent with each other. FCC structure occupies almost 50% of all local atom orders in the core. Since the atoms in the core do not obtain enough energy to override the energy barrier at 900 K, they are trapped in the core and maintain their equilibrium positions during stage III [Figure 2.9(a) at 500 ps]. On the contrary, the sintered NPs at 1000 K form a ball-shape structure during stage II [Figure 2.9(b) at 112 ps], minimizing the surface energy. At the end of stage II, no crystal structure is maintained in the Cu core, indicating that the Cu core has completely transformed from solid to liquid phase. The atoms in the core then exhibit outer-diffusion behaviors. As a result, the core disintegrates, and the core atoms are randomly distributed, mixing with Ag shell atoms during stage III [Figure 2.9(b) at 500 ps]. This difference is evidenced by MSD, which is shown in Figure 2.10b. Diffusivity obtained from MSD curves is 0.0920 $Å^2$/ps at 1000 K, which is 16.7 times larger than the value at 900 K (0.0055 $Å^2$/ps).

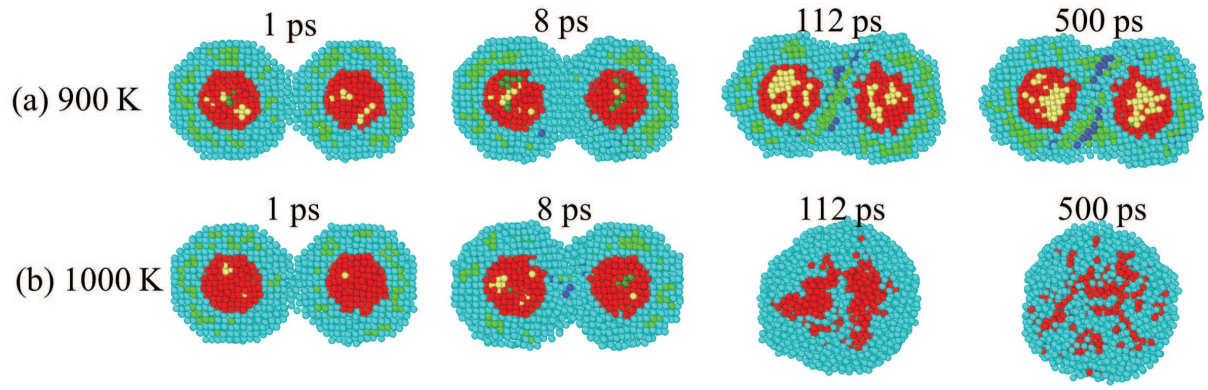

Figure 2.9: Local crystalline structural evolution of two $Ag_5Cu_{2.5}$ NPs during sintering at (a) 900 K and (b) 1000 K as illustration of surface-premelting-induced sintering and liquid-phase sintering. 1 ps is the onset time of sintering, and 8 ps and 112 ps indicate the ends of stage I and II, respectively. The local crystalline structures at 500 ps represent the stage III. The color scheme is the same as Figure 2.5.

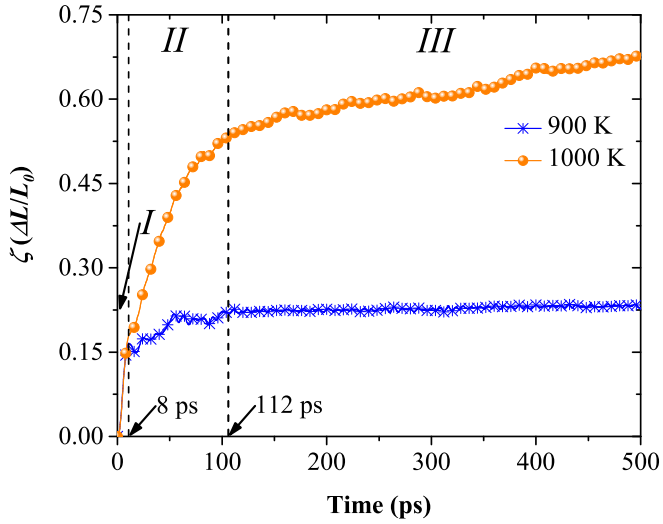

(a) Shrinkage (ζ)

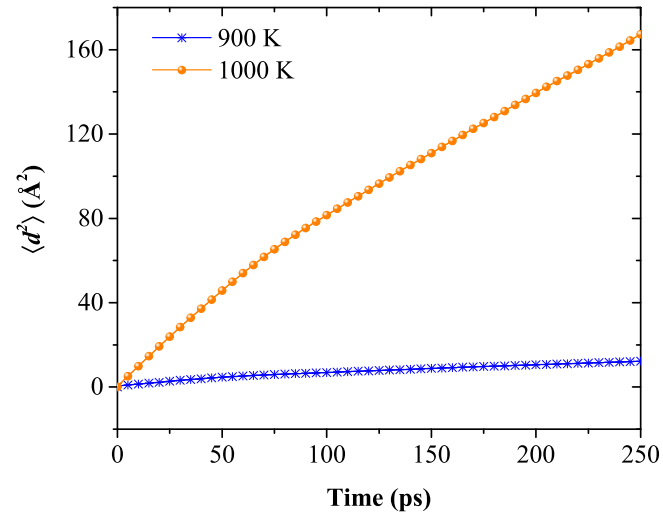

(b) Mean square displacement (MSD, $\langle d^2 \rangle$)

Figure 2.10: (a) Shrinkage (ζ) of two equal-sized $Ag_5Cu_{2.5}$ NPs during surface-premelting-induced sintering at 900 K (blue star) and liquid-phase sintering at 1000 K (orange sphere). The three stages are: (I) neck formation (1 ps) and fast growth (1-8 ps), (II) slow neck growth (8-112 ps), and (III) continuous coalescence (112-500 ps). (b) Mean square displacement (MSD, $\langle d^2 \rangle$) evolution of outermost layer atoms in NP $Ag_5Cu_{2.5}$ at each corresponding temperature. At both 900 K (blue star) and 1000 K (orange sphere), MSDs are proportional to observation time as it approaches infinity. However, the diffusivity obtained at 900 K is much smaller than that at 1000 K, which is demonstrated by the large slope difference of these two curves.

2.3.3 Sintering of Two Unequally sized NPs

Since the size of NPs is distributed, sintering of unequally-sized NPs is more frequent. For more realistic sintering, the sintering of two parallel pairs with unequally-sized NPs ($Ag_7Cu_{3.5}$-$Ag_3Cu_{1.5}$ and $Ag_7Cu_{3.5}$-$Ag_5Cu_{2.5}$) is simulated under temperatures ranging from 300 K to 1200 K (in 100 K increments).

At the beginning, the two NPs ($Ag_7Cu_{3.5}$-$Ag_3Cu_{1.5}$) approach each other, forming a neck with an amorphous bilayer. Atoms in the neck region then quickly crystallize, lowering the PE of the system (2.4 ps, Figure 2.11). Even at temperatures below T_{sm}, some of the shell atoms (within the black ellipse marked in Figure 2.11) in the smaller NPs move to the surface of the bigger NP (10 ps, Figure 2.11); here, the smaller NP has soft matter behavior and wets the bigger NP, whereas the bigger NP remains almost intact. This wetting behavior further diminishes the surface area, resulting in the decrease of the PE from 10 ps to 38 ps, and then leads to amorphization of the atoms in the neck region (38 ps, Figure 2.11). The amorphized atoms reorient themselves by clockwise rotation to achieve epitaxial layering, leading to the recrystallization (87 ps, Figure 2.11), which is similar to the initial sintering stage of equally sized NP pair $Ag_5Cu_{2.5}$-$Ag_5Cu_{2.5}$. As a result of the continuous reorientation especially in the neck region, more epitaxial layers and a final stable structure with a crystallized neck are formed (200 ps, Figure 2.11). The final sintered structures at different temperatures are listed in supplementary materials [Figures 2.12(a) and (b)]. The neck of the sintered structure of pair $Ag_7Cu_{3.5}$-$Ag_3Cu_{1.5}$ reaches the size of the smaller NP even at room temperature, as a result of the wetting behavior. However, the Cu core in the smaller NP is still maintained until the MP. At temperatures above the MP, the smaller NP shows a higher wettability, and the atoms spread across the surface of larger NP [1000 K, Figure 2.12(a)]; finally, a ball-shape structure is formed [1200 K, Figure 2.12(a)]. Note that although sintering of $Ag_7Cu_{3.5}$-$Ag_3Cu_{1.5}$ NPs at 300 K is a complete solid-phase sintering, the surface atoms are more active due to the existence of Cu core and the ultrafine size of the small NP, so the wettability of NP $Ag_3Cu_{1.5}$ at 300 K is partially attributed to the strong surface atom movement. Wettability is less significant as the size difference decreases. The

solid-phase sintering process of pair $Ag_7Cu_{3.5}$-$Ag_5Cu_{2.5}$ is similar to that of pair $Ag_5Cu_{2.5}$-$Ag_5Cu_{2.5}$ sintering. The smaller NP of pair $Ag_7Cu_{3.5}$-$Ag_5Cu_{2.5}$ (i.e., $Ag_5Cu_{2.5}$) starts to wet the bigger NP only at very high temperature [1100 K, Figure 2.12(b)]. This detected wettability-driven sintering coincides with the reported results [73].

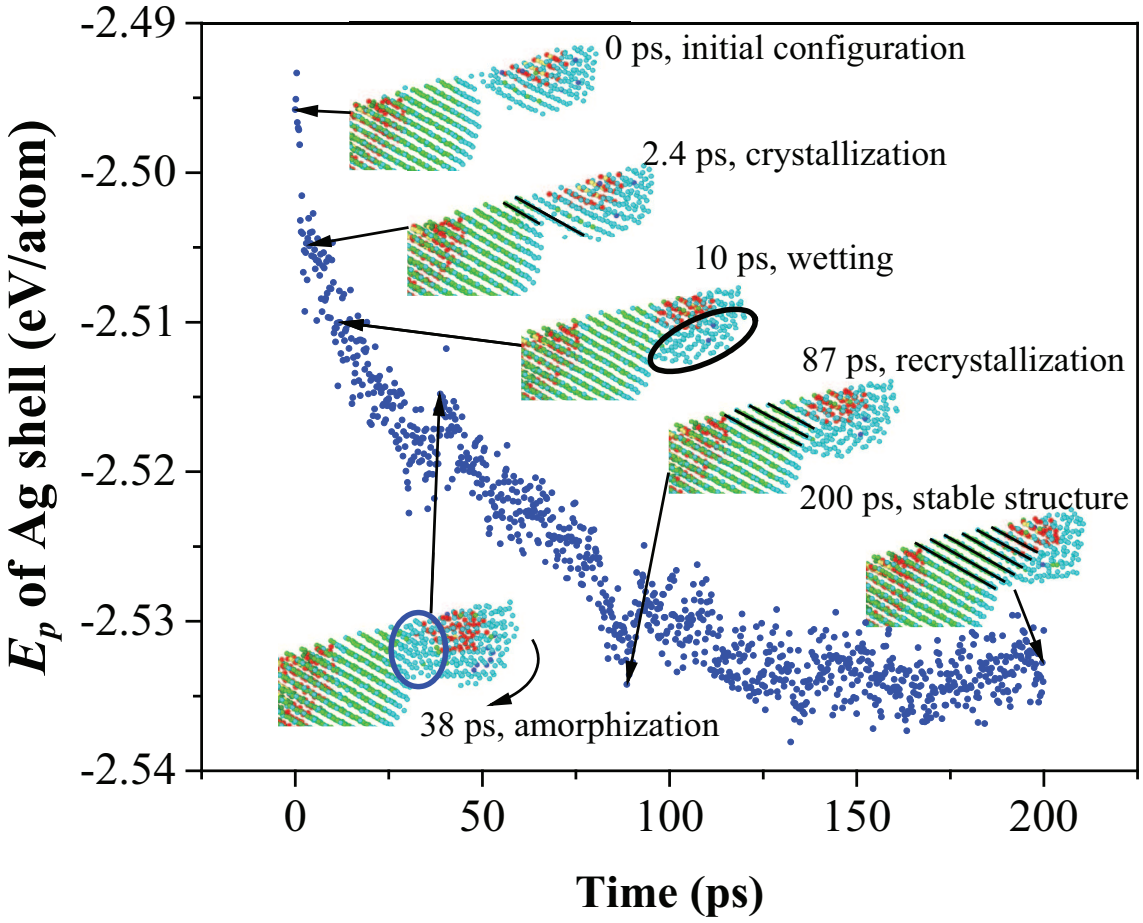

Figure 2.11: Potential energy (E_p) evolution of Ag shell in NP pair $Ag_7Cu_{3.5}$-$Ag_3Cu_{1.5}$ sintering at 300 K. The color scheme is the same as Figure 2.5.

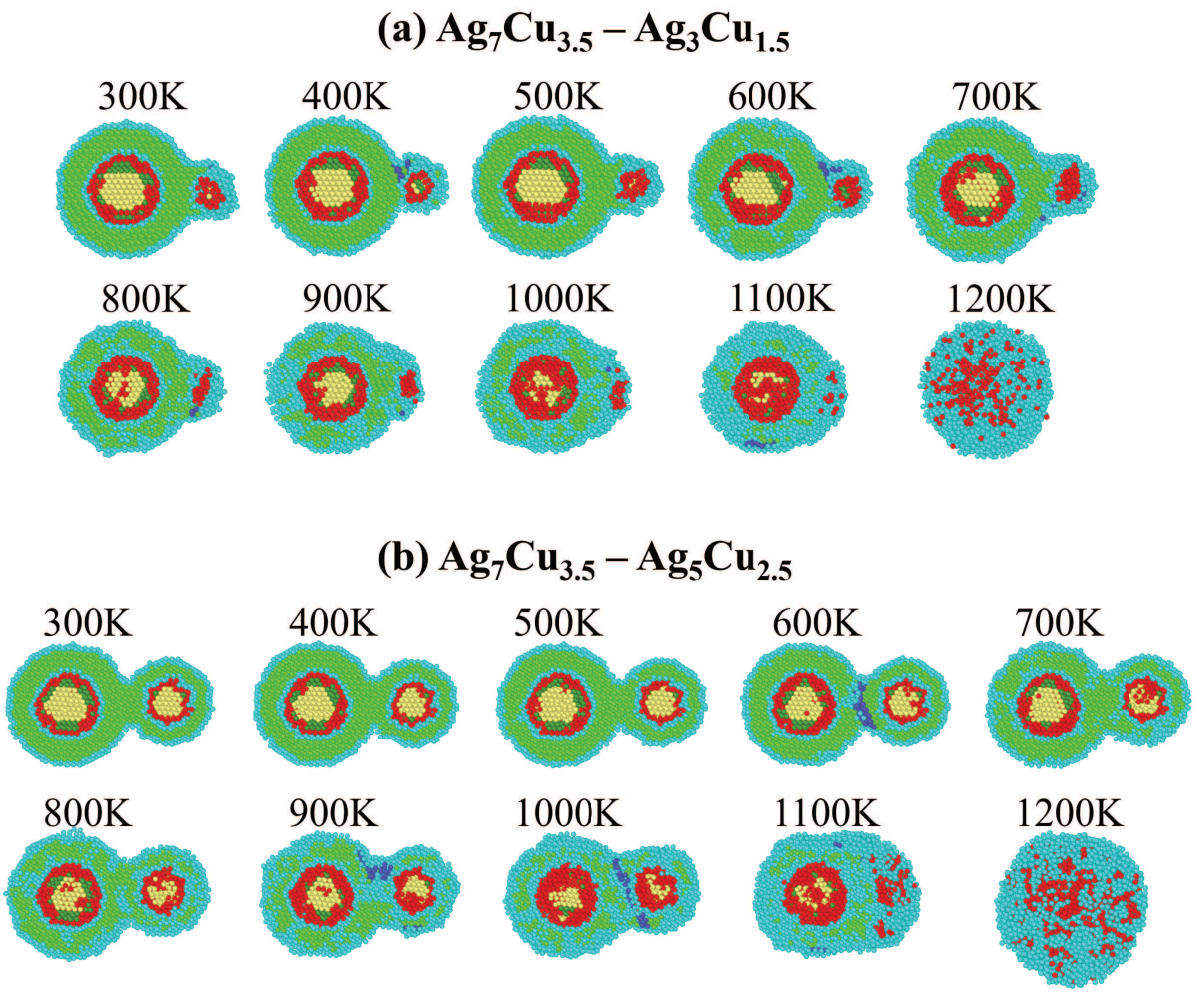

Figure 2.12: Final sintered structures of NP pairs (a) $Ag_7Cu_{3.5}$-$Ag_3Cu_{1.5}$ and (b) $Ag_7Cu_{3.5}$-$Ag_5Cu_{2.5}$ at various temperatures. The NP pair $Ag_7Cu_{3.5}$-$Ag_3Cu_{1.5}$ exhibits high wettability even at room temperature while the NP pair $Ag_7Cu_{3.5}$-$Ag_5Cu_{2.5}$ shows the wetting behavior only at 1100 K, which is above the MP of NP $Ag_5Cu_{2.5}$. The color scheme is the same as Figure 2.5.

2.3.4 Sintering of NPs with Different Core Sizes

Although the Cu cores are not coalescent during the solid-phase (Figure 2.5) or surface-premelting-induced sintering process [Figure 2.9(a)], the existence of Cu core affects the sintering dynamics. To identify the effects of Cu core, the sintering properties of three pairs of Cu-Ag CS NPs with different core sizes are compared with pure Ag and Cu NPs. The cross-sectional images of initial configurations of respective NPs are shown in Figure 2.13.

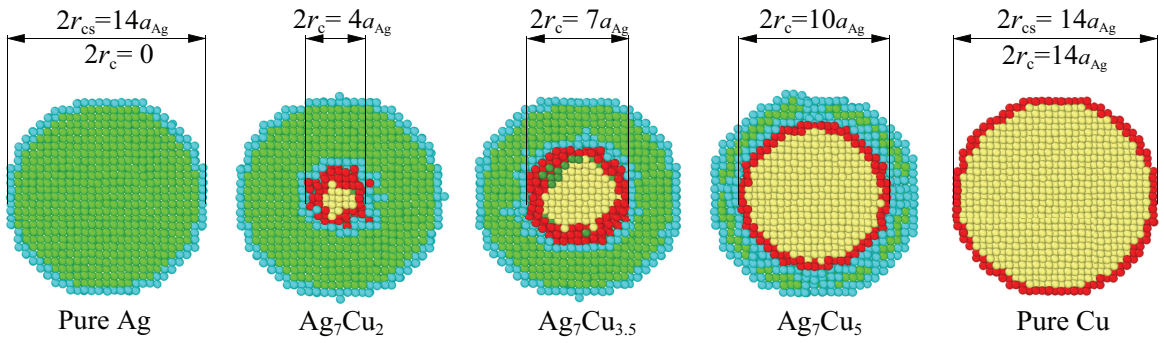

Figure 2.13: Initial local crystal orders for pure Ag and Cu NPs with radius of $7a_{Ag}$ and three Cu-Ag CS NPs with different core sizes, after relaxation at 300 K for sintering simulations. Here a_{Ag} (= 4.0853 Å) is lattice constant of Ag. The color scheme is the same as Figure 2.5. r_{cs} and r_c are CS NP and core radii, respectively.

Shrinkage is calculated during the solid-phase sintering process at 300 K, and the statistical neck sizes of the stable sintered structures are also measured. Because of the fact that different pairs have different onset sintering times, the shrinkage does not start at exactly the same time. As Figure 2.14a shows, the final shrinkage of all CS NP pairs is higher than that of pure Ag NP sintering. As shown in Figure 2.13, the Cu core induces interfacial amorphous layers of Ag shell, enhancing the mobility of the Ag shell atoms. However, the number of surface atoms in the neck region, which participate in the plastic deformation and surface diffusion, decreases dramatically as the shell thickness increases. Thus, the core size can be optimized for the shrinkage, and as Figure 2.14b shows, the core size of $3.5a_{Ag}$ in the Ag-Cu CS NP with a radius of $7a_{Ag}$ results in the maximum shrinkage and neck size (i.e., optimal core radius/shell thickness ratio is 1). To investigate the size dependency of the optimal core radius/shell thickness ratio, another five pairs of NPs, pure Ag and pure Cu

NPs with a radius of $9a_{\mathrm{Ag}}$, Ag_9Cu_2, $Ag_9Cu_{3.5}$, $Ag_9Cu_{5.5}$, are also studied (Figure 2.15) The maximum shrinkage and neck size are obtained in NP $Ag_9Cu_{3.5}$ sintering (Figure 2.16), i.e., the optimal core radius/shell thickness ratio for NPs with a radius of $9a_{\mathrm{Ag}}$ is 0.64. It is also found that small core has less influence on sintering properties to larger NPs. For example, compared with same-sized pure Ag NP, the increment in shrinkage of NP Ag_9Cu_2 is 13.67%; however, comparing same-sized NPs Ag_7Cu_2 and pure Ag, the increment in shrinkage is 34.78%. The experimental results also show that in seeded NPs, a small core size has less influence on sintering properties [74]. On the other hand, the thermal instability is found in the Cu-Ag CS structure with a very thin shell, where the shell broke into several tiny clusters [75].

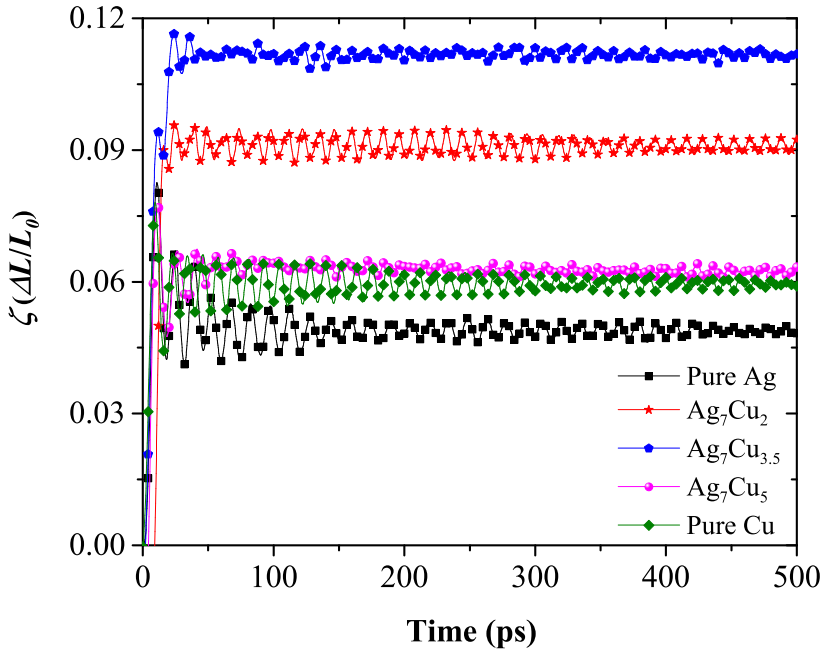

(a) Shrinkage (ζ) evolution

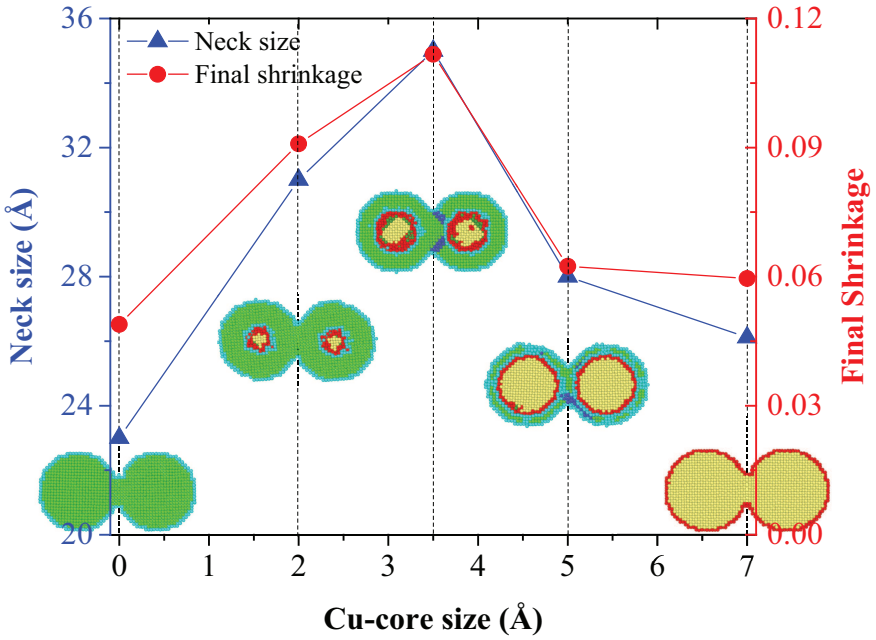

(b) Final neck size and shrinkage (ζ)

Figure 2.14: (a) Shrinkage evolution of five pairs of NPs sintering at 300 K (b) Final neck size (blue triangle) and final shrinkage (red circle) of stable sintered structures.

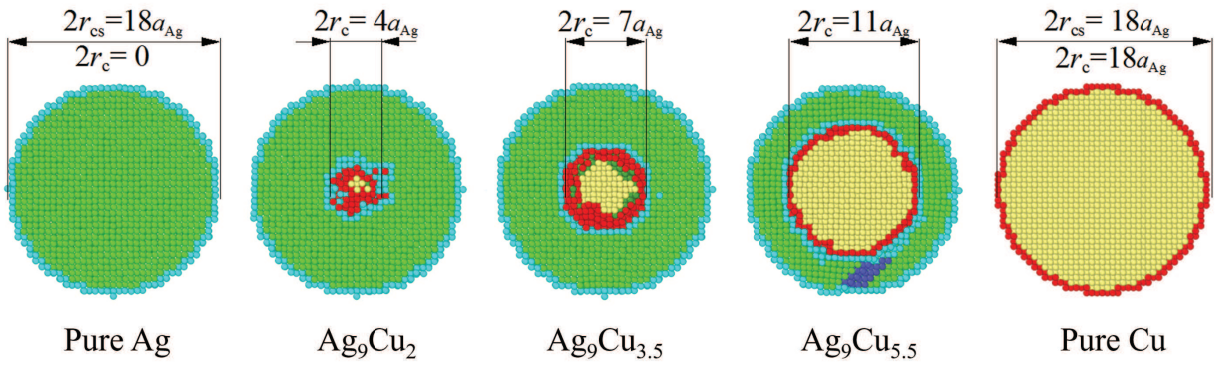

Figure 2.15: Initial local crystal orders for pure Ag and Cu NPs with radius of $9a_{\mathrm{Ag}}$ and three Cu-Ag CS NPs with different core sizes, after relaxation at 300 K for sintering simulations. Here a_{Ag} (= 4.0853 Å) is the lattice constant of Ag. The color scheme is the same as Figure 2.5. r_{cs} and r_{c} are overall particle and core radii, respectively.

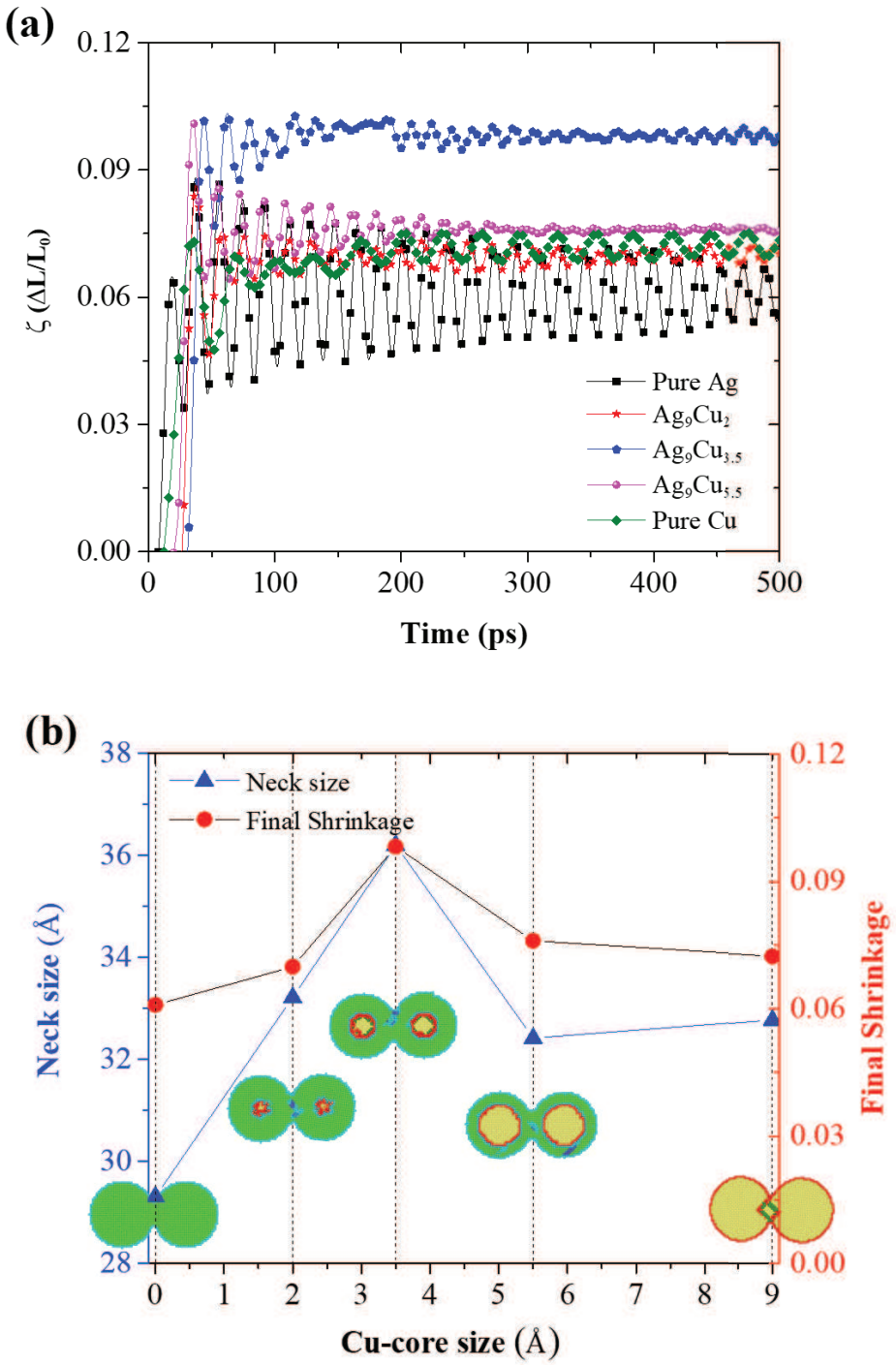

Figure 2.16: (a) Shrinkage during the sintering of five pairs of NPs with overall radius $9a_{\mathrm{Ag}}$ at 300 K. (b) Neck size (blue triangle) and final shrinkage (red circle) of stable sintered structures. The NP $Ag_9Cu_{3.5}$ has an optimal core radius/shell thickness ratio for maximum densification. The color scheme is the same as Figure 2.5.

2.4 Conclusions

Sintering mechanisms, such as reorientation, plastic deformation, and surface diffusion, are suggested in the Cu-Ag CS NP sintering process. Furthermore, two sintering mechanisms are newly found: (1) crystallization-amorphization-recrystallization during solid-phase sintering process and (2) wetting in the sintering of two unequally sized NPs induced by its own small size and existence of Cu core. The wetting is more significant as the size difference increases, suggesting that dense materials could be achieved for strong bonding strength once the discrepancy in NPs' size is large. The Cu core enhances the mobility of the Ag shell atoms, thus enhancing the sinterability and sintering strength, which is demonstrated by larger shrinkage. Optimal core radius/shell thickness ratio, which is proposed to achieve maximum densification at room temperature, decreases as NP size increases.

Through this study on sintering dynamics of CS NPs with different geometries, the roles of core in sintering are identified, and the effective structures for sintering are suggested; these enable accurate control of sintering process and achieve strong bonding strength in industry. Furthermore, this paper provides a significant basis for selecting appropriate temperature to sinter different-sized CS NPs. Further insights into the maintenance of desirable CS nanostructures during sintering or heat treating processes are also achieved. For additional enhancement in understanding of the Cu-Ag CS NP sintering, the morphology, pressure and crystallographic orientation effects on the sintering mechanisms and quantum size effects in small clusters can be studied further. More comprehensive evaluation of the mechanical, thermal and electrical properties of the sintered structure will also be conducted in the future.

Chapter 3

Room Temperature Nanojoining of Cu-Ag Core-Shell Nanoparticles and Nanowires

Note: Chapter 3 is a modified version of the publication: **Jiaqi Wang** and Seungha Shin*, "Room temperature nanojoining of Cu-Ag core-shell nanoparticles and nanowires", Journal of Nanoparticle Research, 19, 53 (2017).

3.1 Introduction

Nanoparticles (NPs) and nanowires (NWs) have been widely applied in optical, electrical, and biomedical nanosystems, such as optical logic gates [76, 77, 78, 79], photovoltaic cells [80], and bactericidal materials [81]. Among them, Ag nanomaterials have been broadly utilized in printed electronics [82] and electronics packaging [83] due to the high thermal and electrical conductivity as well as oxidation stability [84, 85]. However, the high cost of Ag has hindered the commercial promotion of nanotechnologies involving Ag. As an alternative to pure Ag nanomaterial, Cu has been considered since the price of Cu nanopowder is much lower than that of Ag and has comparable thermal and electrical conductivity to Ag. In order to prevent the oxidation for the excellent thermal and electrical conductivities, a NP with Cu core/Ag shell structure is conceived and synthesized by researchers [86, 82]. This

core-shell structure is thermodynamically favorable due to phase separation (the Ag tends to deposit on the surface) induced by higher surface energy, weaker cohesion, and larger atomic size of Ag [87]. This core-shell structure can be formed by the Ag wetting on the Cu NPs, and surface diffusion along the Cu surface since the surface diffusivity is much higher than the bulk diffusivity [88].

Sintering or joining of nanomaterials has been used as a convenient technique to build up nanostructure blocks [88, 89, 90]. Nanomaterials have higher specific surface energy, due to higher fraction of surface atoms with low coordination number, compared with their bulk counterparts, which induces high sensitivity to heat input. Consequently, conventional joining methods such as laser welding [91, 92], soldering [93, 94], and ultrasonic bonding [95] with high thermal energy input can possibly cause damage to the micro or nanoscale electronic components, where their original morphology should be maintained. However, room temperature (T_{room}, 300 K) nanojoining technology does not involve heating or fusion at the interface. Therefore, the quality of the nanojoint is high due to absence of local heating. In addition, the low-cost of the T_{room} joining makes it a promising academic and industrial field to develop technology producing reliable nanojoint. However, according to our best knowledge, study on joining process of Cu-Ag core-shell (CS) NW has never been reported and understanding in the CS NP joining is still immature. Due to the existence of Cu core, mobility of shell atoms may be alternated, distinct coalescence process and properties of final joined structures are also expected. Differing from the CS NPs, Cu directly participate in the joining process of NW in end-to-end configuration, which may also result in distinct joining processes due to the discrepancy in the cohesive energy of Cu and Ag.

In the present work, we conduct theoretical analysis on joining process with molecular dynamics (MD) simulation of three pairs of NPs and one pair of CS NWs. Following this introduction, simulation and analysis methodology are presented. In the Results and Discussion (section 3.3), the thermal stability of CS NP and NW, joining dynamics of NP and NW with different geometries are analyzed. To test the reliability of the nanojoint in the joined NWs, a uniaxial tensile test is performed.

3.2 Methodology

3.2.1 MD Simulation Implementation

The constructed embedded atom method (EAM) potential [96], through combining the existed EAM potentials for Cu and Ag, is selected as the force field to describe the interactions between Cu and Ag atoms. It has been proved that the Cu-Ag phase diagram and high-temperature properties calculated with this binary EAM potential agree well with experiments. As a result, it is convincing that this EAM potential can produce accurate simulation results over broad temperature ranges, although in this research we only conduct the joining simulations at T_{room}.

Pure Ag NP, Cu-Ag CS NP and Cu-Ag CS NW are modelled and employed as our simulation subjects. The detailed geometry information of these three nanostructures will be addressed in the subsection 3.3.1 of Results and Discussion. Before joining simulation, each nanostructure is relaxed at T_{room} for 50 ps, so as to eliminate any effect induced by the instability of initial structure. All simulations are conducted in NVT canonical ensemble (constant number of atoms, system volume and temperature) with Nosé-Hoover thermostat for maintaining the system at T_{room}. Periodic boundary condition is applied for both the upper and lower boundaries in three dimensions. A vacuum layer in simulation cells is large ($>$ interaction cutoff radius, 8.995 Å) enough to ignore interactions with NPs or NWs in other periodic images. Thus, the periodic boundary condition applied here works as the non-periodic boundary condition. The equations of motion are integrated with time step of 1 fs, using the Verlet algorithm, and 1 fs has been validated to conserve energy well in NVE microcanonical ensemble (constant number of atoms, system volume and energy). The duration of the joining simulation is 500 ps. Although the complete joining process cannot be achieved within this time scale, various phenomena in the early stages of the joining process including neck formation, neck growth, and densification, can be understood through these MD simulations. In order to investigate the thermal stability of the nanostructures and validate our simulation methodology, melting temperatures (T_{m}'s) of these nanostructures are determined and compared with reported computational and experimental results.

For studying the mechanical properties of the NW joint, a uniaxial tensile test is performed with a constant engineering strain rate (e_{rate}) of 0.03 ps^{-1}. The box length L in x dimension as a function of time t will change as follows:

$$L(t) = L_{x\_0} \times (1 + e_{\text{rate}} \times \Delta t) \tag{3.1}$$

where L_{x_0} is the original length in x dimension, and Δt is the elapsed time of the tensile test. In this simulation, tensile test is performed for 60 ps (i.e., total Δt is 60 ps). The x dimension of simulation box is updated every time step (1 fs), meaning that the box length is increased by ($L_0 \times 3 \times 10^{-5}$) Å every time step. The total deformation of simulation box in x dimension is ($L_0 \times 1.8$) Å, which is long enough to break the joined NW. The stress tensor of each atom in x direction is calculated and summed every 0.2 ps. All aforementioned simulations of joining, melting and tensile tests are conducted with LAMMPS code [47] and partial simulations are relied on the Extreme Science and Engineering Discovery Environment (XSEDE) resources [48].

3.2.2 Analysis Methods

The analysis methods employed in this research are similar to those in the section 2.2 of chapter 1. Potential energy (E_p) and Lindemann index (δ_{LI}) are applied to determine the T_m; shrinkage is used to characterize the sintering stages of both NPs and NWs; and the local crystalline structural evolution is identified through the common neighbor analysis (CNA).

3.3 Results and Discussion

3.3.1 Thermal Stability of NPs and NWs

The detailed geometries of the relaxed pure Ag NP, Cu-Ag CS NP and NW are shown in Table 3.1 and Figure 3.1. The NP and NW are denoted as NP-Ag$_x$Cu$_y$ and NW-Ag$_x$Cu$_y$, respectively. The x and y are the times of lattice constant of Ag (a_{Ag} = 4.0853 Å). Both the pure and CS NP has an overall radius (r_{cs}) of $6a_{\text{Ag}}$, and the core radius (r_{c}) of CS NP

is $3a_{Ag}$, while the r_{cs} of NW is $5a_{Ag}$ and the r_c of NW is $2.5a_{Ag}$. Thus, the pure Ag NP, CS NP, and CS NW are denoted as NP-Ag_6Cu_0, NP-Ag_6Cu_3, and NW-$Ag_5Cu_{2.5}$, respectively.

Table 3.1: Initial configures after equilibration of (a) pure Ag NP (NP-Ag_6Cu_0), (b) Cu-Ag CS NP (NP-Ag_6Cu_3), and (c) Cu-Ag CS NW (NW-$Ag_5Cu_{2.5}$) for melting and joining simulations

NP/NW type	Shell thickness/Å	Core radius/Å	#Cu atoms	#Ag atoms
(a) NP-Ag_6Cu_0	$6a_{Ag}$	0	0	3589
(b) NP-Ag_6Cu_3	$3a_{Ag}$	$3a_{Ag}$	627	3130
(c) NW-$Ag_5Cu_{2.5}$	$2.5a_{Ag}$	$2.5a_{Ag}$	2179	4400

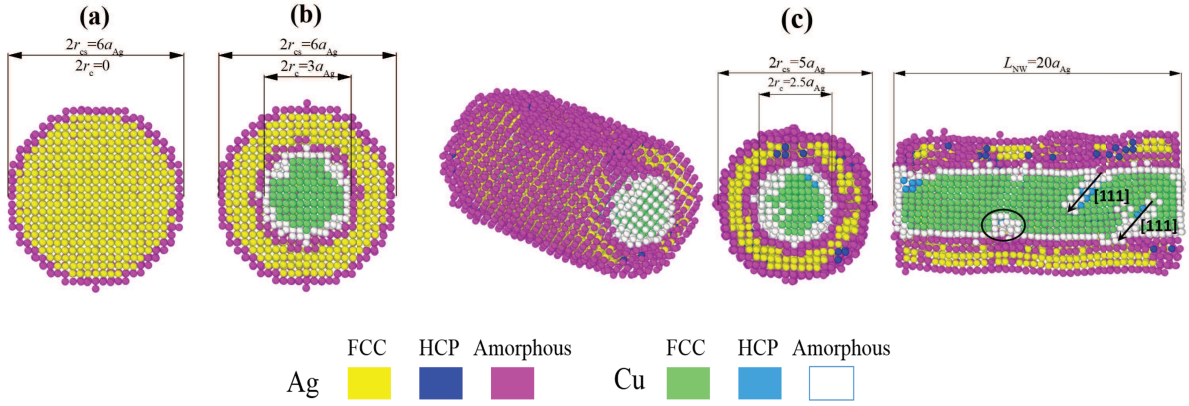

Figure 3.1: Initial configurations of (a) pure Ag NP (NP-Ag_6Cu_0), (b) Cu-Ag core-shell NP (NP-Ag_6Cu_3), and (c) Cu-Ag core-shell NW (NW-$Ag_5Cu_{2.5}$).

The NPs are obtained by cutting spherical NPs from FCC lattice, and then are equilibrated at T_{room} for 50 ps. The potential energy (E_p) evolution of these three structures during the equilibration process shows almost constant E_p before 50 ps, indicating the stability of the nanostructures, as shown in Figure 3.2. This quasi-stable nanostructure with Cu core after equilibration is employed as an initial structure for sintering, although this differs from the reported icosahedra structure [97, 98, 87, 99] due to insufficient relaxation time. This spherical nanoparticle has much smaller terraces, more edges, and kinks compared with the icosahedra cluster surface in FCC equilibrium nanoparticles, which may strongly alter the mobility of surface atoms, thus the surface melting mechanisms and joining mechanisms in initial stage. As a result, the melting and joining of the nanostructure is

not initiated from optimal structures. However, it can provide fundamental understanding in temperature and size effects on sintering dynamics, since sintering of different-shaped NP (quasi-spherical, decahedral, etc.) is also possible in experiment.

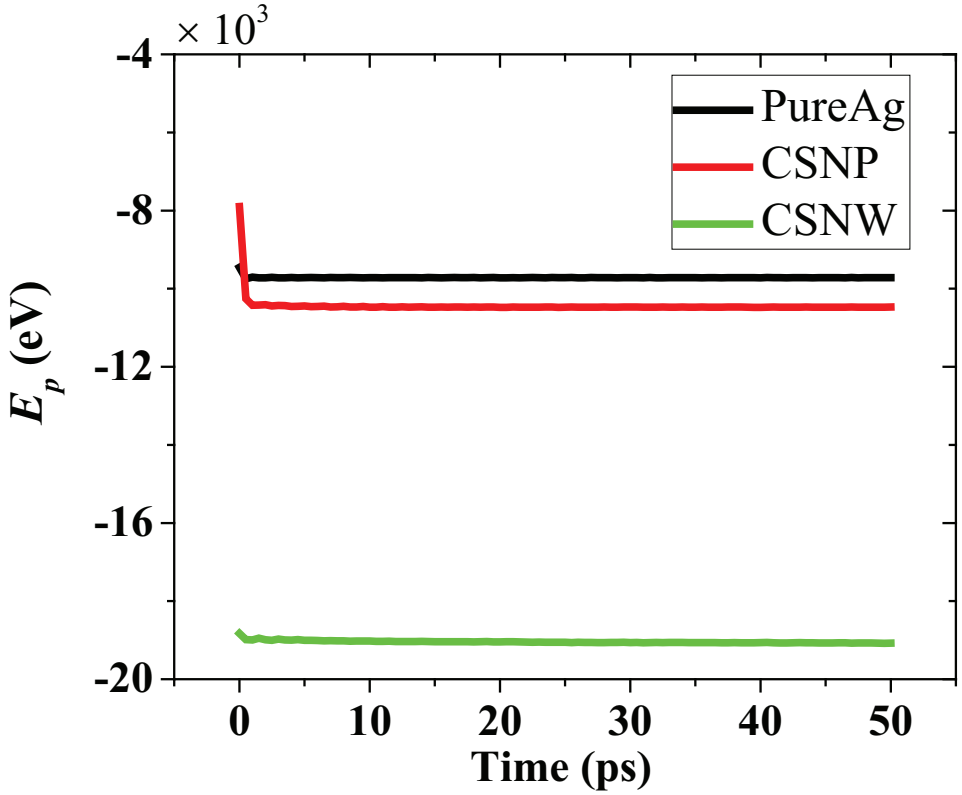

Figure 3.2: Potential energy (E_p) evolution of all NP-Ag_6Cu_0, NP-Ag_6Cu_3 and NW-$Ag_5Cu_{2.5}$ during the equilibration process for 50 ps.

Atoms of the equilibrated structures are rendered with different colors according to local atom orders analyzed by the conventional CNA with fixed cutoff radius. As shown in Figure 3.1, the surface atoms are amorphous due to low coordination number since the spherical shape introduces smaller terraces, more edges and kinks, while atoms located between the surface and the interface are still in FCC lattice sites. Note that differing from NP-Ag_6Cu_0, NP-Ag_6Cu_3 has another layer (in the interfacial region, except the amorphous surface layer) consisting of amorphous Ag atoms induced by existence of Cu core, which could enhance the mobility of the shell Ag atoms. Multiple new amorphous Ag layers are observed in CS NW since the thinner shell than NP hinders crystallization due to lattice mismatch between Cu and Ag. In CS NW, amorphous Cu atoms appeared mostly along the [111] direction induced

by large shear stress during relaxation [as indicated by arrows in Figure 3.1(c)], however, some amorphous Cu atoms appear in random directions without orientation preference [as indicated by a circle in 3.1(c)]. The defects could disappear if the core size is increased so that the crystallized structure is maintained.

The T_{m} is determined as 1060 K for NP-Ag_6Cu_0 [Figure 3.3(a)], 1100 K for NP-Ag_6Cu_3 [Figure 3.3(b)], both of which coincide well with reported simulation results of 1050 K and 1090 K [76, 77, 100], respectively, and also coincides with experimental results [101]. The tiny difference should be ascribed to measurement errors, difference in selected force field and Cu/Ag mass fraction. It is also broadly reported that the melting of the NP initials from surface layer and gradually propagates into the inner layers for pure NPs and this also occurs in bimetallic NPs if their T_{m}'s are different [76, 77, 102, 103, 104, 105]. The reported melting propagation also coincides with our simulation results: regarding NP-Ag_6Cu_0, the evolution of local orders shows that, the outer layer atoms transform from FCC order (yellow) to amorphous (magenta) ahead of the inner atoms with temperature increasing, indicating that melting propagates from surface to inner part. For NP-Ag_6Cu_3, melting propagation from surface to inner part is still the dominant scenario, while two other propagation directions are newly found: (1) inverse-propagation from interface to surface and (2) interface to inner core. These new propagation directions can be explained by the high mobility of the interfacial atoms (i.e., metastable interface), as shown in Figure 3.4(a). Due to interfacial interaction and lattice mismatch, the interface is strongly metastable and unfavorable since the Cu atoms subject to strong tensile stress [97, 106], thus the δ_{LI}'s of several Ag and Cu atoms are much higher than other atoms, even higher than the surface atoms. The normalized radial distribution stress of each atom is shown in Figure 3.4(b). The stress of the interfacial Cu atoms increases significantly compared with the Ag and inner Cu atoms. This provides a direct evidence that the activated interfacial atoms have the highest mobility at T_{room} due to the strong tensile stress. Joining dynamics is expected to be alternated by the high mobility of interfacial atoms.

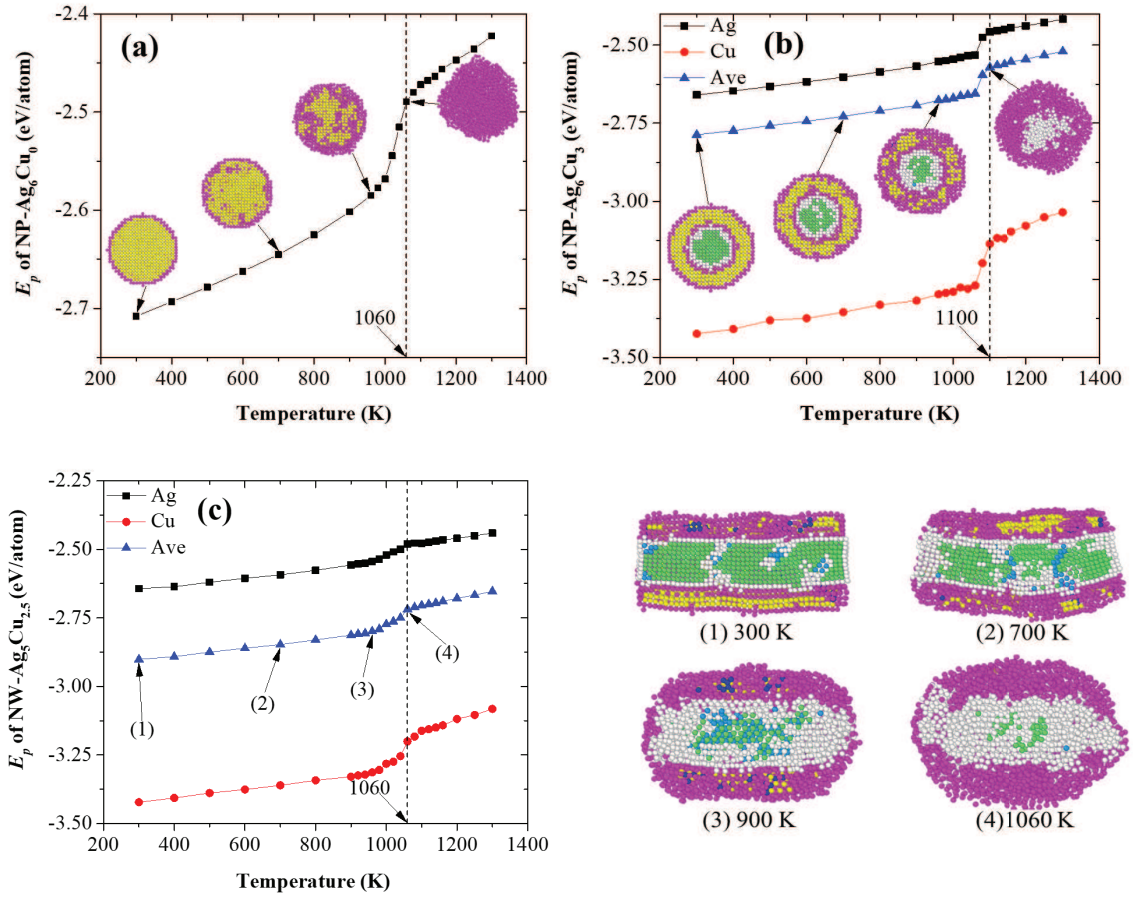

Figure 3.3: Potential energy (E_p) evolution of (a) NP-Ag_6Cu_0, (b) NP-Ag_6Cu_3, and (c) NW-$Ag_5Cu_{2.5}$, during heating process. The color scheme is the same as Figure 3.1.

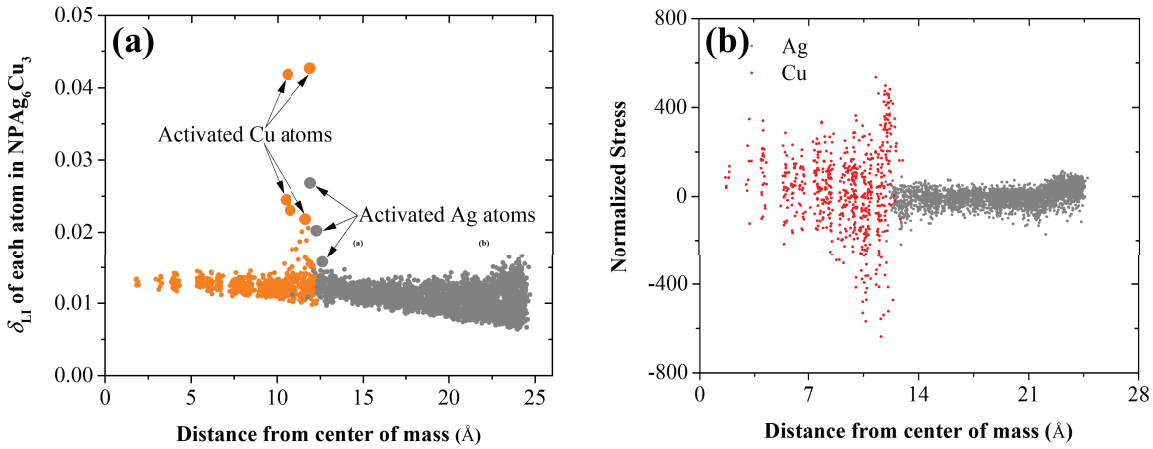

Figure 3.4: (a) Lindemann index (δ_{LI}) of each atom along the radius in CS NP-Ag_6Cu_3 at 300 K. (b) Normalized radial distribution stress of each atom in CS NP-Ag_6Cu_3. Several activated Ag and Cu atoms are found in the proximity of Ag/Cu interface.

From our simulations, the T_m of NW-$Ag_5Cu_{2.5}$ is also reported as 1060 K [Figure 3.3(c)], 40 K lower than that of CS NP-Ag_6Cu_3. The E_p evolution curve during the heating process is smoother than NP-Ag_6Cu_3 because the surface of the NW has more amorphous atoms with low coordination number [Figure 3.1(c)], i.e., NW is actually already in a quasi-liquid state, thus no distinct increase is observed as NW melts; hence, the melting occurs at a lower temperature than NP-Ag_6Cu_3.

The thermal stability of nanostructures is also important in determining the joining mechanisms. For example, at surface-premelting temperature, joining could be facilitated by surface premelted atoms [76]. Although in this research, joining simulations are only conducted at T_{room}, the thermal stability investigated here could still be potential reference for future joining research at a higher temperature.

3.3.2 Joining of NPs

Joining processes of three pairs of NPs are investigated under T_{room}. The NP pairs are Ag_6Cu_0-Ag_6Cu_0 (pair1), Ag_6Cu_3-Ag_6Cu_0 (pair2), and Ag_6Cu_3-Ag_6Cu_3 (pair3), respectively. To eliminate the effect of relative crystallographic orientation, the two NPs are placed to each other, facing [100] orientation with a distance of 4 Å (as shown in Figure 3.5), which is still within the cutoff radius of the EAM potential. Hence, the joining can be initiated by the attractive forces between the nearest surface atoms.

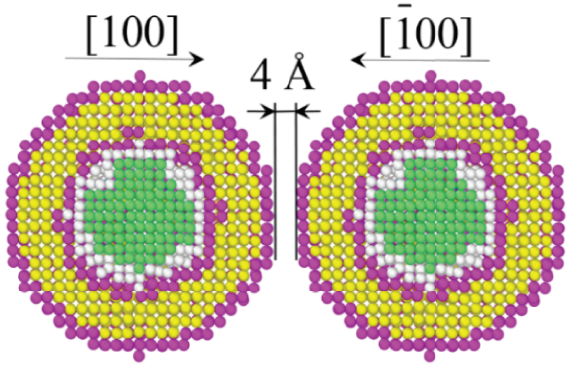

Figure 3.5: Initial configuration for joining of two NP-Ag_6Cu_3. The initial joining configurations of NP pairs Ag_6Cu_0-Ag_6Cu_0 and Ag_6Cu_3-Ag_6Cu_0 are the same as NP pair Ag_6Cu_3-Ag_6Cu_3 presented here. The color scheme is the same as Figure 3.2.

ζ and neck size are direct measurement of sinterability of NPs and can also indicate the bonding strength. Figure 3.6 shows the ζ evolution of three NPs during joining for 500 ps. The ζ is measured at the onset of joining (two NPs start to have point contact). After 500 ps, the final ζ of pairs 1, 2 and 3 are around 0.060, 0.075, and 0.120, respectively. The neck sizes of pairs 1, 2 and 3 are measured as 19.33, 23.67 and 27.23 Å, which coincide well with ζ. Obviously, the NP pair3 yields highest ζ and neck size. This is because the shell atoms of CS NP have higher mobility than pure Ag NP, induced by the lattice mismatch and interfacial interactions, which is evidenced by activated Ag atoms found in Figure 3.4.

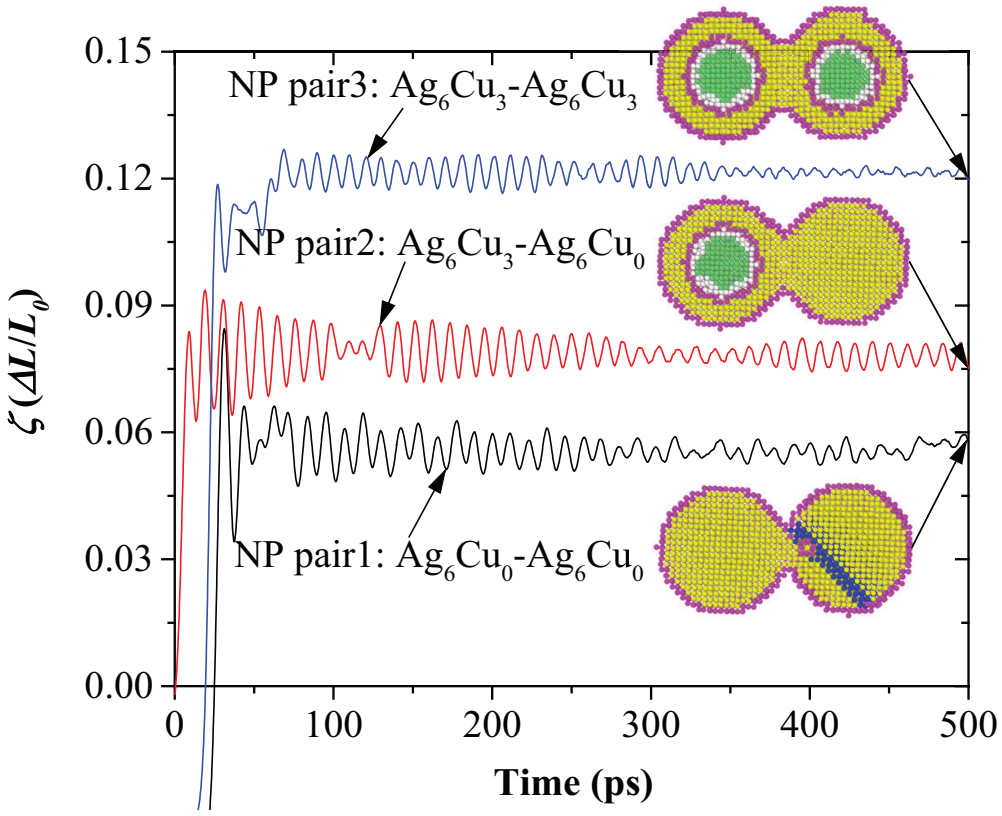

Figure 3.6: Shrinkage (ζ) evolution of three pairs of NPs during joining process. The joined structures at 500 ps are also shown.

As is known, the thermodynamic driving force for sintering is the reduction of surface energy, and it increases exponentially when a particle size decreases to nanoscale [107]. It is assumed that with larger ζ and neck size, the reduction of surface area is also larger, i.e., the reduction of surface energy is larger. As a result, we checked the E_p to see whether the calculated neck size and ζ coincide with the E_p evolution.

E_p evolutions of Ag shell and Cu core during joining at T_{room} are shown in Figures 3.7(a) and 3.7(b). It can be known that the initial E_p of three pairs is: $E_{\text{p, pair1}} < E_{\text{p, pair2}} < E_{\text{p, pair3}}$. As a result, the Ag atoms in NP pair3 has the strongest propensity of reducing the energy to reach the minimum-energy state. This also indicates that the Ag shell atoms in NP pair3 have the highest mobility. The E_p of Ag shell decreases dramatically once the joining initiates, which is induced by the annihilation of free surface during the joining process, decreasing the surface energy. However, before the E_p of Ag reaches equilibrium, it fluctuates a lot according to the structural deformation. The joining mechanism will be addressed in detail, corresponding to the E_p change in the following part.

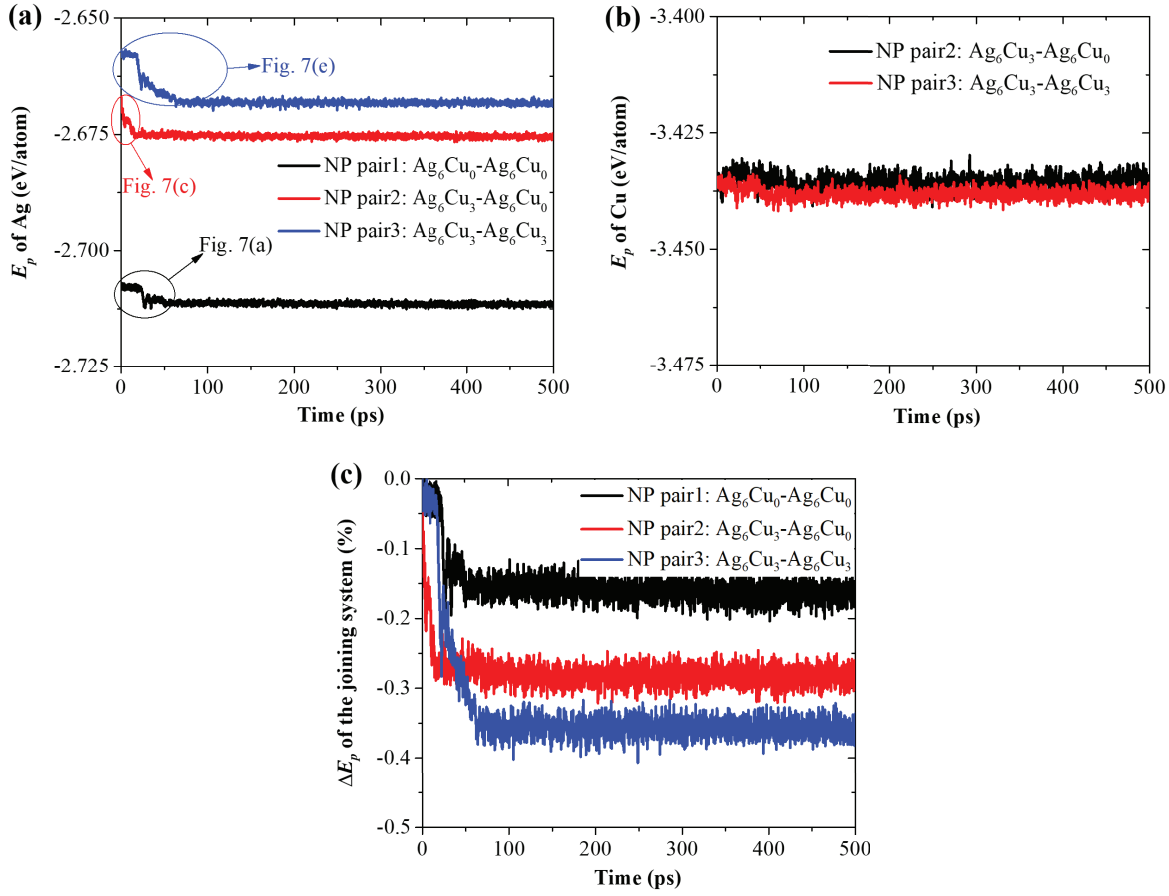

Figure 3.7: Potential energy (E_p) evolution of (a) Ag and (b) Cu in three NP pairs during joining process. In NP pair1, Cu is not included. (c) Normalized potential energy reduction (ΔE_p) of joining system at T_{room} verse time.

As Figure 3.7(b) shows, the E_p of Cu core does not show obvious decrease during the joining process, due to the fact that the Cu atoms do not participate in the joining process under T_{m}. At low temperatures, the Cu core atoms do not obtain enough energy to escape the original lattice sites and squeeze their neighbors to diffuse. Instead, they are trapped in the core and only vibrate around their equilibrium positions. Therefore, the E_p reduction (ΔE_p) of the whole system is mainly contributed by the E_p reduction of Ag shell. To compare the E_p change of the joining system, the changes in the E_p normalized by the initial E_p before joining at T_{room} is plotted in Figure 3.7(c). This figure reveals that the E_p drop during joining of NP pair3 is larger than NP pair1 and pair2, induced by the strongest propensity for reaching the energy-minimum position; i.e., NP pair3 has the largest driving force for joining. The greatest reduction observed here validates our previous finding that the NP pair3 has the largest ζ and neck size.

To have a comprehensive understanding of joining process, especially the initial neck formation and growth process, the structural deformation is characterized with respect to the E_p evolution (Figure 3.8). Before the onset of joining for all pairs, the two NPs are attracted to each other by interatomic attractive force. As they contact each other (i.e., neck formation), the E_p drops quickly since the initial neck growth is very fast. It can be generalized that the duration from point 1 to 2 [Figures 3.8(b), (d) and (f)] is neck formation and fast growth (Stage I). In NP pair1 and 2, crystallization during stage I [point 2, Figures 3.8(b) and (d)] is observed. As a result, the E_p reduction in stage I of NP pair1 and 2 is partially contributed by the crystallization of the neck region. However, for NP pair3, crystallization is absent due to lack of enough Ag atoms in neck region. It is also commonly observed that the E_p increases after stage I [point 2 to 3 in Figures 3.8(a), (c) and (e)], which is caused by amorphization [point 2 to 3 in Figures 3.8, (d) and (f)] of pre-crystallized atoms in the neck region.

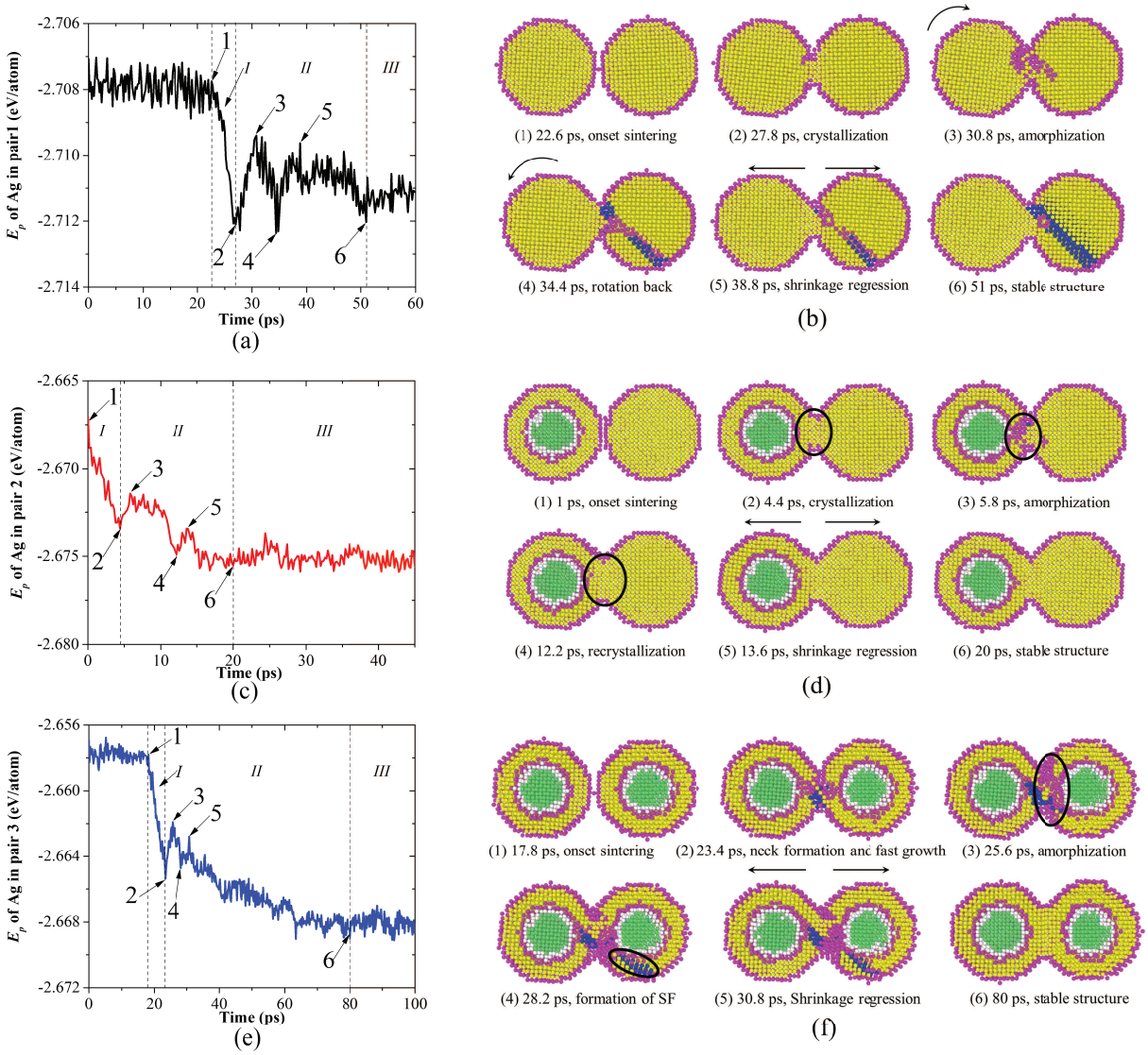

Figure 3.8: Potential energy (E_p) evolution of Ag in three pairs [(a), (c), and (e)] and characteristic structural deformation at each instant [(b), (d), and (f)].

In NP pair1, obvious clockwise rotation of the left NP occurs [point 3, Figure 3.8(b)] while atoms are finding pathways to reorient with each other. Afterwards, the left NP rotates counter-clockwise, recrystallizes and reduces the E_p [point 3 to 4, Figure 3.8(a)]. Also, SF forms with two adjacent planes of HCP atoms [point 4, Figure 3.8(b)], after nucleation and propagation of a Shockley partial dislocation through FCC crystal according to the theory of crystal dislocations [108, 109]. This SF is stable and does not disappear in the following joining process. In NP pair2, the rotation is not obvious; however, it does follow the similar pathways to recrystallize [point 4, Figure 3.8(d)] and lower the E_p of the system [point 3 to 4, Figure 3.8(c)]. In NP pair3, SF forms with two adjacent (111) planes of HCP atoms as well [point 4, Figure 3.8(f)]. The SF has higher energy than FCC crystalline structure but less energy than amorphous structure, causing the E_p reduction from point 3 to 4 [Figure 3.8(e)]. However, the SF formed in the NP pair3 is transient and gradually eliminated by the following adjustment of atom positions. After the recrystallization, ζ regression is observed in all NP pairs because the NP approaches each other with high speed, resembling elastic collision behaviors and the NPs bounce back, increasing the surface area of the two NPs. Consequently, the E_p increases a little bit [point 4 to 5 in Figures 3.8(a), (c), and (e)]. After ζ regression, the NP pairs 1 and 2 reach equilibrium [point 6, Figures 3.8(a) and (c)] within a short time (around 10 ps), while the NP pair3 takes much longer time (around 44 ps) to reach stable state through gradual elimination of SFs. We characterize the process from point 2 to 6 as transient neck growth stage (stage II), while the joining process after point 6 are equilibrium stage (stage III). During stage II of NP pair3, after the ζ regression, the two NPs are continually approaching to each other induced by the higher diffusivity of neck-region shell atoms, causing the gradual reduction in E_p [point 5 to 6, Figure 3.8(e)]. Therefore, it yields larger ζ and neck size. During the equilibrium stage (stage III), all NP pairs are repeating the bouncing behavior along the ζ direction, causing the oscillation in ζ.

3.3.3 Joining and Tensile Testing of CS NWs

Normal welding occurs at high temperature and thus involves molten metals. However, in this research we investigate the cold-welding of CS NWs at T_{room} without heating or compressing. Two CS NWs are placed in an end-to-end configuration with distance of 4

Å, similar to that of two NPs. The ζ and E_p of both Ag shell and Cu core are tracked to explain the welding behaviors [Figures 3.9(a) and (b)] and Figure 3.9(c) shows the structural evolution of NW during welding process. Both the ζ and E_p curves exhibit an obvious three-stage joining scenario of CS NWs, which is divided by joining rate indicated by the slope of ζ and E_p curves.

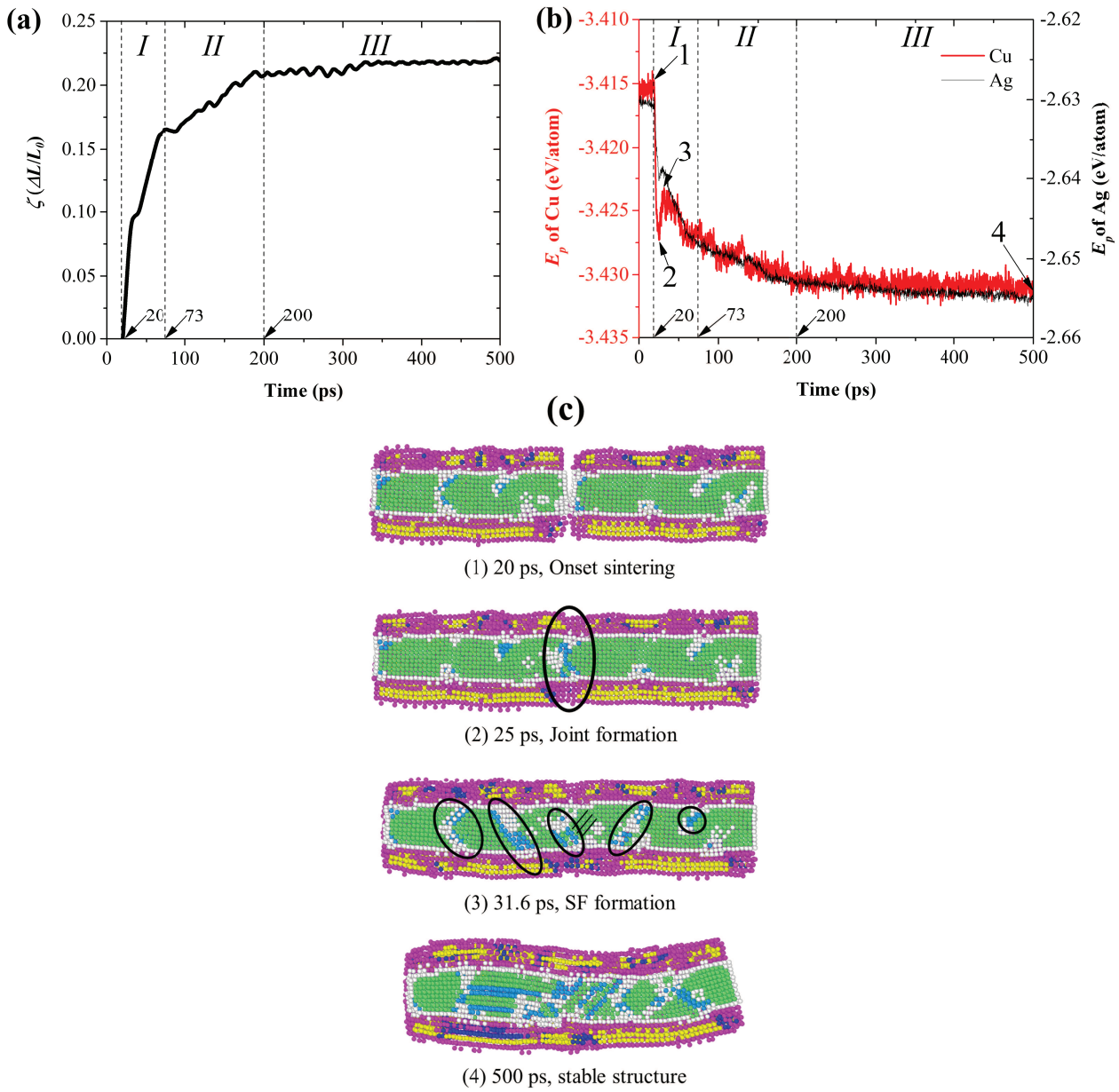

Figure 3.9: Evolution of (a) Shrinkage (ζ) (b) Potential energy (E_p) of both Ag shell and Cu core during cold welding process. A three-stage joining scenario can also be observed (indicated by I, II, and III). The 20, 73, and 200 ps in (a) and (b) are beginning time of stage I, II, and III, respectively. (c) Structural evolution of two CS NWs during end-to-end welding process at T_{room}. Image (1) shows onset joining, in image (2), a neck with size of NW diameter can be seen. Image (3) shows the formation of stacking faults (SFs). In the final joined structure (4), stable SF is observed, which are defects detrimental to electrical and thermal properties. Images (1), (2), (3), and (4) are also indicated in (b).

In stage I, once the two NWs get contact to each other, amorphous atoms located in two ends quickly crystallize and form HCP structures, reducing the surface energy from point (1) to (2) [Figure 3.9(b)]. Process from (1) to (2) occurs faster than any other process since it is not driven by thermal activation, but large intrinsic atomic force. A joint with size of NW diameter is formed at (2), and this neck is not enlarged in the following welding process although the NWs are still approaching to each other (i.e., the size of the neck remains the diameter of the NW). After the joint formation, several SFs are observed in Cu core [image (3), Figure 3.9(c)], increasing the E_p of the Cu core [point (2) to (3) in Figure 3.9(b)]. Contrarily, SF formation is not distinguishable in Ag shell, thus the E_p increment of Ag shell is not so obvious as Cu. After stage I, NWs slow the joining rate, in that the driving force for the joining is decreased with annihilation of free surface. In the final joined structure (4), defects such as SFs can be observed, which deteriorates electrical and thermal transport properties.

To test the reliability of the nanojoint, the joined NW is stretched in x dimension by a constant engineering rate. The snapshots from (1) to (4) in Figure 3.10(a) show the structural deformation in cross-sections of the joined NWs during the stretching process with the corresponding time and strain (ε). The left NW and right NW are rendered with different colors, so that we can directly observe whether the joined NW breaks at the joint. The Figure 3.10(b) is the stress-strain curve of the joined NW. As the simulation box deforms in x dimension, the NW also elongates in x direction, and before 1.2 ps, it is elastic deformation during which the joined NW can be recovered if the strain is removed. The NW does not have too much deformation ($< 3.6\%$) in x dimension as indicated by image (2) [Figure 3.10(a)] within elastic range. Since the tensile test is performed in periodic boundary condition, several atoms in right NW run across the boundary and re-enter the simulation cell from the left side. Thus, a small fraction of atoms belong to right NW can be observed in the left NW in image (2) and (3) [Figures 3.10(a)]. The Young's modulus (E_{ym}) is determined as 8.29 GPa by fitting the curve within the elastic deformation, while the yield strength (σ_{ys}) of the NW is determined as 0.43 GPa. Since the stress curve is strain rate, temperature and size-dependent [97, 110], the obtained E_{ym} is much lower than the bulk counterparts, indicating that the NW is very easy to deform under the present conditions. Once the strain

exceeds the elastic deformation regime, the NW displays obvious elongation and necking, which initiates at 35 ps [image (3), Figure 3.10(a)]. Finally, the NW breaks at 51.2 ps [image (4), Figure 3.10(a)]. Surprisingly, the NW is fractured at different point from the joint, suggesting that the resistance to rupture at the joint can be higher than the CS NW itself.

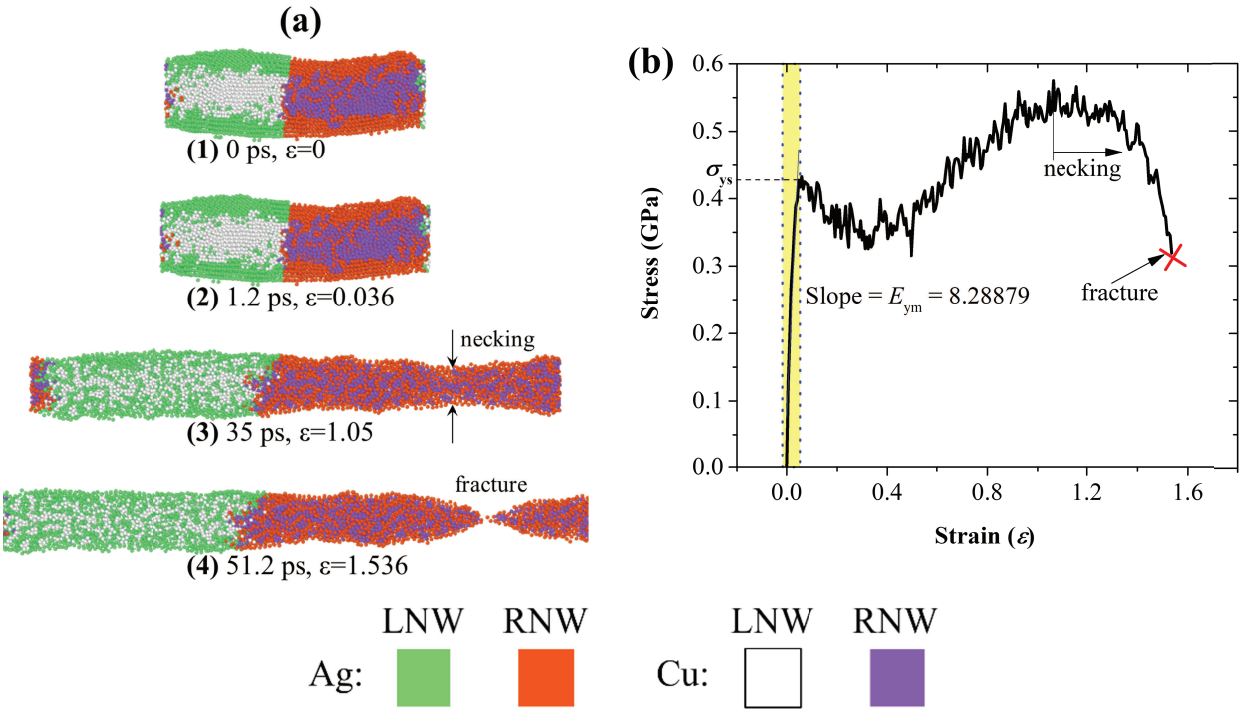

Figure 3.10: (a) Structural evolution of Cu-Ag core-shell nanojoint during the tensile test process, (b) stress-strain curve. The yield strength is determined as 0.43 GPa and the Young's modulus is 8.29 GPa. Color scheme for (a): green: Ag in left NW (LNW); red: Ag in right NW (RNW); white: Cu in LNW; purple: Cu in RNW.

3.4 Conclusions

Joining processes of Cu-Ag core-shell NPs and NWs are evaluated from the energetic perspective. Similar joining processes are proposed for both nanoparticle and nanowire: (1) fast neck formation and growth, (2) slow neck growth mainly involves plastic deformation such as amorphization of neck-region atoms and stacking fault formation, followed by (3) formation of stable joined structure with or without stacking fault. This three-stage joining scenario is determined for all nanostructures, depending on the joining rate indicated by

slope of shrinkage slope. Rupture strength of the nanojoint in the joined NW could be higher than the CS NW itself.

Through this study on joining dynamics of core-shell NPs and NWs with different geometries, the roles of Cu core in joining, which enhances the mobility of the Ag shell atoms, are identified, and the effective configurations for joining are suggested; these may enable accurate control of joining process and strong bonding strength for improvement of industrial applications such as conductive films and electrodes. For additional enhancement in the Cu-Ag CS NP or NW joining and more comprehensive evaluation of the structure, the morphology and crystallographic orientation effects on the joining mechanisms, mechanical, thermal and electrical properties of the joined structures, as well as quantum confinement effects in small clusters, can be further studied.

Chapter 4

Sintering of Multiple Cu-Ag Core-Shell Nanoparticles and Properties of the Nanoparticle-Sintered Structures

Note: Chapter 4 is a modified version of the publication: **Jiaqi Wang**, and Seungha Shin*, "Sintering of multiple Cu-Ag core-shell nanoparticles and properties of nanoparticle-sintered structures", RSC Advances, 7, 21607-21617 (2017).

4.1 Introduction

The miniaturization of electronic devices increasingly motivates the development of nanotechnology in synthesis, assembly, and the joining of metallic nanoparticles (NP) [111, 112, 113, 114, 115, 116, 117]. Among them, Ag NP has been widely produced and employed in fabrication of flexible and low-cost electronic devices through sintering, where high thermal and electrical conductivities are required [118, 119, 120, 121, 122]. However, the cost of Ag has increased significantly over the last few years and is not projected to display a reduction trend in the near future [123], which has limited the wide industrial applications of Ag NP. Thus, Cu-Ag core-shell (CS) NP has been synthesized as a potential alternative to pure

Ag NP [25, 124, 125]; this allows for tremendous reduction of production costs, enhanced protection of the Cu core from oxidation, and thereby maintaining the desirable thermal and electrical properties for electronic applications.

Joining of the CS NP has been widely used as a bottom-up nanotechnology to provide permanent unions or connections to form functional nanodevices [126, 127, 128]. The main challenge to nanojoining lies in the formation of a robust junction between NPs with excellent mechanical, thermal, and electrical performances. Understanding the underlying sintering mechanisms of NPs can enhance the performance of the sintered structure through manipulation of temperature, pressure, heating rate, NP size or relative crystallographic orientation. Numerous studies have been conducted on the sintering process of NPs both computationally and experimentally [129, 130, 131, 132, 133, 134]. While most studies have focused on the monometallic two- or three-NP sintering model, the sintering process of multiple bimetallic Cu-Ag CS NPs is still relatively unexplored. The two- or three-NP sintering model is valid for loosely packed NP sintering in gas phase or on substrates, but they overlook important factors that affect sintering dynamics and the properties of sintered structures [135]. For instance, agglomeration and pore effects, which significantly contribute to the sintering rate and porosity of final sintered structures, are neglected in the two-NP model. Consequently, the sintering mechanisms and properties of sintered structures of multiple NPs are different from a two- or three-NP model [136]. Therefore, a model containing pores to simulate the real case is essential for elucidating the sintering mechanism of the porous structure and studying the porosity dependency of sintered structure properties.

As an initial attempt, we developed a multiple-CS-NP sintering model with molecular dynamics (MD) simulation to gain an insight into the nanoscale sintering process by monitoring the atomic movement [137, 134, 138]. Our model takes into account the effects of NP size and temperature in this research; we plan a further extension of this model to reveal the effects of pressure, size distribution, and crystallographic orientation on the sintering process. The sintering simulations using the monometallic multiple-NP model have been confirmed to be very effective for reproducing the sintering process in porous anodes [139, 134]. With this multiple-CS-NP model, the sintering dynamics of CS porous structure at one atmospheric pressure but various temperatures, as well as mechanical and

thermodynamic properties of sintered structures, are investigated effectively. Following this introduction, the methodology of simulation and analysis is displayed. In the Results and Discussion (section 4.3), the sintering dynamics and sintered structure properties are analyzed and compared between (1) different-sized multiple-CS-NP models, (2) two-CS-NP and multiple-CS-NP sintering model, and (3) the bimetallic Cu-Ag CS NP model and monometallic pure Ag NP model. Implications and future work are elucidated in our conclusion.

4.2 Methodology

4.2.1 Modelling of Multiple CS NPs

Differing from the two-CS-NP sintering model, the multiple-CS-NP model possesses more degrees of freedom. Although particle packing arrangement can the affect sintering rate due to different numbers of contacting points [136, 140], the sintering rate is not a main focus of this research and it is formidable and unnecessary to test all possible arrangements. Therefore, among various packing arrangements [e.g., simple cubic (SC), body-centered cubic (BCC), face-centered cubic (FCC), hexagonal close-packed (HCP), etc.], we employ the SC arrangement, within which the NPs are facing each other with identical crystallographic orientation. For instance, we set the NPs facing each other with [100] orientation in this research, then no other orientations such as [111] are induced in this SC arrangement. NPs are built within a simulation box with periodic boundary conditions in all three dimensions. Compared to the two-CS-NP sintering model under non-periodic boundary condition [141], this model is more realistic, since the agglomeration and porosity effect can be directly addressed [136, 139, 134]. To simplify the simulated system, the effects of core size, and size distribution of NPs are excluded, i.e., all CS NPs in a simulation cell have the same radius and ratio of shell-thickness to core-radius.

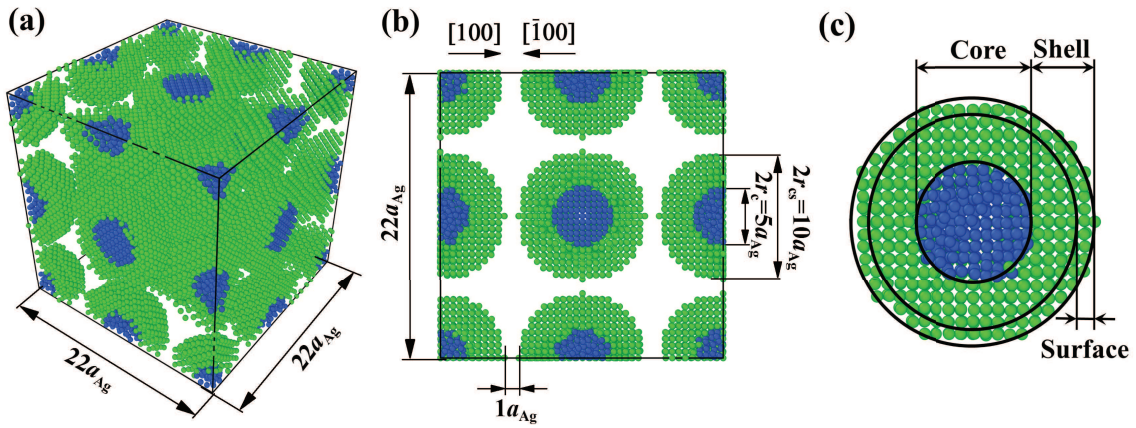

Figure 4.1: (a) 3-D view of the initial configuration for sintering simulations of multiple NP2-$Ag_5Cu_{2.5}$. (b) Cross-sectional image of (a). The initial sintering arrangements of other CS NPs are identical to NP2-$Ag_5Cu_{2.5}$. (c) One CS NP2-$Ag_5Cu_{2.5}$ extracted from (a), which is divided into three regimes (core, shell, and surface), as illustrated. The Ag shell atoms are coloured with green, while the Cu core atoms are coloured with blue.

NP is denoted as Ag_xCu_y, where x and y represent the overall NP and core radii in terms of a_{Ag}, where a_{Ag} (= 4.079 Å) is the lattice constant of Ag. Four kinds of NP are employed, they are (1) NP1-Ag_5Cu_0, (2) NP2-$Ag_5Cu_{2.5}$, (3) NP3-Ag_8Cu_4, and (4) NP4-$Ag_{11}Cu_{5.5}$. The NP1-Ag_5Cu_0 is pure Ag NP with a radius of $5a_{Ag}$, and the latter three are Cu-Ag CS NPs with r_{cs} of $5a_{Ag}$, $8a_{Ag}$ and $11a_{Ag}$ and r_c of $2.5a_{Ag}$, $4a_{Ag}$, and $5.5a_{Ag}$. Therefore, the ratio of core radius to shell thickness remains as unity in CS NPs [i.e., $r_c : (r_{cs} - r_c) = 1$].

Figures 4.1a and 4.1b show the initial sintering configuration of multiple NP2-$Ag_5Cu_{2.5}$. Eight NPs are included in each simulation box: one ($= 8 \times 1/8$) NP at eight corners, three ($= 6 \times 1/2$) at the centers of the six faces, three ($= 12 \times 1/4$) at the centers of the twelve edges, and one at the center of the simulation box. The NPs are separated by a distance of a_{Ag} to prevent atoms from overlapping. This distance is still within the cutoff radius of the interaction potential so that the sintering can be initiated by attractive forces among the atoms. For analysis of the surface and shell diffusion during sintering, the NP is divided into three regimes: Cu core, Ag shell, and Ag surface (Figure 4.1c); their atomic distances (r) from the center of mass are in the range of $0 < r < r_c$, $r_c < r < r_{cs}$, and $(r_{cs} - a_{Ag}) < r < r_{cs}$, respectively.

4.2.2 Simulation methodology

In this research, all the simulations are performed utilizing the LAMMPS code, and the Extreme Science and Engineering Discovery Environment (XSEDE) resources are employed for partial simulations [47, 48]. The embedded atom method (EAM) potential [142] is applied for describing the interactions between Cu and Ag atoms [143]. This potential has been proven to accurately calculate the cohesive energy, lattice parameters, elastic constant, phase diagram and high-temperature properties of Cu and Ag. A timestep of 1 fs is chosen for all simulations, and Newton's equation of motion is integrated with the Verlet algorithm [144].

Melting simulations are first conducted to determine the melting temperature (T_{m}) as well as surface-premelting temperature (T_{sm}) of different-sized NPs. The simulation methodology is validated by comparing the obtained T_{m} with other reported values. Based on the resulting T_{sm} and T_{m}, we select temperatures for sintering simulations, in which we (1) investigate the temperature and size effect on the sintering dynamics, and (2) obtain final structures sintered at different temperatures as simulation subjects for the subsequent studies of mechanical and thermodynamic properties.

Melting Simulations

For melting simulations, the system is equilibrated at 300 K for 50 ps, simulations are then continued at various temperatures ranging from 300 K to 1300 K (employing increments of 100 K from 300 K to 900 K, and increments of 20 K from 900 K to 1300 K for a closer observation near T_{m}) for 50 ps at each temperature, while recording the system-averaged potential energy (E_p) and atomic trajectories of the CS NP every 0.5 ps. Both the equilibration and data production phases are conducted in NVT canonical ensemble (constant number of atoms, volume, and temperature) with non-periodic boundary condition. E_p has been widely reported for determining the T_{m} by the sharp increase in E_p curve due to the heat absorption at the phase transition [145, 146, 147, 148]. Atom trajectories are processed to obtain the Lindemann index (δ_{LI}, Equation 2.3), which is employed to determine both the T_{sm} and T_{m}, so that verifying the T_{m} determined by E_p.

Sintering, Diffusivity and Activation Energy

Sintering of four different multiple-CS-NP systems (NP1-Ag_5Cu_0, NP2-$Ag_5Cu_{2.5}$, NP3-Ag_8Cu_4, and NP4-$Ag_{11}Cu_{5.5}$) is simulated for 800 ps. All the initial sintering processes such as neck formation, growth, and densification are observed in the simulations. We employ the isothermal-heating method in sintering simulations [149], i.e., the sintering system is kept at 300 K for 800 ps using the 300 K relaxed structure, and then kept at 400 K for another 800 ps with the same structure, until the temperature reaches 1300 K (with increments of 100 K). By applying the isothermal-heating method, temperature gradients inside the NP will be eliminated and thus heat transfer effects can be ignored. NpT isobaric-isothermal ensemble (constant number of atoms, constant pressure and temperature) is employed with Nosé-Hoover thermo- and barostat to control the system temperature and pressure (constant pressure = 1 atm at all temperatures). Sintering simulations are preceded by energy minimization on the initial multiple-CS-NP configuration with steepest decent algorithm [150]. Atom trajectory, E_p, densification (ξ, the ratio of reduction in volume of simulation cell to initial volume during sintering process), and mean square displacement ($\langle d^2 \rangle$) of surface and shell atoms are exported every 0.2 ps for further comparison and analysis. The $\langle d^2 \rangle$ is correlated with self-diffusivity (D_{self}) by Einstein's relation [151] given by

$$D_{self} = \frac{1}{2d} \lim_{\tau \to \infty} \frac{1}{\tau} \langle \{ [r(t_0 + \tau) - r_{com}(t_0 + \tau)] - [r(t_0) - r_{com}(t_0)] \}^2 \rangle \tag{4.1}$$

where d is the dimensionality, equivalent to 3 for our sintering system, τ is the elapsed observation time, $r(t)$ is the atomic position at time t, and $\langle \{ [r(t_0 + \tau) - r_{com}(t_0 + \tau)] - [r(t_0) - r_{com}(t_0)] \}^2 \rangle$ is $\langle d^2 \rangle$, which has eliminated any effect from the random center-of-mass motion caused by Nosé-Hoover thermo- and barostat. The angle brackets, $\langle \rangle$, indicate an ensemble average over all time origins t_0. Based on the above equations, the $\langle d^2 \rangle$ and D_{self} can be obtained by post-processing the atomic trajectory files. Additionally, the activation energy of surface and shell diffusion are obtained by fitting the temperature dependence of the D_{self} to the Arrhenius expression [152, 138] given by

$$D_{self} = D_0 \exp(\frac{-Q_{\text{v}}}{RT}). \tag{4.2}$$

where Q_v is the activation energy, D_0 is a pre-exponential factor, and R is the universal gas constant (= 8.314 J/K-mol).

Mechanical Properties

Before running simulations for mechanical properties, the final sintered structures (sintering products at 800 ps) are annealed from the sintering temperature (T_{sinter}) to room temperature (T_{room} = 300 K) within 100 ps, and the annealed structures are further relaxed at T_{room} for another 100 ps to obtain a fully equilibrated structure. Strain for mechanical properties is then applied by uniformly extending the x dimension of the MD cell with a constant axial strain rate of 2 × 10^{-2} ps^{-1}; i.e., extending the box length in x dimension by 2% of its original length every picosecond, followed by rescaling the new x coordinates of the atoms to fit within the new dimension. Strain (ε), stress (σ), and x, y, and z dimensions of the simulation cell are recorded every 0.2 ps during the tensile test for mechanical properties, including Young's modulus (E_{100} = dσ/dε), yield strength (σ_{YS}) and Poisson's ratio (ν_{100} = -$\varepsilon_{yy}/\varepsilon_{xx}$ = -$\varepsilon_{zz}/\varepsilon_{xx}$). Since each NP is initially placed facing other NPs with the [100] direction and did not rotate during sintering, the E_{100}, σ_{YS}, and ν_{100} obtained below T_m are regarded as those of the {100} faces in the final structures. The E_{100} and σ_{YS} are extracted from the strain-stress plots, while ν_{100} is obtained by calculating the strain ratio in the y (or z) direction and x direction (strain direction).

Thermodynamic Properties

We performed MD simulations on calculating the isothermal compressibility (β_T), volumetric coefficient of thermal expansion (α_p), and constant-volume specific heat capacity (c_v), using the equations shown as below: [153, 154, 155]

$$\beta_T = [-\frac{1}{V}(\frac{\partial V}{\partial p})]_T \tag{4.3}$$

$$\alpha_p = [\frac{1}{V}(\frac{\partial V}{\partial T})]_p \tag{4.4}$$

$$c_v = [\frac{\langle E_{p,tot}^2\rangle - \langle E_{p,tot}\rangle^2}{k_B T^2 m}]_V \tag{4.5}$$

In equations 4.3 and 4.4, V is the volume of the multiple-CS-NP system; in equation 4.5, k_B is the Boltzmann constant ($= 8.614 \times 10^{-5}$ eV/K), m is the mass of multiple-NP-sintered structure, and $E_{p,tot}$ is the total potential energy of the system. The multiple-NP-sintered structures at different temperatures are equilibrated prior to the simulations for β_{T}, similar to that in obtaining mechanical properties. Then, the multiple-NP-sintered structures are further simulated for 100 ps at T_{room} under five different pressures (81, 121, 161, 201, and 241 atm, respectively) within the NpT ensemble. As pressure increases, the multiple-NP-sintered structure is more compressed, thus decreasing the volume. The compressed volume is obtained by averaging the volume during the last 50 ps. The ratio of volume change to original volume ($-\Delta V/V_0$, where V_0 is the original volume at 1 atm) is plotted with respect to pressure change (Δp), and β_{T} is calculated using the slope of the plot obtained by equation 4.3. In simulations for α_{p} calculation, the multiple-NP-sintered structure is first relaxed at a temperature, which is 200 K lower than the T_{sinter} for 200 ps, then the temperature is increased by a step of 20 K and the system maintains at each increased temperature for 100 ps. The volume is averaged during the last 50 ps as well. The α_{p} is the slope of the $(\Delta V/V_0)$-ΔT plot. Since the c_{v} is dependent on T below the Debye temperature (215 K for Ag and 315 K for Cu, respectively) [156], we evaluate the c_{v} of all sintered structures at T_{room} using equation 4.5 after the equilibration to exclude the temperature dependency.

4.3 Results and Discussions

4.3.1 Thermal Stability of Different-Sized NPs

Sintering dynamics are affected by thermal behaviors of single NP such as diffusion, which depends on the NP shape, size, temperature, etc. For example, thermal diffusion of triangular nanoplates can be activated at T_{room}, to allow the nanoplates to self-sinter and form nanobelts with a growth-oriented capping agent [157]; while the diffusion of the Cu-Ag two-CS-NP model is not initiated at T_{room} [141]. Thus, thermal stability of NPs with various sizes is first studied under heating process by determining the critical temperatures such as T_{m} and T_{sm} according to the two aforementioned criteria: E_p (Figure 4.2a) and δ_{LI} (Figure

4.2b). Steep jumps are observed in both curves at 960 K, 1180 K, and 1220 K for NP2-$Ag_5Cu_{2.5}$, NP3-Ag_8Cu_4 and NP4-$Ag_{11}Cu_{5.5}$, respectively. The obtained T_m's for different sized Cu-Ag CS NPs coincide well with the reported computational values [158]. For further verification and comparison, we display the cross-sectional images of NP3-Ag_8Cu_4 in Figure 4.2a. As temperature increases, NP has a less crystallized structure, and the structure at the determined T_m is completely amorphous, also indicating the phase transition from solid to liquid.

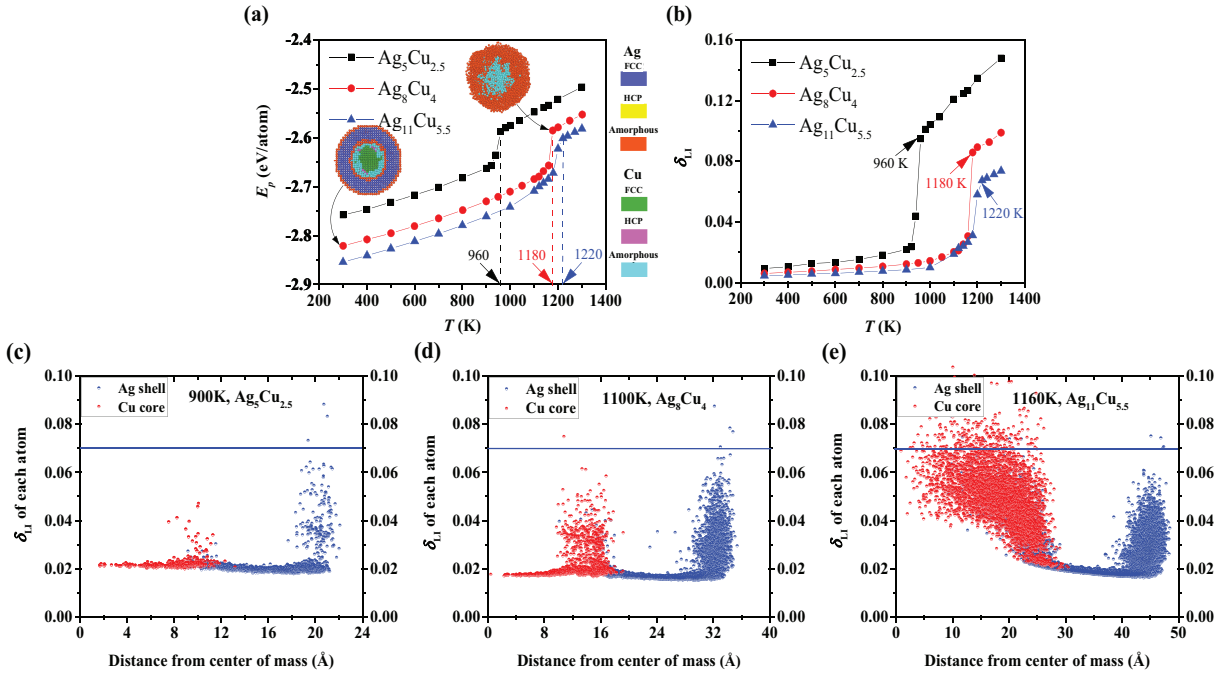

Figure 4.2: (a) Potential energy (E_p) of different-sized single CS NP during the heating process. (b) Lindeman index (δ_{LI}) of different-sized single CS NP during the heating process. The melting temperatures (T_m) determined by both the E_p and δ_{LI} coincide well with each other. Radial distribution of δ_{LI} in (c) NP2-$Ag_5Cu_{2.5}$, (d) NP3-Ag_8Cu_4, and (e) NP4-$Ag_{11}Cu_{5.5}$ at surface premelting temperature (T_{sm}).

Lindemann atom, which has δ_{LI} larger than 0.07, on Ag surface indicates that the surface is premelted. As Figure 2 shows, Lindemann atoms appear at temperatures of 900 K in NP2-$Ag_5Cu_{2.5}$ (Figure 4.2c), 1100 K in NP3-Ag_8Cu_4 (Figure 4.2d), and 1160 K in NP4-$Ag_{11}Cu_{5.5}$ (Figure 4.2e). These temperatures are determined as T_{sm}. Since the pure Ag NP, i.e., NP1-Ag_5Cu_0, has the identical size as NP2-$Ag_5Cu_{2.5}$, the NP1-Ag_5Cu_0 should have the same T_m and T_{sm} as the NP2-$Ag_5Cu_{2.5}$, which are 960 K and 900 K respectively. The increase

in T_{sm} is induced by size effect, i.e., increasing the radius leads to reduction in the ratio of surface atoms with low coordination number to the atoms with higher bulk coordination number, contributing to the decrease of the surface energy and thus the mobility of surface atoms. Not only at T_{sm}, but even at T_{room}, interfacial Cu and Ag atoms show higher mobility than inner Cu atoms and Ag atoms located between the interface and the shell, which can make a difference to the sintering dynamics as compared with multiple-Ag-NP sintering model. Detailed physical analysis will be demonstrated in the part of "Comparison between Multiple-CS-NP and Multiple-Ag-NP Models". Table 4.1 summarizes the geometrical details and the corresponding T_m and T_{sm} for each NP.

Table 4.1: Geometrical details, melting temperature (T_m) and surface premelting temperature (T_{sm}) for four NPs.

NP type	r_{cs}	r_c	#Cu atoms	#Ag atoms	T_m (K)	T_{sm} (K)
NP1-Ag_5Cu_0	$5a_{Ag}$	0	0	2120	960	900
NP2-$Ag_5Cu_{2.5}$	$5a_{Ag}$	$2.5a_{Ag}$	369	1874	960	900
NP3-Ag_8Cu_4	$8a_{Ag}$	$4a_{Ag}$	1505	7505	1180	1100
NP4-$Ag_{11}Cu_{5.5}$	$11a_{Ag}$	$5.5a_{Ag}$	4093	19401	1220	1160

4.3.2 Sintering Dynamics of Multiple CS NPs

As the size of NP decreases, the fraction of surface-layer atoms, which are more sensitive to the surrounding temperature [159, 160, 161], increases. Thus, a smaller NP is more thermodynamically active; this is also confirmed by their lower T_{sm} (Table 4.1). However, if the NP size is too small, quantum-confinement effect should be considered [162], which cannot be properly addressed in MD. Hence, for a clear observation of temperature-effect on sintering dynamics while avoiding the quantum-confinement effects, multiple-CS-NP model with NP2-$Ag_5Cu_{2.5}$ (the smallest NP in this research) is selected.

E_p is analyzed not only for detecting the sintering mechanism but also for evaluating the stability of the final sintered structure. As shown in Figure 3a, the E_p of Ag shell atoms (obtained by averaging the E_p during last 50 ps) in final structures sintered at different temperatures increases linearly as temperature rises from 300 K to 500 K, characterized as

the low-temperature sintering without elimination of pores [Figures 4.3(a)-(c)]. The surface diffusion mechanism loses its dominance at low temperatures (300 - 500 K); instead, other mechanisms, such as plastic deformation involving dislocation or twinning, contribute to the densification [136]. Therefore, we employ 300 K as a low-temperature case in order to study various sintering mechanisms for multiple-CS-NP model. An obvious decrease in E_p of Ag shell in structures sintered at a temperature range from 600 K (pore elimination temperature, T_{pe}) to 800 K is observed, which is induced by the annihilation of free surface due to pore elimination after sintering [Figures 4.3(d)-(f)]. The E_p decrease indicates that a more stable structure is achieved in this temperature range ($T_{\mathrm{pe}} < \mathrm{T} < T_{\mathrm{sm}}$) than at low-temperature cases. At 900 K (T_{sm}), the pores are eliminated with a higher atomic speed since surface-premelting occurs in multiple NP2-$Ag_5Cu_{2.5}$ [Figure 4.3(g)]. The whole NP system is melted at 1000 K (the T_{m} is 960 K fo NP2-$Ag_5Cu_{2.5}$) and the final sintered structure is shown as Figure S1h. The melting is also indicated by a steep jump in E_p from 900 K to 1000 K (Figure 4.4a). However, different from the Ag shell, the E_p of Cu core shows a linear increase both before and after melting, indicating that the Cu cores do not participate in the sintering at temperatures below T_{m}. Based on the above analysis, we thus only selected 300, 600, 900, and 1000 K to efficiently analyze the temperature effects on the sintering dynamics of multiple-CS-NP model with NP2-$Ag_5Cu_{2.5}$ in detail.

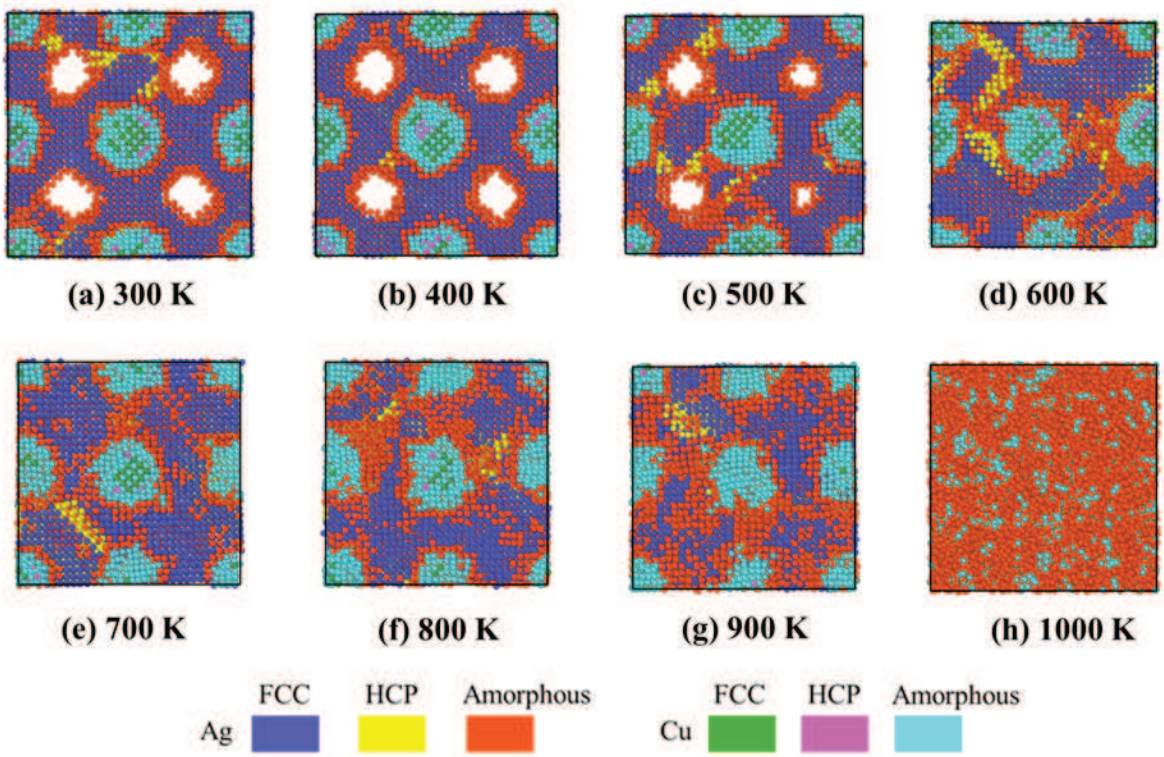

Figure 4.3: Final Morphology of sintered multiple-CS-NP model $Ag_5Cu_{2.5}$ at different temperatures (T's). The pores are not eliminated under T of 500 K. As T increases from 600 K to 900 K, the porosity gradually decreases, thus a more densified structure is obtained, but still some pores are left inside within the sintered structures. At 1000 K, the whole system melts, the core-shell structure is collapsed and a Cu-Ag alloy is obtained. Color scheme is explained as: Blue: Ag FCC; Yellow: Ag HCP; Red: Ag amorphous; Green: Cu FCC; Magenta: Cu HCP; Cyan: Cu amorphous.

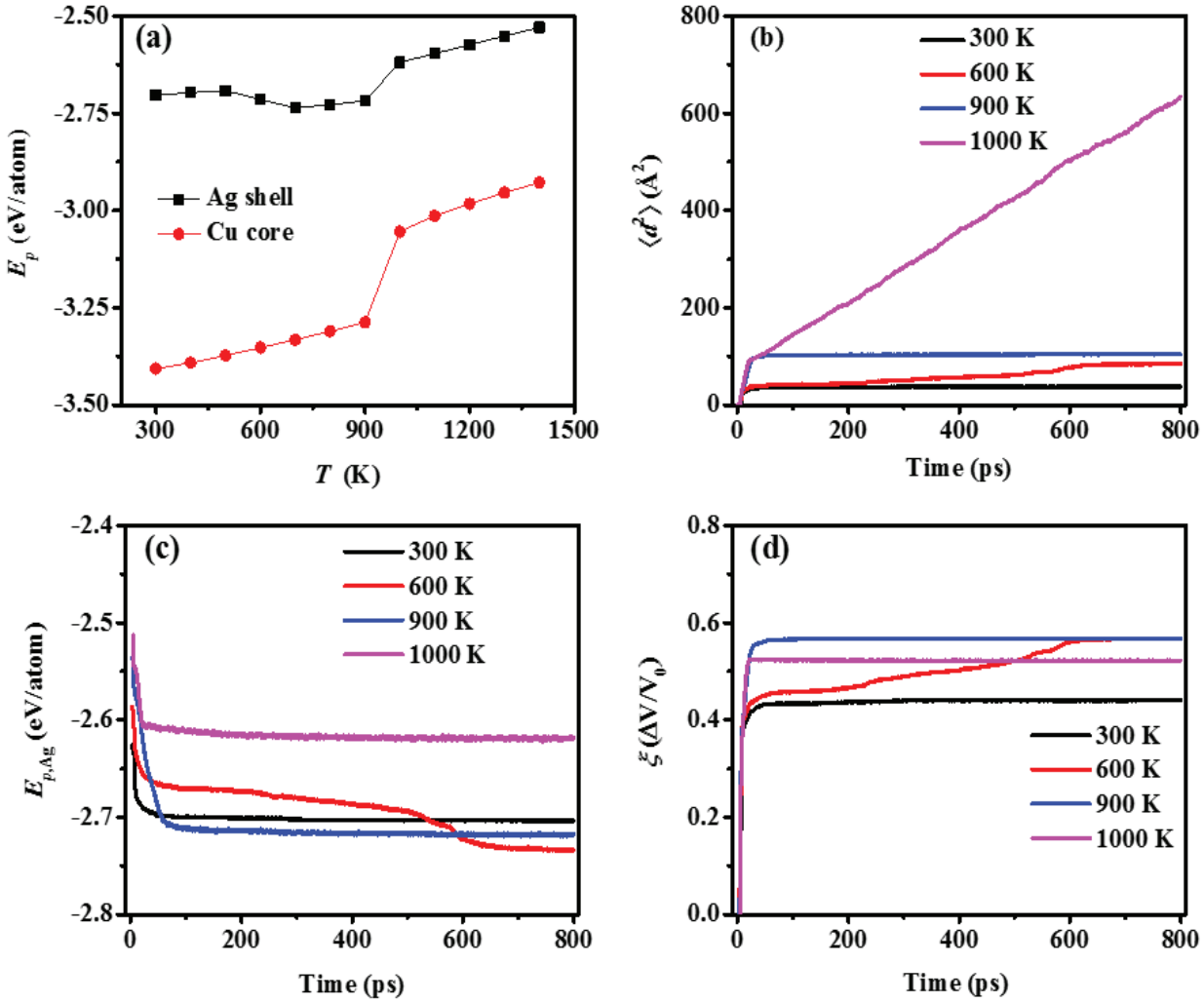

Figure 4.4: (a) Averaged potential energy (E_p) of the Ag shell and Cu core over the last 50 ps (total simulation time: 800 ps) with respect to temperature. (b) Mean square displacement ($\langle d^2 \rangle$) of the surface atoms (atoms located within the depth of a_{Ag}) in multiple NP2-$Ag_5Cu_{2.5}$. (c) Potential energy of the Ag shell in NP $Ag_5Cu_{2.5}$ ($E_{p,\mathrm{Ag}}$) at four representative temperatures (i.e., 300, 600, 900 and 1000 K). (d) Densification (ξ) of the sintered structure of multiple NP2-$Ag_5Cu_{2.5}$. The trends of the $\langle d^2 \rangle$, $E_{p,\mathrm{Ag}}$, and ξ coincide well with each other.

At each selected temperature, evolutions of 1) $\langle d^2 \rangle$ of surface atoms, 2) E_p of Ag shell ($E_{p,Ag}$), as well as 3) ξ of the sintering system are monitored and plotted in Figures 4.4b-d, to characterize the sintering dynamics. Regardless of temperature, the agglomeration of NPs involving neck formation and fast broadening are achieved within 20 ps as evidenced by the steep slope of curves in Figures 4.4b-d. This indicates that the initial migration of atoms

is not dominated by thermal energy of the system. Instead, the attractive forces existing between the atoms lead to initial contact only if the distance between the NPs is less than the cutoff radius of the interaction potential. The finding of temperature-independent initial stage in multiple-CS-NP sintering coincides well with our previous two-CS-NP sintering model, and also coincides with many other MD simulations of sintering [163, 164, 149, 138, 165].

The sintering process after the initial agglomeration shows a distinct temperature dependence. At 300 K the $\langle d^2 \rangle$ of the surface atoms remains constant due to insufficient kinetic energy (E_k) for diffusion, leading to the equilibrium of E_p and ξ, while at 600 K, E_p and ξ do not reach the equilibrium. Continuous densification of the multiple-CS-NP model occurs at 600 K with a moderate speed, which facilitates the observation of various sintering mechanisms. A detailed illustration of sintering process at 600 K is shown in Figure 4.5, during which local order of each atom is identified by common neighbor analysis [166, 167, 168] and categorized as: (1) FCC (atoms in a local FCC order), (2) HCP (atoms in a local HCP orders), and (3) amorphous (atoms in all other local orders, including BCC order).

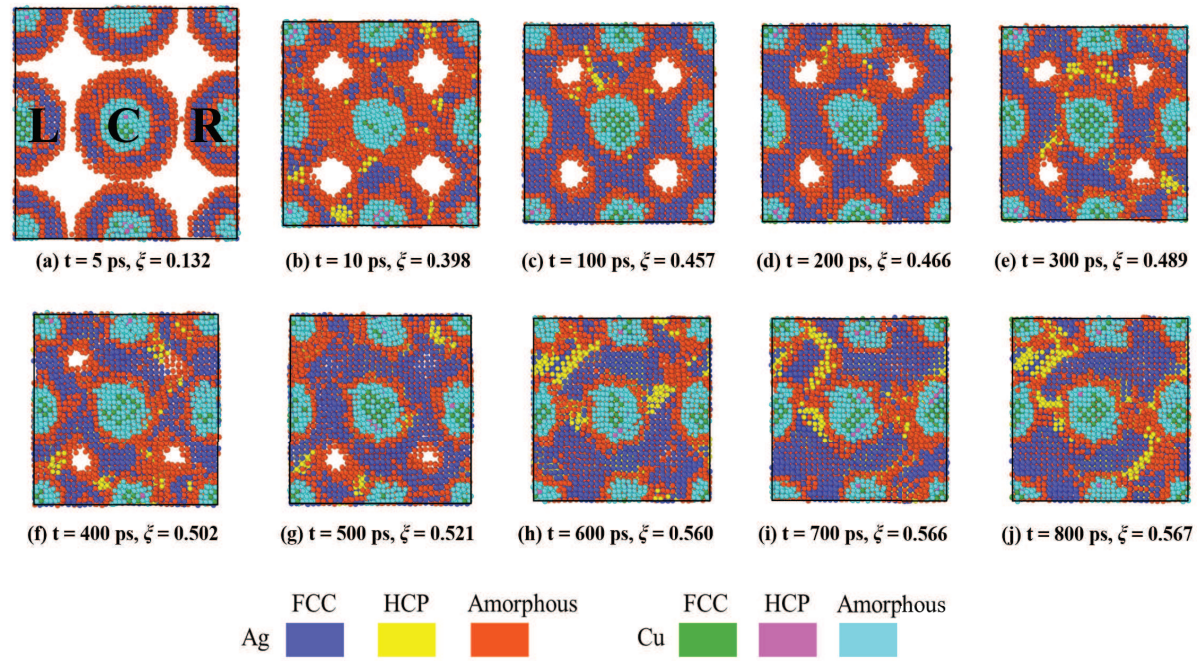

Figure 4.5: Cross-sectional images of the sintering process of porous multiple NP2-$Ag_5Cu_{2.5}$ at 600 K. Blue: Ag FCC; yellow: Ag HCP; red: Ag amorphous; green: Cu FCC; magenta: Cu HCP; cyan: Cu amorphous.

We start to monitor the sintering behavior at 600 K from 5 ps, at which the NPs make their initial contact (Figure 4.5a). The surface and partial inner Ag atoms of the center NP (NP 1, as indicated in Figure 4.5) deviate from original FCC lattice sites to form several high-energy surface layers. As NPs approach one another, surface energy is minimized, necks are created and rapidly broadened within 5 ps, and curvature of the pores are diminished (Figure 4.5b). Different from the two-CS-NP sintering model, the multiple-CS-NP sintering model loses elastic collision behavior (collision and then bouncing back), which can be attributed to the pore-induced curvature and packing arrangement. One mechanism is that although the neck formation and broadening stages reduce the curvature, the strong propensity of further reducing the curvature and thus the surface energy leads to further diffusion. Another possible mechanism for the disappearance of the elastic collision behavior is the symmetry of the multiple-CS-NP system. Assuming that NPs 2 and 3 (as indicated in Figure 4.5) elastically collide with NP 1 from both sides at the same time, NP 1 will either move right or left. Therefore, the elastic collision behavior cancels out and do not show up in this

SC packing arrangement. From 10 ps to 100 ps, amorphized atoms in the neck region rearrange themselves, leading to the recrystallization and thus contributing to further E_p reduction. This detected amorphization-recrystallization coincides with both two-CS-NP and two-pure-NP sintering model such as nickel [169] and copper [138]. After 100 ps, pores are gradually diminished with a moderate E_p reduction rate until 600 ps, at which several stacking faults (double HCP layers) are formed. This multiple-NP-sintered structure reaches quasi-equilibrium after 700 ps and stable stack faults are left within the structure, which could potentially be eliminated by annealing process. The reduction of E_p at 600 K in Figure 4.4c, acting as a driving force of the sintering [170, 133], contributes to densification comparable to that at 900 K, indicating that sintering at a lower T_{pe} can yield the same densification as T_{sm}. Note that the sintered structure at 600 K, even at 900 K, is not a fully densified structure, i.e., still some pores are left in the structure.

Based on the $\langle d^2 \rangle$ value (Figure 4.4b), solid surface diffusion is only observed at 600 K after the initial neck formation and growth stage. While at T_{room}, a dominant mechanism is not the solid surface diffusion, but the plastic deformation including stacking deformation and twin boundary formation during the neck formation and growth. At 900 K, pores in the multiple-CS-NP system are quickly eliminated due to higher mobility of premelted surface atoms. This irreversible pore elimination locates the system in a quasi-equilibrium low-energy state, thus the premelted atoms recrystallize and have not enough E_k to diffuse, similar to that at 300 K.

Surface and bulk diffusion of atoms dominate the liquid phase sintering at T_{m} (1000 K). The sintering process is dominated by the inter-diffusion of melted core and shell atoms, similar to that of two-CS-NP sintering model at T_m.[141] The sintering resultant is an alloy structure with well mixed Cu and Ag atoms. The ξ of the final structure at 1000 K (Figure 4.4d) is smaller (i.e., larger volume) than that at 900 K, and even smaller than that at 600 K due to the thermal expansion of the alloy.

In order to validate the reliability of our results and investigate the size effect, we performed sintering simulations with identical sintering conditions, but with different NP sizes, i.e., multiple-CS-NP sintering model with NP3-Ag_8Cu_4 and NP4-$Ag_{11}Cu_{5.5}$, $\langle d^2 \rangle$ and corresponding final sintered structures of these two multiple-CS-NP sintering models at

each temperature are shown as Figure 4.6. At T_{room}, it is commonly observed that the plastic deformation takes precedence in the sintering process, especially at initial stages. In multiple-CS-NP systems of NP3-Ag_8Cu_4, the solid surface diffusion dominates sintering at a temperature (900 K is tested for multiple-CS-NP NP3-Ag_8Cu_4) lower than its T_{sm} (Figure 4.6a), since pores are eliminated at T_{sm} and a stable structure is formed (Figure 4.6c), thereby deactivating the liquid surface diffusion at T_{sm}. However, for multiple-CS-NP with NP4-$Ag_{11}Cu_{5.5}$, pores are not eliminated even at T_{sm} (1160K, Figure 4.6d). As a result, solid surface diffusion dominates the sintering both at a lower temperature (1100 K is tested for multiple-CS-NP model with NP4-$Ag_{11}Cu_{5.5}$) and T_{sm} (Figure 4.6b).

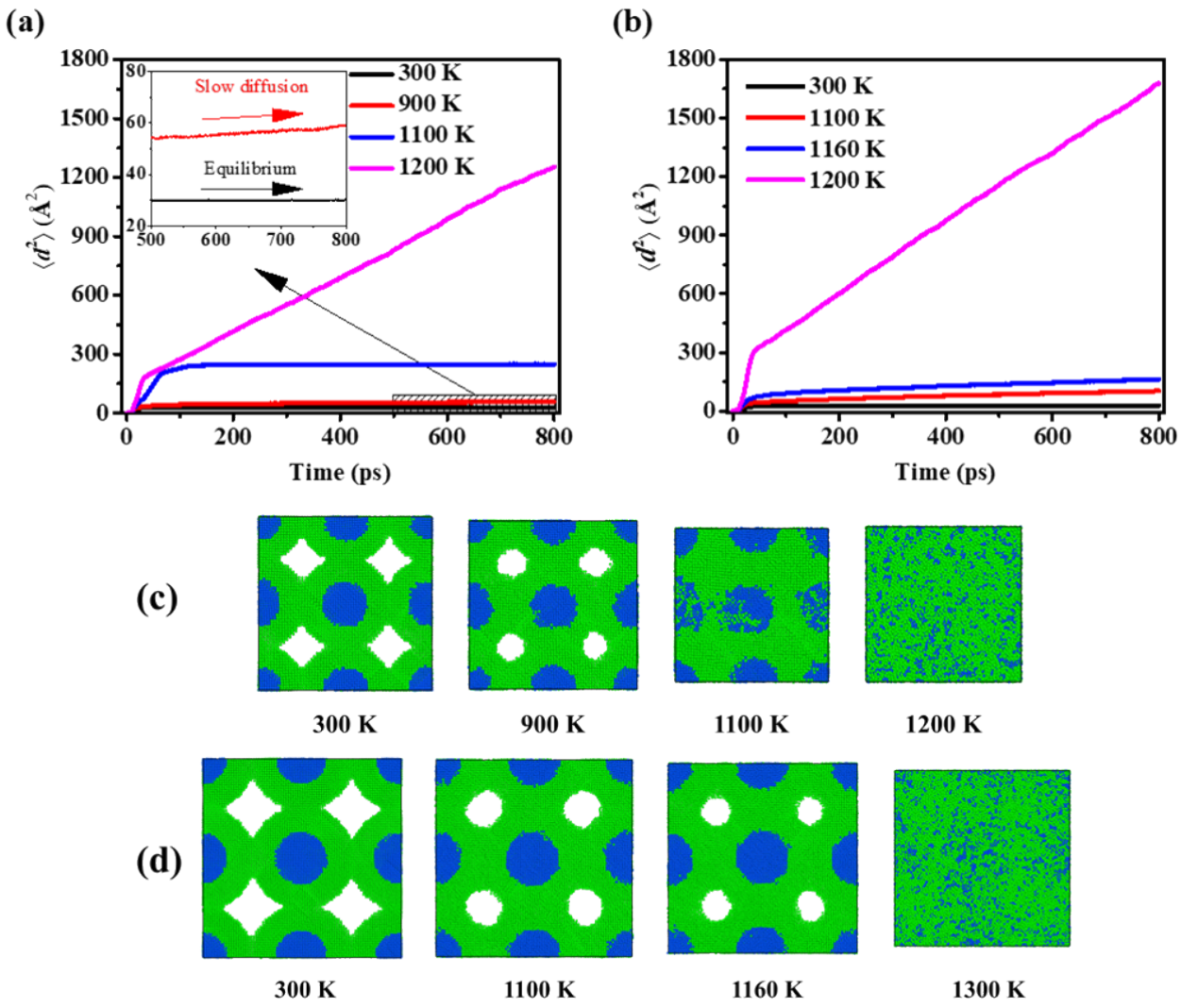

Figure 4.6: Mean square displacement ($\langle d^2 \rangle$)during the sintering of multiple-CS-NP structures with (a) Ag_8Cu_4 and (b) $Ag_{11}Cu_{5.5}$, respectively. Cross-sectional images of multiple-CS-NP structures with (c) Ag_8Cu_4 and (d) $Ag_{11}Cu_{5.5}$ at critical T's. Slow solid diffusion can be observed at 900 K in (a) while no solid diffusion can be observed after the liquid diffusion of surface premelted atoms at surface premelting temperature (T_{sm}) 1100 K. However, continuous diffusion is observed at both 1100 K and 1160 K in multiple-CS-NP $Ag_{11}Cu_{5.5}$ due to the continuous pore narrowing. Pores are eliminated at T_{sm} (1100 K) in multiple-CS-NP structures with Ag_8Cu_4; thus, no solid diffusion can be observed in (a). However, for $Ag_{11}Cu_{5.5}$, pores survive even at T_{sm} (1160 K), causing continuous solid diffusion following by initial liquid diffusion. The Ag shell atoms are colored with green, while the Cu core atoms are colored with blue.

4.3.3 Comparison between Multiple-CS-NP and Multiple-Ag-NP Models

Sintering simulations on multiple NP1-Ag_5Cu_0 under the same conditions (size, temperature and pressure, etc) as multiple NP2-$Ag_5Cu_{2.5}$ demonstrate that the CS NP is a more suitable candidate for higher ξ as shown in Figures 4.7a, b, and c. Since the CS and pure NPs have the same overall radius, the higher ξ of CS NP is not induced by the higher mobility of surface atoms. $\langle d^2 \rangle$ of the surface atoms in both the CS and pure NPs presents direct evidence for the similar mobility of surface atoms at T_{room} (black and green lines, Figure 4.7d). However, the mobility of the overall shell atoms in multiple-CS-NP model is over 60% higher than that of the multiple-Ag-NP (blue and red lines, Figures 4.7d, e, and f), where this increased shell mobility is attributed to lattice mismatch and interfacial restructuring between Ag and Cu atoms; thus, the mobility of the Ag atoms in the vicinity of the Cu-Ag interface is much higher than surface atoms. As temperature increases up to 600 K, pores are not eliminated in multiple-Ag-NP model due to a lack of sufficient solid surface diffusion (smaller $\langle d^2 \rangle$ of multiple-Ag-NP model than the multiple-CS-NP model is demonstrated in Figure 4.7e). Pore elimination at 600 K in multiple-CS-NP model suggests that the activated interfacial Ag atoms facilitate the ξ. At 900 K, even though surface premelting occurs in multiple-CS-NP model, the $\langle d^2 \rangle$ of the surface atoms is smaller than the multiple-Ag-NP model (black and green lines, Figure 4.7f). This supports that the surface diffusion is not a dominant mechanism at T_{sm} in small CS NP($r_{\text{cs}} < 8a_{\text{Ag}}$) while it contributes to the densification of multiple-Ag-NP model at 900 K.

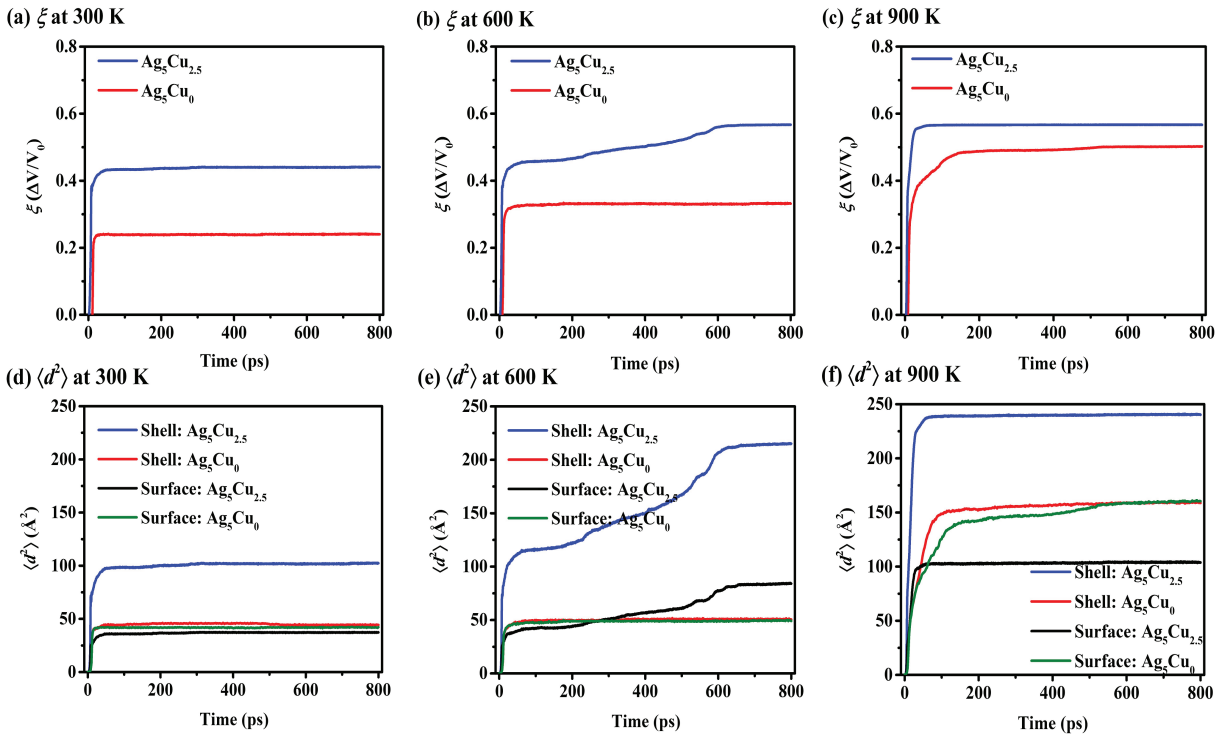

Figure 4.7: (a-c) Densification (ξ) and (d-f) mean square displacement ($\langle d^2 \rangle$) during multiple-NP sintering with $Ag_5Cu_{2.5}$ and Ag_5Cu_0 at 300 K, 600 K, and 900 K. At each temperature, the ξ of CS NP2-$Ag_5Cu_{2.5}$ is higher than that of pure Ag NP1-Ag_5Cu_0 due to the high mobility of interfacial Ag atoms in the CS NP model.

4.3.4 Self-Diffusivity and Activation Energy

Self-diffusivity (D_{self}) characterizes atom mobility during sintering, while activation energy (Q_v) is a good measure of sinterability within porous materials [135]. D_{self} and Q_v for surface and shell diffusion of multiple-CS-NP sintering model with NP2-$Ag_5Cu_{2.5}$ are studied in this research. Accurate diffusivity can be obtained only if the atoms travel a sufficient distance to make the $\langle d^2 \rangle$ have a linear, infinite time behavior, which is required by the Einstein relation. However, below T_m, the atoms vibrate around the equilibrium positions once the sintering system reaches the minimum-energy state; i.e., diffusion ends before it reaches linearity. Thus we employ the $\langle d^2 \rangle$, starting from the initial contact of multiple NPs and ending at the system minimum-energy state, as the diffusion period for calculating the D_{self} and Q_v (starting and ending points are indicted by spherical dots in Figures 4.8a and b). In Figure 4.9, the Q_v of the shell and surface diffusion is 0.42 eV and 0.46 eV respectively, which is in a

fairly good agreement with the reported Q_v for silver {100} surface diffusion (0.4 eV) [171]. However, these values are smaller than the Q_v of grain boundary (84.4 kJ/mol = 0.87 eV) [172] and lattice self-diffusion (192.1 kJ/mol = 1.99 eV) [173] in Ag. These discrepancies can be attributed to (1) a higher surface mobility induced by the ultrafine sizes, and (2) a higher mobility of interfacial Ag atoms in CS structures. Note that the Q_v of overall shell is lower than that of surface; i.e., the shell diffusion is easier to be activated compared with surface only. These results also coincide with our previous findings that the interfacial atoms of Ag shell have higher mobility than surface atoms and lead to a much higher densification in multiple-CS-NP model as compared with same-size multiple-Ag-NP model. Smaller D_{self} and higher Q_v are expected for larger NPs due to size effects, although significant size effects have not been reported on surface diffusivity for Ag NP in the size ranges of 10-40 nm [174]. More detailed examination on the size dependency of activation energy will be conducted with MD approach in the near future.

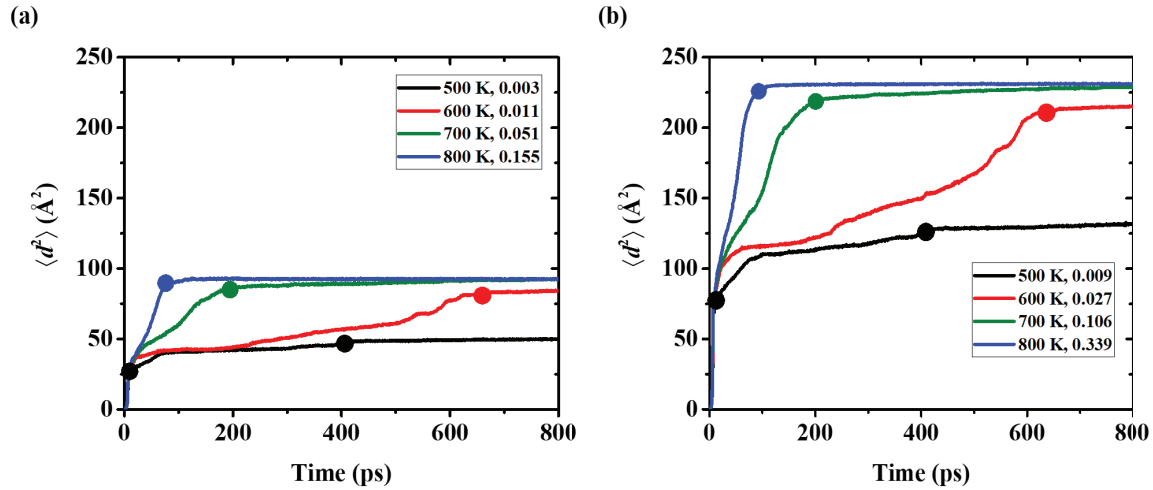

Figure 4.8: Mean square displacemnt ($\langle d^2 \rangle$) of the (a) surface and (b) shell atoms during the sintering of multiple $Ag_5Cu_{2.5}$ NPs. The self-diffusivity (in the unit of Å^2) obtained by linear fitting is also shown after each T. The dots in each curve represent the starting and ending points, during which the ($\langle d^2 \rangle$) is used to calculate the self-diffusivity and activation energy.

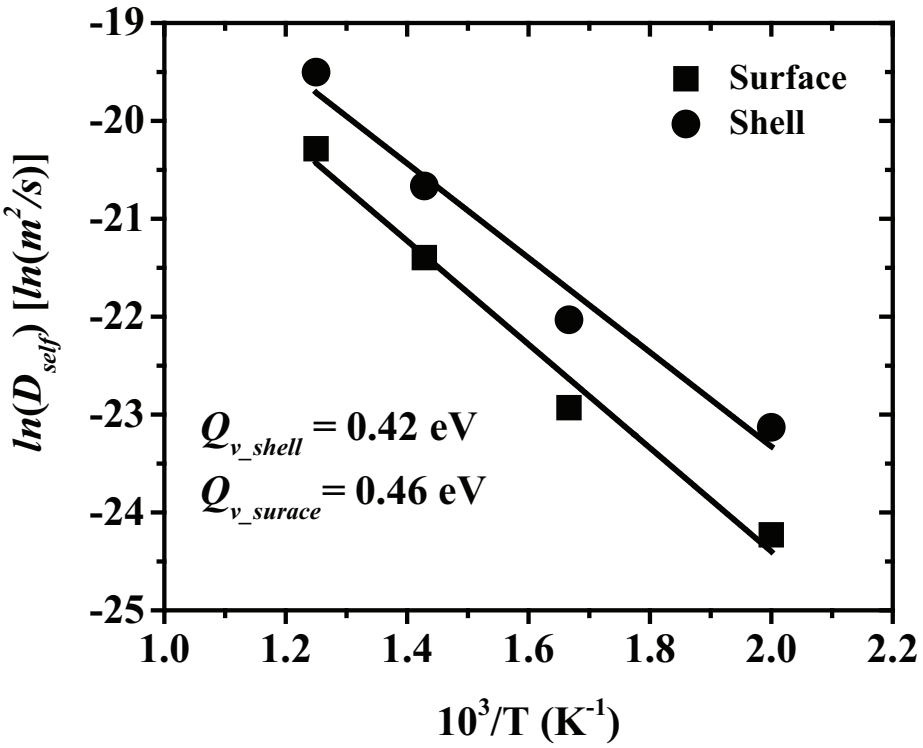

Figure 4.9: Arrhenius plot of self-diffusivity of shell and surface in the multiple-CS-NP sintering model Ag_5Cu_0. The solid line is the Arrhenius equation fitting. The activation energies obtained for the shell and surface are 0.42 eV and 0.46 eV, respectively.

4.3.5 Mechanical Properties

Temperature and size dependent mechanical properties including Young's modulus (E_{100}), yield strength (σ_{YS}), and Poisson's ratio (ν_{100}) are discussed in this section. Table 4.2 summarizes these properties of final structures sintered at four representative temperatures, which are i) $T_1 = T_{\mathrm{room}}$, ii) $T_{\mathrm{room}} < T_2 < T_{\mathrm{sm}}$, iii) $T_3 = T_{\mathrm{sm}}$, and iv) $T_4 > T_{\mathrm{m}}$ (i.e., 300, 600, 900, and 1000 K for sintered structures of both NP1-Ag_5Cu_0 and NP2-$Ag_5Cu_{2.5}$; 300, 900, 1100, and 1200 K for NP3-Ag_8Cu_4; 300, 1100, 1160 and 1300 K for NP4-$Ag_{11}Cu_{5.5}$). Since each NP is initially placed facing other NPs with [100] direction and do not rotate during sintering, the Young's modules, yield strength and Poisson's ratio obtained below T_{m} are regarded as those of {100} faces in the final structures. The Young's modulus (E_{100} = Δstress/Δstrain in elastic regime) and yield strength (σ_{YS}) are extracted from the strain-stress plots (not shown here), while the Poisson's ratio (ν_{100} = -$\varepsilon_{yy}/\varepsilon_{xx} = -\varepsilon_{zz}/\varepsilon_{xx}$) is obtained by calculating the strain ratio in the x, y, and x, z dimensions. During the tensile test, isotropic shrinkage

in the y and z direction is observed, demonstrating the identical Poisson's ratio in the final sintered structures.

Table 4.2: Mechanical properties of the final structures sintered at four critical temperatures.

T (K)	Young's modulus (E_{100}, GPa)				Yield strength (σ_{YS}, GPa)				Poisson's ratio (ν_{100})			
	NP1	NP2	NP3	NP4	NP1	NP2	NP3	NP4	NP1	NP2	NP3	NP4
300	17.04	21.33	14.11	11.24	1.18	1.83	1.30	1.04	0.12	0.30	0.26	0.24
600	21.72	33.64	–	–	1.63	2.55	–	–	0.23	0.37	–	–
900	33.15	38.51	22.12	–	2.62	2.84	2.04	–	0.38	0.39	0.29	–
1000	27.72	33.22	–	–	1.63	1.51	–	–	0.40	0.41	–	–
1100	–	–	40.34	21.43	–	–	3.73	1.71	–	–	0.39	0.28
1160	–	–	–	23.37	–	–	–	2.13	–	–	–	0.31
1200	–	–	28.13	–	–	–	1.87	–	–	–	0.41	–
1300	–	–	–	34.05	–	–	–	1.68	–	–	–	0.41

Through scrutinized comparison and analysis, we have the following findings:

(1) Below T_m, all three properties of the sintered structures by multiple NP1-Ag_5Cu_0 are smaller than the counterparts sintered by multiple NP2-$Ag_5Cu_{2.5}$, manifesting that the former has smaller elastic resistance and the maximum force it can bear for recovering the original shape is also smaller, but the resistance in the orthogonal directions of the strain are larger. Note that all of these properties also increase with temperature, regardless of the NP size. This suggests that the pore narrowing and elimination in the final sintered product increases its resistance of elastic deformation in the elongation direction, and the maximum force, with which the structure can withstand and still recover its original shape, while decreasing the resistance of deformation in the shrinkage directions.

(2) In general, all properties tend to decrease as the nanoscale grain size increases below T_{sm}. The E_{100} of nanocrystalline materials increases with decreasing the grain size, which contradicts the previous study [175]. However, the porosity of larger grain sized NP-sintered structure is also higher than smaller grain-sized structure (even the sintering temperature of larger grain sized structure is higher), and the porosity has substantially greater effect than

the grain size effect (larger porosity induces smaller E_{100}). Therefore, a more dominant porosity effect leads to a smaller E_{100} in larger grain sized structures. The grain-size dependency of σ_{YS} and ν_{100} coincides well with previous experimental and theoretical results [176, 177].

(3) For the sintered structure above T_{m}, E_{100} and σ_{YS} is smaller than that at T_{sm}, except the E_{100} of sintered NP4-$Ag_{11}Cu_{5.5}$. Pores in sintered structure of multiple NP4-$Ag_{11}Cu_{5.5}$ are not eliminated at T_{sm}, leading to a smaller E_{100}, compared with that at the temperature (1300 K) above T_{m}. Quenching has been executed before the tensile test with rate of 7×10^{12} K/s, 9×10^{12} K/s, and 10^{13} K/s for sintered multiple NP1-Ag_5Cu_0 and NP2-$Ag_5Cu_{2.5}$, NP3-Ag_8Cu_4, and NP4-$Ag_{11}Cu_{5.5}$, respectively, all of which are orders of magnitude higher than the critical quenching rate for glass formation (10^5 to 10^6 K/s) [178, 179]. The E_p evolutions during quenching also indicate that all three sintered structures form metallic glass, without an abrupt decrease in the E_p curve [180, 181].The formation of the metallic glass yields lower E_{100} and σ_{YS}, compared with those of nanostructured porous materials. Contrarily, ν_{100} increases with temperature regardless of whether the quenched structure is crystallized or metallic glass, which is different from the decrease of E_{100} and σ_{YS} at temperatures above T_{m}. A uniform ν_{100} of ~0.41 is obtained for all metallic glass structures, manifesting the identical resistance in shrinkage direction.

4.3.6 Thermodynamic Properties

Thermodynamic properties (i.e., β_{T}, α_{p}, and c_{v}) calculated from our simulations are summarized in Table 4.3. The β_{T} and α_{p} are calculated. The response of the volumetric change to pressure is more significant in a sintered structure with a larger porosity to yield a higher isothermal compressibility β_{T}. At T_{room}, all four sintered structures possess large porosities, which induce large β_{T} (0.099, 0.053, 0.068, and 0.095 GPa^{-1} for NP1, NP2, NP3, and NP4 sintered structures, respectively), while β_{T} decreases with increasing temperature due to pore narrowing and elimination. Differing from sintered NP3 and NP4, β_{T} of the molten sintered structures of NP1 and NP2 are 0.018 $\mathrm{GPa}^{-1}$and 0.015 GPa^{-1}, both of which are larger than those at T_{sm} of 900 K. The sintered structures by multiple NP3's and NP4's still contain pores at T_{sm} (Figure 4.6d), but not at T_{m}. Thus, the β_{T} at T_{sm}

is larger than the molten sintered structures of NP3 and NP4. On the other hand, pores in NP1 and NP2 are completely eliminated above T_{sm}, so we attribute the larger β_T above T_{sm} to its less crystallinity instead of porosity, which results in higher entropy and more compressibility. This analysis concludes that porosity dominates the decreasing trend of β_T in NP-sintered structure below T_{sm}, while the dominant factor switches to crystallinity once pores are completely eliminated. α_p exhibits porosity and grain-size independence, i.e., no obvious difference is observed for all NP-sintered structures below T_{sm}. A uniform α_p ($\sim 1.2\times10^{-4}$ K^{-1}) is achieved for all amorphous Cu-Ag alloy structure, which is $\sim$75% higher than the α_p of crystallized structure. Thus, the higher entropy of the less-crystallized melted structure induces not only more compressibility, but also more expansivity. Similar to α_p, no obvious dependency on porosity, grain size and crystallinity is observed for c_v. Values ranging from 0.111 to 0.170 kJ/kg-K are obtained for all CS NP-sintered structures, while a much smaller averaged c_v for pure Ag NP sintered structure is calculated as 0.054 kJ/kg-K.

Table 4.3: Thermodynamic properties of three final structures sintered at four different sintering temperatures.

T (K)	Isothermal compressibility (β_T, GPa^{-1})				Coefficient of thermal expansion ($\alpha_p \times 10^5$, K^{-1})				Specific heat capacity (c_v, kJ/kg-K)			
	NP1	NP2	NP3	NP4	NP1	NP2	NP3	NP4	NP1	NP2	NP3	NP4
300	0.099	0.053	0.068	0.095	5.50	6.43	6.69	6.48	0.051	0.134	0.122	0.122
600	0.068	0.014	–	–	6.07	6.50	–	–	0.055	0.122	–	–
900	0.017	0.010	0.041	–	7.40	7.26	5.90	–	0.056	0.111	0.150	–
1000	0.018	0.015	–	–	15.40	12.03	–	–	0.052	0.149	–	–
1100	–	–	0.009	0.049	–	–	7.41	6.85	–	–	0.128	0.167
1160	–	–	–	0.038	–	–	–	6.14	–	–	–	0.170
1200	–	–	0.008	–	–	–	12.02	–	–	–	0.132	–
1300	–	–	–	0.009	–	–	–	11.89	–	–	–	0.128

4.4 Conclusion

We report the sintering differences and similarities between (1) multiple-CS-NP models with different-sized NPs, (2) the multiple-CS-NP and two-CS-NP models, and (3) the multiple-CS-NP model and multiple-Ag-NP model. Interplay among porosity, grain size, and crystallinity on the mechanical and thermodynamic properties of NP-sintered structures are also unraveled. The main conclusions are drawn below as:

1. Differing from the two-CS-NP sintering model, this research on the sintering of multiple-CS-NP exhibits accurate description of agglomeration and pore elimination. Loss of elastic collision behavior during the sintering of multiple-CS-NP model is found which contributes to a faster reach on thermodynamic equilibrium.

2. For smaller CS NP ($r_{\mathrm{c}} < 8a_{\mathrm{Ag}}$), solid surface diffusion dominates sintering at an intermediate temperature ($T_{\mathrm{room}} < T < T_{\mathrm{sm}}$) for the multiple-CS-NP sintering model, while plastic deformation plays a significant role at the T_{room}; liquid surface diffusion is deactivated after recrystallization at T_{sm}. Solid surface diffusion can induce continuous pore narrowing and elimination at T_{sm} in larger NP ($r_{\mathrm{c}} > 11a_{\mathrm{Ag}}$).

3. Activated interfacial atoms induced by lattice mismatch and interfacial interaction contribute to a higher densification, and thus a higher bonding strength in multiple-CS-NP sintered structures than the pure Ag NP sintered structures.

4. E_{100}, σ_{YS}, and ν_{100} of the NP-sintered structure under T_{sm} are positively correlated with grain size, but negatively with porosity. In general, the metallic glass structure yields a lower E_{100} and σ_{YS}, but identical ν_{100}, compared with nanoporous crystallized structures. In terms of thermodynamics properties, the β_{T} also has negative dependency on porosity while the α_{p} and c_{v} are independent of porosity and grain size.

This research illustrates a more realistic sintering scheme of multiple-CS-NP model at various critical temperatures than the two-CS-NP sintering model. The size and temperature dependency of the properties of the final sintered structures are investigated to provide a solid theoretical basis for selecting suitable sized NP and temperature to meet specific property requirements. These findings corroborate our previous research on sintering dynamics of two Cu-Ag CS NPs. Further simulations for the effects of relative crystallographic orientation

and size distribution should be performed to gain an integrative insight into Cu-Ag CS NP sintering.

Chapter 5

Summary and Future Work

5.1 Summary and Impacts

Through the integrative investigation of sintering dynamics of Cu-Ag core-shell nanostructures with three different models (models of two core-shell NPs, two core-shell NWs, and multiple core-shell NPs) , sintering dynamics of loosely-packed nanostructure sintering in gas phase or on substrate has been elucidated, and the effect of porosity as well as nanostructure agglomeration during sintering have been illustrated: (1) two new sintering mechanisms are found, i.e., crystallization-amorphization-recrystallization during solid-phase sintering process and wetting in the sintering of two unequally sized NPs. (2) A three-stage sintering process is found for both nanoparticle and nanowires, involving the fast neck formation and growth (stage 1), slow neck growth (stage 2), and formation of stable joined structure with defects. (3) Optimal ratio of core radius to shell thickness is suggested to experimentalist to achieve maximum bonding strength. (4) Role of Cu is found to be increasing the mobility of overall shell atoms, thus increasing the sinterability of the nanostructures and the bonding strength. (5) Mechanical and thermal properties of the sintered nanostructure exhibit competitive performance compared with its bulk counterpart or single nanoparticle. The enhanced understanding in nanostructure sintering provides a theoretic basis for experimentalists to choose optimal sintering conditions to achieve desirable properties of a sintered structures, which opens new opportunities for developing new applications in printable nanoinks, catalysts, electrodes and other energy devices.

5.2 Recommendation for Future Studies

In all these studies, only the temperature and size effects are considered, while other parameters, such as the crystallographic orientation, pressure, size distribution, etc., are maintained constant, which is contradictory to the realistic sintering model. For further enhancing the understanding in sintering of a more realistic model, I would like to recommend continuing the work in:

(1) Studying the temperature and pressure effect on the sintering dynamics of a multiple-CS-NP/NW model containing randomly-distributed nanostructures. Here the "randomly-distributed" means the size, crystallographic orientation, core size, and packing arrangement are randomly distributed, and also the system contains both the NPs and NWs. This model should be comparable to the initial sintering nanostructure in experiment and would yield more scientific-reasoning results. *In situ* sintering experiment can be conducted at the same time for comparison.

(2) Performing tensile test simulations on the sintered product from research (1), to calculate the mechanical properties and elucidate the deformation mechanisms. Also, different thermal properties can be calculated for comparison. This research would be beneficial to the experimentalist in designing sintering conditions to achieve desirable structures for specific applications.

(3) Employing the quantum mechanics approach, such as the density functional theory to compare the sintering dynamics of the multiple-CS-NP/NW model obtained from molecular dynamics. The thermal and electrical transport properties of the sintered structures (such as thermal and electrical conductivity) should also be further studied using quantum methods, since they are important properties which influence the safety and reliability of the electronic applications. However, the limit of the quantum method calculation relies in the speed of the calculation, thus developing quantum computing should significantly contribute to the scientific discovery, which is also a promising research field.

Bibliography

[1] W David Kingery. Introduction to ceramics. 1960. ix, 2

[2] Gurcan Aral, Md Mahbubul Islam, and Adri CT Van Duin. Role of surface oxidation on the size dependent mechanical properties of nickel nanowires: a reaxff molecular dynamics study. *Physical Chemistry Chemical Physics*, 20(1):284–298, 2018. ix, 5

[3] Ali Yousefzadi Nobakht, Yasser Ashraf Gandomi, Jiaqi Wang, Matthew H Bowman, Drew C Marable, Benton E Garrison, Daekun Kim, and Seungha Shin. Thermal rectification via asymmetric structural defects in graphene. *Carbon*, 132:565–572, 2018. ix, 5

[4] Randall M German. Sintering theory and practice. *Solar-Terrestrial Physics (Solnechno-zemnaya fizika)*, page 568, 1996. 1

[5] Sukjoon Hong, Junyeob Yeo, Gunho Kim, Dongkyu Kim, Habeom Lee, Jinhyeong Kwon, Hyungman Lee, Phillip Lee, and Seung Hwan Ko. Nonvacuum, maskless fabrication of a flexible metal grid transparent conductor by low-temperature selective laser sintering of nanoparticle ink. *ACS nano*, 7(6):5024–5031, 2013. 1

[6] Kenjiro Fukuda, Tomohito Sekine, Yu Kobayashi, Daisuke Kumaki, Mitsunori Itoh, Minami Nagaoka, Takami Toda, Sayaka Saito, Masato Kurihara, Masatomi Sakamoto, et al. Stable organic thin-film transistors using full solution-processing and low-temperature sintering silver nanoparticle inks. *Organic Electronics*, 13(9):1660–1664, 2012. 1

[7] A Hu, JY Guo, H Alarifi, G Patane, Y Zhou, G Compagnini, and CX Xu. Low temperature sintering of Ag nanoparticles for flexible electronics packaging. *Applied Physics Letters*, 97(15):153117, 2010. 1

[8] Shlomo Magdassi, Michael Grouchko, Oleg Berezin, and Alexander Kamyshny. Triggering the sintering of silver nanoparticles at room temperature. *ACS Nano*, 4 (4):1943–1948, 2010. 1

[9] James M Haile. *Molecular dynamics simulation: elementary methods*. John Wiley & Sons, Inc., 1992. 4

[10] Daan Frenkel and Berend Smit. *Understanding molecular simulation: from algorithms to applications*, volume 1. Elsevier, 2001. 4

[11] Dennis C Rapaport. *The art of molecular dynamics simulation*. Cambridge University Press, 2004. 4

[12] R Leach Andrew. *Molecular modeling principles and applications*. 2nd, editor.: Pearson Education Limited, 2001. 4

[13] Herman JC Berendsen, JPM van Postma, Wilfred F van Gunsteren, ARHJ DiNola, and JR Haak. Molecular dynamics with coupling to an external bath. *The Journal of Chemical Physics*, 81(8):3684–3690, 1984. 4

[14] Shuichi Nosé. A unified formulation of the constant temperature molecular dynamics methods. *The Journal of Chemical Physics*, 81(1):511–519, 1984. 4

[15] Shūichi Nosé. A molecular dynamics method for simulations in the canonical ensemble. *Molecular Physics*, 52(2):255–268, 1984. 4

[16] Alarifi HA, Murat Atis, C Özdoğan, A Hu, M Yavuz, and Y Zhou. Molecular dynamics simulation of sintering and surface premelting of silver nanoparticles. *Materials Transactions*, 54(6):884–889, 2013. 6, 10, 11

[17] Beat Buesser and Sotiris E Pratsinis. Morphology and crystallinity of coalescing nanosilver by molecular dynamics. *The Journal of Physical Chemistry C*, 119(18): 10116–10122, 2015. 6

[18] Ehsan Marzbanrad, Anming Hu, Boxin Zhao, and Y Zhou. Room temperature nanojoining of triangular and hexagonal silver nanodisks. *The Journal of Physical Chemistry C*, 117(32):16665–16676, 2013. 6, 21

[19] Y Norman Zhou. *Microjoining and nanojoining*. Elsevier, 2008. 6

[20] Ngoc Ha Nguyen, Anming Hu, John Persic, and John Z Wen. Molecular dynamics simulation of energetic aluminum/palladium core–shell nanoparticles. *Chemical Physics Letters*, 503(1-3):112–117, 2011. 6

[21] Wei Xie, Yaya Zheng, Jiacai Kuang, Zhen Wang, Shihe Yi, and Yingjun Deng. Preparation of disperse silver particles by chemical reduction. *Russian Journal of Physical Chemistry A*, 90(4):848–855, 2016. 6

[22] Hoang Tri Hai, Hitoshi Takamura, and Junichi Koike. Oxidation behavior of Cu–Ag core–shell particles for solar cell applications. *Journal of Alloys and Compounds*, 564: 71–77, 2013. 6

[23] Yan Jianfeng, Zou Guisheng, Hu Anming, and Y Norman Zhou. Preparation of PVP coated Cu NPs and the application for low-temperature bonding. *Journal of Materials Chemistry*, 21(40):15981–15986, 2011. 6

[24] Cheng Yang, Ching Ping Wong, and Matthew MF Yuen. Printed electrically conductive composites: conductive filler designs and surface engineering. *Journal of Materials Chemistry C*, 1(26):4052–4069, 2013. 6

[25] Masaharu Tsuji, Sachie Hikino, Yoshiyuki Sano, and Misao Horigome. Preparation of Cu@Ag core–shell nanoparticles using a two-step polyol process under bubbling of N_2 gas. *Chemistry Letters*, 38(6):518–519, 2009. 7, 59

[26] Ian E Stewart, Shengrong Ye, Zuofeng Chen, Patrick F Flowers, and Benjamin J Wiley. Synthesis of Cu–Ag, Cu–Au, and Cu–Pt core–shell nanowires and their use in transparent conducting films. *Chemistry of Materials*, 27(22):7788–7794, 2015. 7

[27] Dung Chinh Trinh, Thi My Dung Dang, Kim Khanh Huynh, Eric Fribourg-Blanc, and Mau Chien Dang. Synthesis of Cu core Ag shell nanoparticles using chemical reduction method. *Advances in Natural Sciences: Nanoscience and Nanotechnology*, 6(2):025018, 2015. 7

[28] Masato Miyakawa, Norihito Hiyoshi, Masateru Nishioka, Hidekazu Koda, Koichi Sato, Akira Miyazawa, and Toshishige M Suzuki. Continuous syntheses of Pd@Pt and Cu@Ag core–shell nanoparticles using microwave-assisted core particle formation coupled with galvanic metal displacement. *Nanoscale*, 6(15):8720–8725, 2014. 7

[29] Bingqing Cheng and Alfonso HW Ngan. The crystal structures of sintered copper nanoparticles: A molecular dynamics study. *International Journal of Plasticity*, 47: 65–79, 2013. 7

[30] JS Raut, RB Bhagat, and KA Fichthorn. Sintering of aluminum nanoparticles: a molecular dynamics study. *Nanostructured Materials*, 10(5):837–851, 1998. 7

[31] Qingzhou Cui, Fan Gao, Subhadeep Mukherjee, and Zhiyong Gu. Joining and interconnect formation of nanowires and carbon nanotubes for nanoelectronics and nanosystems. *Small*, 5(11):1246–1257, 2009. 7

[32] Jolke Perelaer, Antonius WM De Laat, Chris E Hendriks, and Ulrich S Schubert. Inkjet-printed silver tracks: low temperature curing and thermal stability investigation. *Journal of Materials Chemistry*, 18(27):3209–3215, 2008. 7

[33] Bok Y Ahn, Eric B Duoss, Michael J Motala, Xiaoying Guo, Sang-Il Park, Yujie Xiong, Jongseung Yoon, Ralph G Nuzzo, John A Rogers, and Jennifer A Lewis. Omnidirectional printing of flexible, stretchable, and spanning silver microelectrodes. *Science*, 323(5921):1590–1593, 2009. 7

[34] A Hu, JY Guo, H Alarifi, G Patane, Y Zhou, G Compagnini, and CX Xu. Low temperature sintering of Ag nanoparticles for flexible electronics packaging. *Applied Physics Letters*, 97(15):153117, 2010. 7

[35] R-Z Li, Rui Peng, KD Kihm, S Bai, D Bridges, U Tumuluri, Z Wu, T Zhang, G Compagnini, Z Feng, et al. High-rate in-plane micro-supercapacitors scribed onto photo paper using in situ femtolaser-reduced graphene oxide/Au nanoparticle microelectrodes. *Energy & Environmental Science*, 9(4):1458–1467, 2016. 7

[36] JY Guo, CX Xu, AM Hu, KD Oakes, FY Sheng, ZL Shi, J Dai, and ZL Jin. Sintering dynamics and thermal stability of novel configurations of Ag clusters. *Journal of Physics and Chemistry of Solids*, 73(11):1350–1357, 2012. 7

[37] Beat Buesser, AJ Grohn, and Sotiris E Pratsinis. Sintering rate and mechanism of TiO_2 nanoparticles by molecular dynamics. *The Journal of Physical Chemistry C*, 115 (22):11030–11035, 2011. 7

[38] Bingqing Cheng and Alfonso HW Ngan. The sintering and densification behaviour of many copper nanoparticles: A molecular dynamics study. *Computational Materials Science*, 74:1–11, 2013. 7

[39] Lingqi Yang, Yong Gan, Yuwen Zhang, and JK Chen. Molecular dynamics simulation of neck growth in laser sintering of different-sized gold nanoparticles under different heating rates. *Applied Physics A*, 106(3):725–735, 2012. 7, 21

[40] Panagiotis Grammatikopoulos, Cathal Cassidy, Vidyadhar Singh, Maria Benelmekki, and Mukhles Sowwan. Coalescence behaviour of amorphous and crystalline tantalum nanoparticles: a molecular dynamics study. *Journal of Materials Science*, 49(11): 3890–3897, 2014. 7

[41] Lifeng Ding, Ruslan L Davidchack, and Jingzhe Pan. A molecular dynamics study of sintering between nanoparticles. *Computational Materials Science*, 45(2):247–256, 2009. 7

[42] Seungha Shin, Massoud Kaviany, Tapan Desai, and Richard Bonner. Roles of atomic restructuring in interfacial phonon transport. *Physical Review B*, 82(8):081302, 2010. 7

[43] Pengxiang Song and Dongsheng Wen. Molecular dynamics simulation of the sintering of metallic nanoparticles. *Journal of Nanoparticle Research*, 12(3):823–829, 2010. 7, 8, 9, 21

[44] Fayyaz Hussain, Sardar Sikandar Hayat, Muhammad Imran, SA Ahmad, and Farida Bouafia. Sintering and deposition of nanoparticles on surface of metals: A molecular dynamics approach. *Computational Materials Science*, 65:264–268, 2012. 7

[45] Murray S Daw and Michael I Baskes. Embedded-atom method: Derivation and application to impurities, surfaces, and other defects in metals. *Physical Review B*, 29 (12):6443, 1984. 7

[46] PL Williams, Y Mishin, and JC Hamilton. An embedded-atom potential for the Cu–Ag system. *Modelling and Simulation in Materials Science and Engineering*, 14(5): 817, 2006. 8

[47] Steve Plimpton. Fast parallel algorithms for short-range molecular dynamics. *Journal of Computational Physics*, 117(1):1–19, 1995. 8, 42, 62

[48] John Towns, Timothy Cockerill, Maytal Dahan, Ian Foster, Kelly Gaither, Andrew Grimshaw, Victor Hazlewood, Scott Lathrop, Dave Lifka, Gregory D Peterson, et al. XSEDE: accelerating scientific discovery. *Computing in Science & Engineering*, 16(5): 62–74, 2014. 8, 42, 62

[49] Yuki Tamura and Noriyoshi Arai. Molecular dynamics simulation of the melting processes of core–shell and pure nanoparticles. *Molecular Simulation*, 41(10-12):905–912, 2015. 9

[50] Xin-Lu Cheng, Jin-Ping Zhang, Hong Zhang, and Feng Zhao. Molecular dynamics simulations on the melting, crystallization, and energetic reaction behaviors of Al/Cu core-shell nanoparticles. *Journal of Applied Physics*, 114(8):084310, 2013. 9

[51] Mehdi Asgari and Hassan Behnejad. Molecular dynamics simulation of the melting process in $Ag_{27}Cu_{13}$ core–shell nanoalloy. *Chemical Physics*, 423:36–42, 2013. 9

[52] Pengxiang Song and Dongsheng Wen. Molecular dynamics simulation of a core–shell structured metallic nanoparticle. *The Journal of Physical Chemistry C*, 114(19):8688–8696, 2010. 9

[53] Yasushi Shibuta and Toshio Suzuki. Melting and nucleation of iron nanoparticles: A molecular dynamics study. *Chemical Physics Letters*, 445(4-6):265–270, 2007. 9

[54] Randall M German. Sintering theory and practice. *Solar-Terrestrial Physics (Solnechno-zemnaya fizika)*, page 568, 1996. 10

[55] GJ Ackland and AP Jones. Applications of local crystal structure measures in experiment and simulation. *Physical Review B*, 73(5):054104, 2006. 10

[56] Wolfgang Lechner and Christoph Dellago. Accurate determination of crystal structures based on averaged local bond order parameters. *The Journal of Chemical Physics*, 129 (11):114707, 2008. 10

[57] Alexander Stukowski. Structure identification methods for atomistic simulations of crystalline materials. *Modelling and Simulation in Materials Science and Engineering*, 20(4):045021, 2012. 10

[58] Rao Huang, Gui-Fang Shao, Xiang-Ming Zeng, and Yu-Hua Wen. Diverse melting modes and structural collapse of hollow bimetallic core–shell nanoparticles: A perspective from molecular dynamics simulations. *Scientific Reports*, 4:7051, 2014. 10, 12

[59] Rao Huang, Gui-Fang Shao, Yu-Hua Wen, and Shi-Gang Sun. Tunable thermodynamic stability of Au–CuPt core–shell trimetallic nanoparticles by controlling the alloy composition: insights from atomistic simulations. *Physical Chemistry Chemical Physics*, 16(41):22754–22761, 2014. 10

[60] Rao Huang, Yu-Hua Wen, Gui-Fang Shao, and Shi-Gang Sun. Insight into the melting behavior of Au–Pt core–shell nanoparticles from atomistic simulations. *The Journal of Physical Chemistry C*, 117(8):4278–4286, 2013. 10, 16

[61] Jakob Schiøtz, Francesco D Di Tolla, and Karsten W Jacobsen. Softening of nanocrystalline metals at very small grain sizes. *Nature*, 391(6667):561, 1998. 10

[62] Jakob Schiøtz and Karsten W Jacobsen. A maximum in the strength of nanocrystalline copper. *Science*, 301(5638):1357–1359, 2003. 10

[63] Shan Jiang, Yuwen Zhang, Yong Gan, Zhen Chen, and Hao Peng. Molecular dynamics study of neck growth in laser sintering of hollow silver nanoparticles with different heating rates. *Journal of Physics D: Applied Physics*, 46(33):335302, 2013. 10

[64] Siqi Li, Weihong Qi, Hongcheng Peng, and Jizheng Wu. A comparative study on melting of core–shell and janus Cu–Ag bimetallic nanoparticles. *Computational Materials Science*, 99:125–132, 2015. 12

[65] Rao Huang, Yu-Hua Wen, Zi-Zhong Zhu, and Shi-Gang Sun. Two-stage melting in core–shell nanoparticles: an atomic-scale perspective. *The Journal of Physical Chemistry C*, 116(21):11837–11841, 2012. 12

[66] Jakob Schiøtz, Tejs Vegge, FD Di Tolla, and Karsten Wedel Jacobsen. Atomic-scale simulations of the mechanical deformation of nanocrystalline metals. *Physical Review B*, 60(17):11971, 1999. 16

[67] P Zeng, S Zajac, PC Clapp, and JA Rifkin. Nanoparticle sintering simulations. *Materials Science and Engineering: A*, 252(2):301–306, 1998. 18, 21

[68] M Tavakol, M Mahnama, and R Naghdabadi. Mechanisms governing microstructural evolution during consolidation of nanoparticles. *Materials and Manufacturing Processes*, 30(11):1397–1402, 2015. 18

[69] Shlomo Magdassi, Michael Grouchko, Oleg Berezin, and Alexander Kamyshny. Triggering the sintering of silver nanoparticles at room temperature. *ACS Nano*, 4 (4):1943–1948, 2010. 21

[70] Michael Grouchko, Alexander Kamyshny, Cristina Florentina Mihailescu, Dan Florin Anghel, and Shlomo Magdassi. Conductive inks with a "built-in" mechanism that enables sintering at room temperature. *ACS Nano*, 5(4):3354–3359, 2011. 21

[71] Huilong Zhu. Sintering processes of two nanoparticles: a study by molecular dynamics simulations. *Philosophical Magazine Letters*, 73(1):27–33, 1996. 21

[72] Heng Pan, Seung H Ko, and Costas P Grigoropoulos. The solid-state neck growth mechanisms in low energy laser sintering of gold nanoparticles: a molecular dynamics simulation study. *Journal of Heat Transfer*, 130(9):092404, 2008. 21

[73] Michael Grouchko, Polina Roitman, Xi Zhu, Inna Popov, Alexander Kamyshny, Haibin Su, and Shlomo Magdassi. Merging of metal nanoparticles driven by selective wettability of silver nanostructures. *Nature Communications*, 5:2994, 2014. 30

[74] Sang-Chae Jeon, Byung-Kwon Yoon, Kwan-Hyeong Kim, and Suk-Joong L Kang. Effects of core/shell volumetric ratio on the dielectric-temperature behavior of $BaTiO_3$. *Journal of Advanced Ceramics*, 3(1):76–82, 2014. 34

[75] Chi-Hang Tsai, Shih-Yun Chen, Jenn-Ming Song, In-Gann Chen, and Hsin-Yi Lee. Thermal stability of Cu@Ag core–shell nanoparticles. *Corrosion Science*, 74:123–129, 2013. 34

[76] Alarifi HA, Murat Atis, C Özdoğan, A Hu, M Yavuz, and Y Zhou. Molecular dynamics simulation of sintering and surface premelting of silver nanoparticles. *Materials Transactions*, 54(6):884–889, 2013. 39, 45, 47

[77] Hani A Alarifi, M Atis, C Ozdogan, A Hu, M Yavuz, and Y Zhou. Determination of complete melting and surface premelting points of silver nanoparticles by molecular dynamics simulation. *The Journal of Physical Chemistry C*, 117(23):12289–12298, 2013. 39, 45

[78] Hong Wei, Zhuoxian Wang, Xiaorui Tian, Mikael Käll, and Hongxing Xu. Cascaded logic gates in nanophotonic plasmon networks. *Nature Communications*, 2:387, 2011. 39

[79] Yongli Yan, Chuang Zhang, Jian Yao Zheng, Jiannian Yao, and Yong Sheng Zhao. Optical modulation based on direct photon-plasmon coupling in organic/metal nanowire heterojunctions. *Advanced Materials*, 24(42):5681–5686, 2012. 39

[80] Barry P Rand, Peter Peumans, and Stephen R Forrest. Long-range absorption enhancement in organic tandem thin-film solar cells containing silver nanoclusters. *Journal of Applied Physics*, 96(12):7519–7526, 2004. 39

[81] Jose Ruben Morones, Jose Luis Elechiguerra, Alejandra Camacho, Katherine Holt, Juan B Kouri, Jose Tapia Ramírez, and Miguel Jose Yacaman. The bactericidal effect of silver nanoparticles. *Nanotechnology*, 16(10):2346, 2005. 39

[82] Chang Kyu Kim, Gyoung-Ja Lee, Min Ku Lee, and Chang Kyu Rhee. A novel method to prepare Cu@Ag core–shell nanoparticles for printed flexible electronics. *Powder Technology*, 263:1–6, 2014. 39

[83] A Hu, JY Guo, H Alarifi, G Patane, Y Zhou, G Compagnini, and CX Xu. Low temperature sintering of Ag nanoparticles for flexible electronics packaging. *Applied Physics Letters*, 97(15):153117, 2010. 39

[84] Dongjo Kim and Jooho Moon. Highly conductive ink jet printed films of nanosilver particles for printable electronics. *Electrochemical and Solid-State Letters*, 8(11):J30–J33, 2005. 39

[85] Jolke Perelaer, B-J de Gans, and Ulrich S Schubert. Ink-jet printing and microwave sintering of conductive silver tracks. *Advanced Materials*, 18(16):2101–2104, 2006. 39

[86] HT Hai, JG Ahn, DJ Kim, JR Lee, HS Chung, and CO Kim. Developing process for coating copper particles with silver by electroless plating method. *Surface and Coatings Technology*, 201(6):3788–3792, 2006. 39

[87] Florent Calvo. *Nanoalloys: from fundamentals to emergent applications*. Newnes, 2013. 40, 43

[88] Ping Lu, Michael Chandross, Timothy J Boyle, Blythe G Clark, and Paul Vianco. Equilibrium Cu-Ag nanoalloy structure formation revealed by in situ scanning transmission electron microscopy heating experiments. *APL Materials*, 2(2):022107, 2014. 40

[89] Marcelo M Mariscal, Sergio A Dassie, and Ezequiel PM Leiva. Collision as a way of forming bimetallic nanoclusters of various structures and chemical compositions. *The Journal of Chemical Physics*, 123(18):184505, 2005. 40

[90] S Alexis Paz and Ezequiel PM Leiva. Unveiling the mechanism of core–shell formation by counting the relative occurrence of microstates. *Chemical Physics Letters*, 595: 87–90, 2014. 40

[91] P Peng, A Hu, and Y Zhou. Laser sintering of silver nanoparticle thin films: microstructure and optical properties. *Applied Physics A*, 108(3):685–691, 2012. 40

[92] Joshua A Spechler and Craig B Arnold. Direct-write pulsed laser processed silver nanowire networks for transparent conducting electrodes. *Applied Physics A*, 108(1): 25–28, 2012. 40

[93] Qingzhou Cui, Fan Gao, Subhadeep Mukherjee, and Zhiyong Gu. Joining and interconnect formation of nanowires and carbon nanotubes for nanoelectronics and nanosystems. *Small*, 5(11):1246–1257, 2009. 40

[94] Fan Gao and Zhiyong Gu. Nano-soldering of magnetically aligned three-dimensional nanowire networks. *Nanotechnology*, 21(11):115604, 2010. 40

[95] Changxin Chen, Lijun Yan, Eric Siu-Wai Kong, and Yafei Zhang. Ultrasonic nanowelding of carbon nanotubes to metal electrodes. *Nanotechnology*, 17(9):2192, 2006. 40

[96] PL Williams, Y Mishin, and JC Hamilton. An embedded-atom potential for the Cu–Ag system. *Modelling and Simulation in Materials Science and Engineering*, 14(5): 817, 2006. 41

[97] Davide Bochicchio and Riccardo Ferrando. Morphological instability of core-shell metallic nanoparticles. *Physical Review B*, 87(16):165435, 2013. 43, 45, 55

[98] Riccardo Ferrando. Symmetry breaking and morphological instabilities in core-shell metallic nanoparticles. *Journal of Physics: Condensed Matter*, 27(1):013003, 2014. 43

[99] Emanuele Panizon, Davide Bochicchio, Giulia Rossi, and Riccardo Ferrando. Tuning the structure of nanoparticles by small concentrations of impurities. *Chemistry of Materials*, 26(11):3354–3356, 2014. 43

[100] Yue Qi, Tahir Çağın, Yoshitaka Kimura, and William A Goddard III. Molecular-dynamics simulations of glass formation and crystallization in binary liquid metals: Cu-Ag and Cu-Ni. *Physical Review B*, 59(5):3527, 1999. 45

[101] Simona Delsante, Gabriella Borzone, Rada Novakovic, Daniele Piazza, Giancarlo Pigozzi, Jolanta Janczak-Rusch, Martina Pilloni, and Guido Ennas. Synthesis and thermodynamics of Ag–Cu nanoparticles. *Physical Chemistry Chemical Physics*, 17 (42):28387–28393, 2015. 45

[102] Z Kuntová, G Rossi, and R Ferrando. Melting of core-shell Ag-Ni and Ag-Co nanoclusters studied via molecular dynamics simulations. *Physical Review B*, 77(20): 205431, 2008. 45

[103] Hassan Yousefi Oderji, Hassan Behnejad, Riccardo Ferrando, and Hongbin Ding. System-dependent melting behavior of icosahedral anti-Mackay nanoalloys. *RSC Advances*, 3(44):21981–21993, 2013. 45

[104] Yuki Tamura and Noriyoshi Arai. Molecular dynamics simulation of the melting processes of core–shell and pure nanoparticles. *Molecular Simulation*, 41(10-12):905–912, 2015. 45

[105] Zhen Yang, Xiaoning Yang, and Zhijun Xu. Molecular dynamics simulation of the melting behavior of Pt-Au nanoparticles with core–shell structure. *The Journal of Physical Chemistry C*, 112(13):4937–4947, 2008. 45

[106] Riccardo Ferrando. *Structure and properties of nanoalloys*, volume 10. Elsevier, 2016. 45

[107] Z Zak Fang and Hongtao Wang. Densification and grain growth during sintering of nanosized particles. *International Materials Reviews*, 53(6):326–352, 2008. 48

[108] Rao Huang, Yu-Hua Wen, Gui-Fang Shao, and Shi-Gang Sun. Insight into the melting behavior of Au–Pt core–shell nanoparticles from atomistic simulations. *The Journal of Physical Chemistry C*, 117(8):4278–4286, 2013. 52

[109] Jakob Schiøtz, Tejs Vegge, FD Di Tolla, and Karsten Wedel Jacobsen. Atomic-scale simulations of the mechanical deformation of nanocrystalline metals. *Physical Review B*, 60(17):11971, 1999. 52

[110] Rajaprakash Ramachandramoorthy, Wei Gao, Rodrigo Bernal, and Horacio Espinosa. High strain rate tensile testing of silver nanowires: rate-dependent brittle-to-ductile transition. *Nano Letters*, 16(1):255–263, 2015. 55

[111] B. Buesser, A. J. Grohn, and S. E. Pratsinis. Sintering rate and mechanism of TiO nanoparticles by molecular dynamics. *The Journal of Physical Chemistry C*, 115(22): 11030–11035, 2011. ISSN 1932-7447 (Print) 1932-7447 (Linking). 58

[112] Su Ding, Yanhong Tian, Zhi Jiang, and Xiaobin He. Molecular dynamics simulation of joining process of Ag-Au nanowires and mechanical properties of the hybrid nanojoint. *AIP Advances*, 5:057120, 2015. ISSN 2158-3226. 58

[113] Fan Gao, Subhadeep Mukherjee, Qingzhou Cui, and Zhiyong Gu. Synthesis characterization and thermal properties of nanoscale lead-free solders on multisegmented metal nanowires. *The Journal of Physical Chemistry C*, 113:9546–9552, 2009. 58

[114] L. Lin, L. Liu, P. Peng, G. Zou, W. W. Duley, and Y. N. Zhou. In situ nanojoining of Y- and T-shaped silver nanowires structures using femtosecond laser radiation. *Nanotechnology*, 27(12):125201. ISSN 1361-6528 (Electronic) 0957-4484 (Linking). 58

[115] P. Peng, A. Hu, A. P. Gerlich, G. Zou, L. Liu, and Y. N. Zhou. Joining of silver nanomaterials at low temperatures: processes, properties, and applications. *ACS Applied Materials & Interfaces*, 7(23):12597–12618, . ISSN 1944-8252 (Electronic) 1944-8244 (Linking). 58

[116] Reto Strobel and Sotiris E. Pratsinis. Flame aerosol synthesis of smart nanostructured materials. *Journal of Materials Chemistry*, 17(45):4743–4756. ISSN 0959-9428 1364-5501. 58

[117] K. N. Thakkar, S. S. Mhatre, and R. Y. Parikh. Biological synthesis of metallic nanoparticles. *Nanomedicine*, 6(2):257–262. ISSN 1549-9642 (Electronic) 1549-9634 (Linking). 58

[118] Dongjo Kim, Sunho Jeong, Bong Kyun Park, and Jooho Moon. Direct writing of silver conductive patterns: Improvement of film morphology and conductance by controlling solvent compositions. *Applied Physics Letters*, 89(26):264101, 2006. ISSN 00036951. 58

[119] Shlomo Magdassi, Michael Grouchko, Oleg Berezin, and Alexander Kamyshny. Triggering the sintering of silver nanoparticles at room temperature. *ACS Nano*, 4 (4):1943–1948, 2010. 58

[120] S. Sivaramakrishnan, P. J. Chia, Y. C. Yeo, L. L. Chua, and P. K. Ho. Controlled insulator-to-metal transformation in printable polymer composites with nanometal clusters. *Nature Materials*, 6(2):149–155. ISSN 1476-1122 (Print) 1476-1122 (Linking). 58

[121] T. H J VanOsch, J. Perelaer, A. W M DeLaat, and U. S Schubert. Inkjet printing of narrow conductive tracks on untreated polymeric substrates. *Advanced Materials*, 20 (2):343–345. ISSN 09359648 15214095. 58

[122] Wei Xie, Yaya Zheng, Jiacai Kuang, Zhen Wang, Shihe Yi, and Yingjun Deng. Preparation of disperse silver particles by chemical reduction. *Russian Journal of Physical Chemistry A*, 90(4):848–855. ISSN 0036-0244 1531-863X. 58

[123] Hoang Tri Hai, Hitoshi Takamura, and Junichi Koike. Oxidation behavior of CuAg coreshell particles for solar cell applications. *Journal of Alloys and Compounds*, 564: 71–77, 2013. ISSN 09258388. 58

[124] M. Miyakawa, N. Hiyoshi, M. Nishioka, H. Koda, K. Sato, A. Miyazawa, and T. M. Suzuki. Continuous syntheses of Pd@Pt and Cu@Ag core-shell nanoparticles using microwave-assisted core particle formation coupled with galvanic metal displacement. *Nanoscale*, 6(15):8720–8725. ISSN 2040-3372 (Electronic) 2040-3364 (Linking). 59

[125] Jit; Sarkar, Mainak; Bhattacharyya, Randhir; Kumar, N. Mandal;, and Manab Mallik. Synthesis and characterizations of CuAg coreshell nanoparticles. *Advanced Science Letters*, 22:193–196, 2016. 59

[126] P. Peng, A. Hu, and Y. Zhou. Laser sintering of silver nanoparticle thin films: microstructure and optical properties. *Applied Physics A: Materials Science & Processing*, 108(3):685–691, . ISSN 0947-8396 1432-0630. 59

[127] Andreas Albrecht, Almudena Rivadeneyra, Alaa Abdellah, Paolo Lugli, and Jos F. Salmern. Inkjet printing and photonic sintering of silver and copper oxide nanoparticles for ultra-low-cost conductive patterns. *Journal of Materials Chemistry C*, 4:3546–3554. ISSN 2050-7526 2050-7534. 59

[128] A. Hu, P. Peng, H. Alarifi, X. Y. Zhang, J. Y. Guo, Y. Zhou, and W. W. Duley. Femtosecond laser welded nanostructures and plasmonic devices. *Journal of Laser Applications*, 24(4):042001, . ISSN 1042346X. 59

[129] Panagiotis Grammatikopoulos, Cathal Cassidy, Vidyadhar Singh, Maria Benelmekki, and Mukhles Sowwan. Coalescence behaviour of amorphous and crystalline tantalum nanoparticles: a molecular dynamics study. *Journal of Materials Science*, 49(11): 3890–3897, 2013. ISSN 0022-2461 1573-4803. 59

[130] Brian J. Henz, Takumi Hawa, and Michael Zachariah. Molecular dynamics simulation of the kinetic sintering of Ni and Al nanoparticles. *Molecular Simulation*, 35(10-11): 804–811, 2009. ISSN 0892-7022 1029-0435. 59

[131] A. Hu, J. Y. Guo, H. Alarifi, G. Patane, Y. Zhou, G. Compagnini, and C. X. Xu. Low temperature sintering of Ag nanoparticles for flexible electronics packaging. *Applied Physics Letters*, 97(15):153117, . ISSN 00036951. 59

[132] Shan Jiang, Yuwen Zhang, Yong Gan, Zhen Chen, and Hao Peng. Molecular dynamics study of neck growth in laser sintering of hollow silver nanoparticles with different heating rates. *Journal of Physics D: Applied Physics*, 46(33):335302. ISSN 0022-3727 1361-6463. 59

[133] E. Marzbanrad, A. Hu, B. Zhao, and Y. Zhou. Room temperature nanojoining of triangular and hexagonal silver nanodisks. *The Journal of Physical Chemistry C*, 117 (32):16665–16676. ISSN 1932-7447 1932-7455. 59, 73

[134] Jingxiang Xu, Ryota Sakanoi, Yuji Higuchi, Nobuki Ozawa, Kazuhisa Sato, Toshiyuki Hashida, and Momoji Kubo. Molecular dynamics simulation of Ni nanoparticles sintering process in Ni/YSZ multi-nanoparticle system. *The Journal of Physical Chemistry C*, 117(19):9663–9672, . ISSN 1932-7447 1932-7455. 59, 60

[135] Kazuhide Nakao, Takayoshi Ishimoto, and Michihisa Koyama. Sintering simulation for porous material by integrating molecular dynamics and master sintering curve. *The Journal of Physical Chemistry C*, 118:15766–15772, 2014. 59, 77

[136] Bingqing Cheng and Alfonso H. W. Ngan. The sintering and densification behaviour of many copper nanoparticles: A molecular dynamics study. *Computional Materials Science*, 74:1–11, 2013. ISSN 09270256. 59, 60, 68

[137] J.S. Raut, R.B. Bhagat, and K.A. Fichthorn. sintering of aluminum nanoparticles: a molecular dynamics study. *Nanostructured Materials*, 10:837–851, 1998. 59

[138] P. Zeng, S. Zajac, P.C. Clapp, and J. A. Rifkin. Nanoparticle sintering simulations. *Materials Science and Engineering: A*, 252:301–306, 1998. 59, 63, 71, 73

[139] Jingxiang Xu, Shandan Bai, Yuji Higuchi, Nobuki Ozawa, Kazuhisa Sato, Toshiyuki Hashida, and Momoji Kubo. Multi-nanoparticle model simulations of the porosity effect on sintering processes in Ni/YSZ and Ni/ScSZ by the molecular dynamics method. *Journal of Materials Chemistry A*, 3(43):21518–21527, . ISSN 2050-7488 2050-7496. 59, 60

[140] Randell M. German. *Sintering theory and practice*. Wiley-Interscience, New York, 1996. 60

[141] Jiaqi Wang, Seungha Shin, and Anming Hu. Geometrical effects on sintering dynamics of Cu–Ag core–shell nanoparticles. *The Journal of Physical Chemistry C*, 120(31): 17791–17800, 2016. 60, 65, 73

[142] Murray S. Daw and M. I. Baskes. Embedded-atom method: Derivation and application to impurities, surfaces, and other defects in metals. *Physics Review B*, 29(12):6443–6453, 1984. ISSN 0163-1829. 62

[143] P. L. Williams, Y. Mishin, and J. C. Hamilton. An embedded-atom potential for the CuAg system. *Modelling and Simulation in Materials Science and Engineering*, 14(5): 817–833. ISSN 0965-0393 1361-651X. 62

[144] Loup Verlet. Computer "experiments" on classical fluids. I. Thermodynamical properties of Lennard-Jones molecules. *PHYSICAL REVIEW JOURNALS ARCHIVE*, 159(1):98–103. ISSN 0031-899X. 62

[145] Rao Huang, YuHua Wen, ZiZhong Zhu, and ShiGang Sun. Two-stage melting in coreshell nanoparticles: An atomic-scale perspective. *The Journal of Physical Chemistry C*, 116(21):11837–11841. ISSN 1932-7447 1932-7455. 62

[146] Pengxiang Song and Dongsheng Wen. Molecular dynamics simulation of a core shell structured metallic nanoparticle. *The Journal of Physical Chemistry C*, 114:8688–8696, 2010. 62

[147] Jianfeng Tang and Jianyu Yang. Simultaneous melting of shell and core atoms, a molecular dynamics study of lithiumcopper nanoalloys. *Journal of Nanoparticle Research*, 17(7):299. ISSN 1388-0764 1572-896X. 62

[148] Z. Yang, X. Yang, Z. Xu, and S. Liu. Structural evolution of Pt-Au nanoalloys during heating process: comparison of random and core-shell orderings. *Physical Chemistry Chemical Physics*, 11(29):6249–6255. ISSN 1463-9076 (Print) 1463-9076 (Linking). 62

[149] Pengxiang Song and Dongsheng Wen. Molecular dynamics simulation of the sintering of metallic nanoparticles. *Journal of Nanoparticle Research*, 12(3):823–829. ISSN 1388-0764 1572-896X. 63, 71

[150] Eric W Weisstein. Method of steepest descent. 2002. 63

[151] D. Keffer and P. Adhangale. The composition dependence of self and transport diffusivities from molecular dynamics simulations. *Chemical Engineering Journal*, 100 (1-3):51–69, 2004. ISSN 13858947. 63

[152] Ruichang Xiong, Khorgolkhuu Odbadrakh, Andrea Michalkova, Johnathan P. Luna, Tetyana Petrova, David J. Keffer, Donald M. Nicholson, Miguel A. Fuentes-Cabrera, James P. Lewis, and Jerzy Leszczynski. Evaluation of functionalized isoreticular metal organic frameworks (IRMOFs) as smart nanoporous preconcentrators of RDX. *Sensors and Actuators B: Chemical*, 148(2):459–468. ISSN 09254005. 63

[153] Voichita M. Dadarlat and Carol Beth Post. Insights into protein compressibility from molecular dynamics simulations. *The Journal of Physical Chemistry B*, 105:715–724, 2001. 64

[154] Mohammad Hadi Ghatee and Khadijeh Shekoohi. Structures, thermal stability, and melting behaviors of bimetallic CsNa clusters studied via molecular dynamics simulation. *Fluid Phase Equilibria*, 355:114–122, 2013. ISSN 03783812. 64

[155] A. Mashreghi. Determining the volume thermal expansion coefficient of TiO_2 nanoparticle by molecular dynamics simulation. *Computional Materials Science*, 62: 60–64. ISSN 09270256. 64

[156] Massoud Kaviany. *Heat Transfer Physics*. Cambridge University Press, New York, 2014. 65

[157] R. Z. Li, A. Hu, D. Bridges, T. Zhang, K. D. Oakes, R. Peng, U. Tumuluri, Z. Wu, and Z. Feng. Robust Ag nanoplate ink for flexible electronics packaging. *Nanoscale*, 7 (16):7368–7377, . ISSN 2040-3372 (Electronic) 2040-3364 (Linking). 65

[158] Siqi Li, Weihong Qi, Hongcheng Peng, and Jizheng Wu. A comparative study on melting of coreshell and janus Cu–Ag bimetallic nanoparticles. *Computational Materials Science*, 99:125–132, . ISSN 09270256. 66

[159] Saman Alavi and Donald L. Thompson. Molecular dynamics simualtions of the melting of aluminum nanoparticles. *The Journal of Physical Chemistry A*, 110:1518–1523, 2006. 67

[160] Gerrit Guenther and Olivier Guillon. Models of size-dependent nanoparticle melting tested on gold. *Journal of Materials Science*, 49(23):7915–7932, 2014. ISSN 0022-2461 1573-4803. 67

[161] Yasushi Shibuta and Toshio Suzuki. Melting and nucleation of iron nanoparticles: A molecular dynamics study. *Chemical Physics Letters*, 445(4-6):265–270. ISSN 00092614. 67

[162] J. G. Hou, B. Wang, J. Yang, K. Wang, W. Lu, Z. Li, H. Wang, D. M. Chen, and Q. Zhu. Disorder and suppression of quantum confinement effects in Pd nanoparticles. *Physical Review Letters*, 90(24):246803, 2003. ISSN 0031-9007 (Print) 0031-9007 (Linking). 67

[163] S. Arcidiacono, N. R. Bieri, D. Poulikakos, and C. P. Grigoropoulos. On the coalescence of gold nanoparticles. *International Journal of Multiphase Flow*, 30(7-8):979–994, 2004. ISSN 03019322. 71

[164] Amlan Dutta. Kinetics of neck formation during nanoparticle sintering: approach of dimensionality reduction. *REVIEWS ON ADVANCED MATERIALS SCIENCE*, 39: 25–33, 2014. 71

[165] Huilong Zhu. Sintering processes of two nanoparticles: A study by molecular dynamics simulations. *Philosophical Magazine Letters*, 73(1):27–33. ISSN 0950-0839 1362-3036. 71

[166] G. J. Ackland and A. P. Jones. Applications of local crystal structure measures in experiment and simulation. *Physics Review B*, 73(5):054104. ISSN 1098-0121 1550-235X. 71

[167] W. Lechner and C. Dellago. Accurate determination of crystal structures based on averaged local bond order parameters. *The Journal of Chemical Physics*, 129(11): 114707. ISSN 1089-7690 (Electronic) 0021-9606 (Linking). 71

[168] A. Stukowski. Structure identification methods for atomistic simulations of crystalline materials. *Modelling and Simulation in Materials Science and Engineering*, 20:045021, 2012. 71

[169] M. Tavakol, M. Mahnama, and R. Naghdabadi. Mechanisms governing microstructural evolution during consolidation of nanoparticles. *Materials and Manufacturing Processes*, 30(11):1397–1402. ISSN 1042-6914 1532-2475. 73

[170] Z. Z. Fang and H. Wang. Densification and grain growth during sintering of nanosized particles. *International Materials Review*, 53(6):326–352, 2013. ISSN 0950-6608 1743-2804. 73

[171] Grazyna Antczak and Gert Ehrlich. *Surface diffusion: metals, metal Atoms, and clusters*. Cambridge University Press, New York, 2010. 78

[172] E.A. Oliber, C. Cugno, M. Moreno, M. Esquivel, N. Haberkorn, J.E. Fiscina, and C.J.R. Gonzlez Olivera. Sintering of porous silver compacts at controlled heating rates in oxygen or argon. *Matéria*, 8:350–357, 2003. 78

[173] R. E. Hoffman and D. Turnbull. Lattice and grain boundary self-diffusion in silver. *Journal of Applied Physics*, 22(5):634–639, 1951. ISSN 00218979. 78

[174] M. A. Asoro, P. J. Ferreira, and D. Kovar. In situ transmission electron microscopy and scanning transmission electron microscopy studies of sintering of Ag and Pt nanoparticles. *Acta Materialia*, 81:173–183, 2014. ISSN 13596454. 78

[175] Hyoung Seop Kim and Mark B. Bush. The effcts of grain size and porosity on the elastic modulus of nanocrystalline materials. *Nanostructured Materials*, 11:361–367, 1999. 80

[176] Tae-Yeon Kim, John E. Dolbow, and Eliot Fried. Numerical study of the grain-size dependent Youngs modulus and Poissons ratio of bulk nanocrystalline materials. *International Journal of Solids and Structures*, 49(26):3942–3952. ISSN 00207683. 81

[177] Ning Wang, Zhuirui Wang, K. T. Aust, and U. Erb. Effect of grain size on mechanical properties of nanocrystalline materials. *Acta Metallurgica et Materialia*, 43:519–528, 1995. 81

[178] Qiang Li. Critical cooling rate for the glass formation of ferromagnetic $Fe_{40}Ni_{40}P_{14}B_6$ alloy. *Materials Letters*, 61(16):3323–3328. ISSN 0167577X. 81

[179] Dmitri V. Louzguine-Luzgin, Takanobu Saito, Junji Saida, and Akihisa Inoue. Influence of cooling rate on the structure and properties of a CuZrTiAg glassy alloy. *Journal of Materials Research*, 23(02):515–522. ISSN 0884-2914 2044-5326. 81

[180] XinLu Cheng, JinPing Zhang, Hong Zhang, and Feng Zhao. Molecular dynamics simulations on the melting, crystallization, and energetic reaction behaviors of Al/Cu core-shell nanoparticles. *Journal of Applied Physics*, 114(8):084310, 2013. ISSN 00218979. 81

[181] Jiangting Wang, Peter Damian Hodgson, Jingde Zhang, Wenyi Yan, and Chunhui Yang. Effects of quenching rate on amorphous structures of $Cu_{46}Zr_{54}$ metallic glass. *Journal of Materials Processing Technology*, 209(9):4601–4606. ISSN 09240136. 81

Vita

Jiaqi Wang (jqwang@vols.utk.edu) was born on May/20/1992 in Nantong (city) Jiangsu (province), which is a city close to the Yellow sea. He graduated with bachelor of science in Jun/2015 from Jiangsu University, China. He arrived at the United States at Jul/27/2015 and initiated his Ph.D. program immediately at Aug/01/2015. This is a thesis for his concurrent master of science towards the way to Ph.D., which he should be able to acquire within two years from May/2018. During his Ph.D. career, he has worked on four projects with molecular dynamics simulations: (1) Sintering dynamics of Cu-Ag core-shell nanostructures; (2) Brazing kinetics of Ni nanoparticles with Inconel 718 alloy; (3) Diffusion kinetics of θ'-Al_2Cu precipitate in Al matrix; (4) Machine learning approach to develop the interatomic potential of Cr-Al-O ternary system. He has published three first-author papers on the first project, and their modified versions are presented in this thesis and will not be counted for Ph.D. graduation. His dream is to become a renowned professor and work on the field he is/will be interested in for the whole life, because research is his favorite!